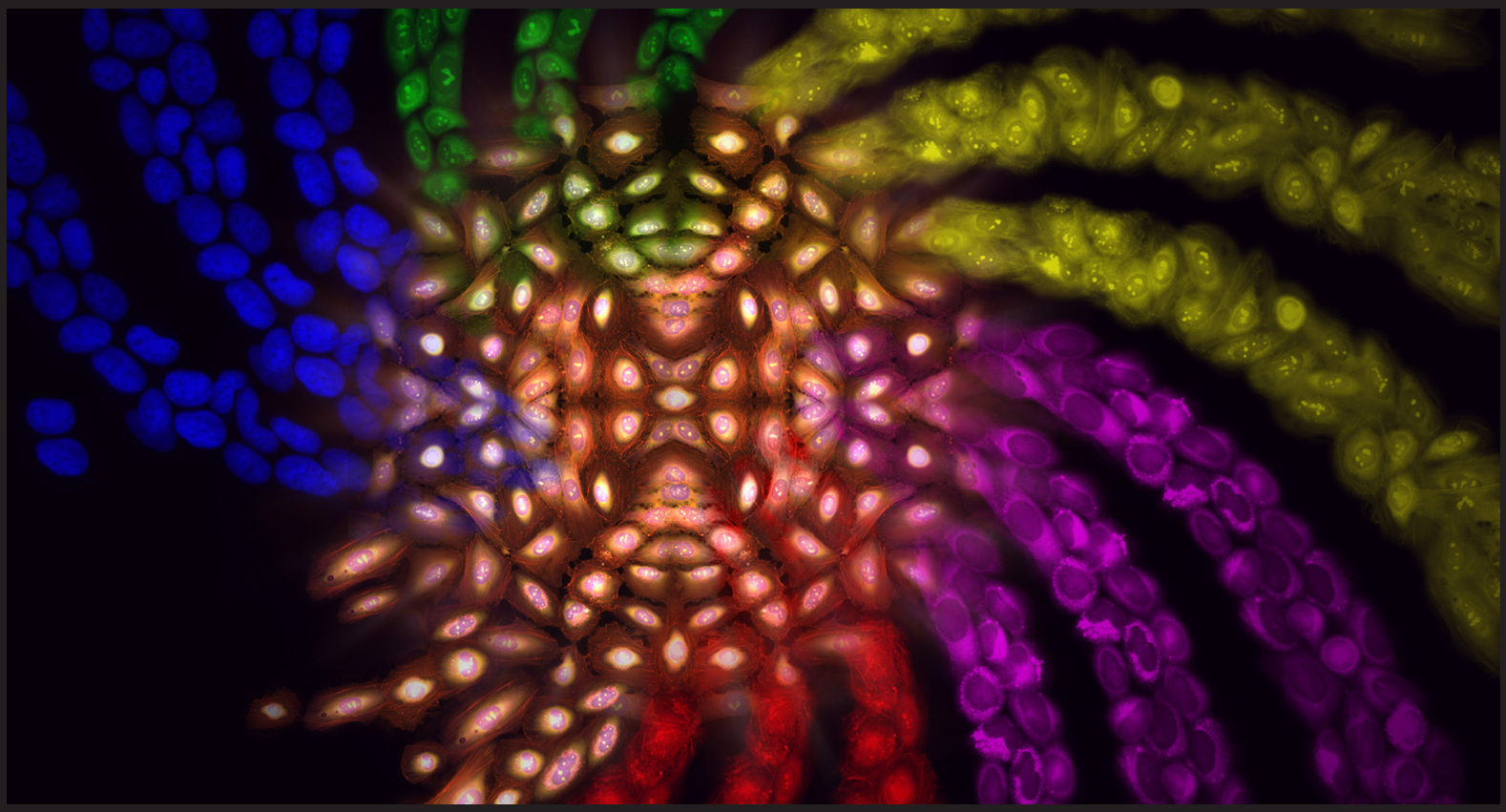

High-Content Screening for Translational Research

ARTICLE COLLECTION

WILEY

CURRENT PROTOCOLS
A Wiley Brand

Sponsored by:
ThermoFisher SCIENTIFIC
The world leader in serving science

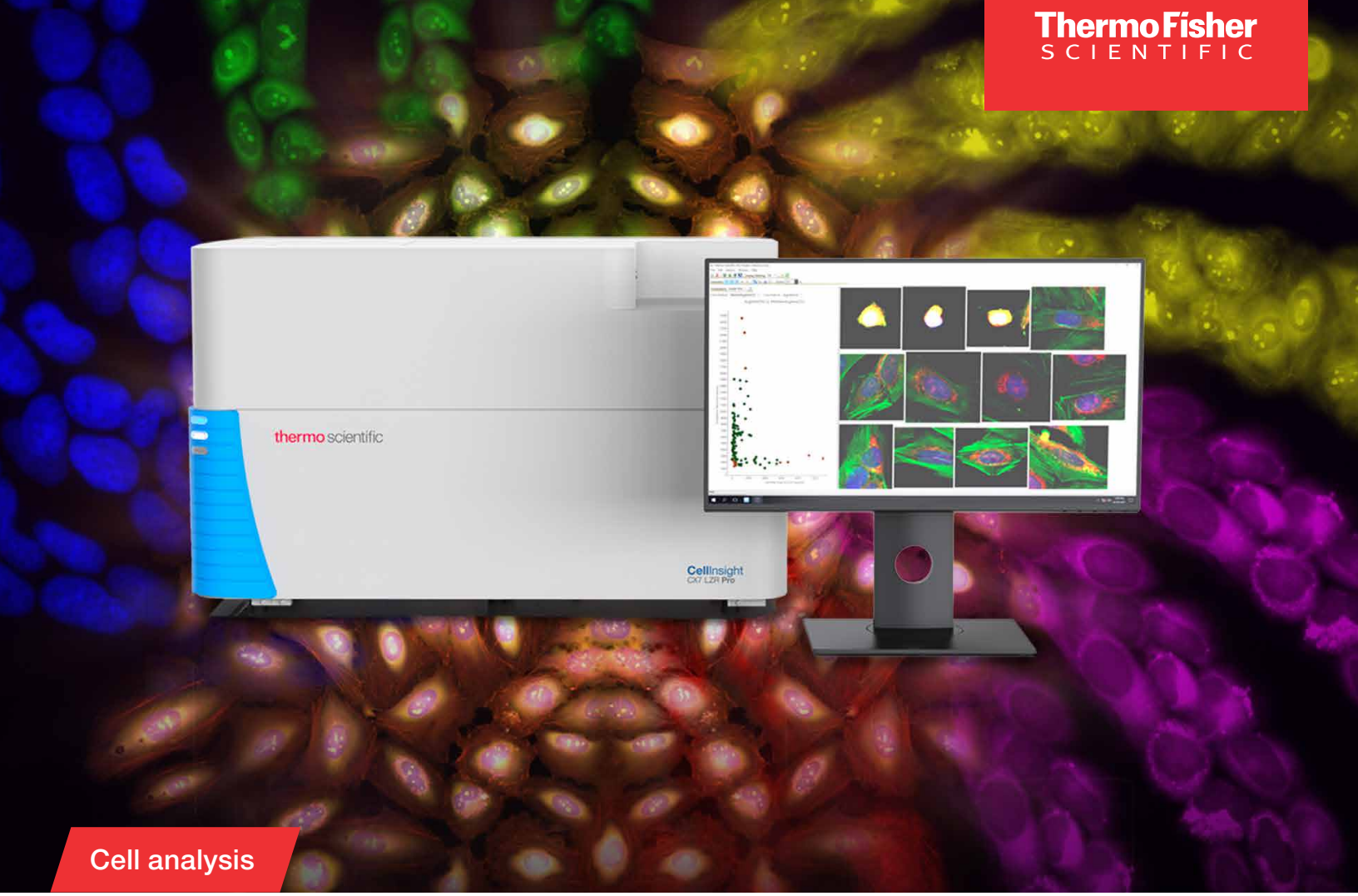

Superior HCS performance for lightning-fast discovery

CellInsight CX7 LZR Pro HCS Platform—fastest time-to-data possible

The Thermo Scientific™ CellInsight™ CX7 LZR Pro High-Content Screening Platform supports your needs with:

- **Clarity**—a new CMOS camera, laser-based fluorescence illumination
- **Precision**—Nipkow spinning-disk confocal technology to create publication-quality images
- **Versatility**—new applications including cell painting and FirePlex® assays

Learn more at **thermofisher.com/hcs**

thermo scientific

Contents

Introduction

From investigating pathways underlying cellular pathologies to the development of novel therapeutics, a significant bottleneck in the research pipeline is the ability to screen vast libraries of gene and proteins for potential candidates. The need to validate targets through experimental replicates places a burden on the investigator to generate a wealth of data in the most reproducible and efficient manner possible. One solution to this problem is the use of high-content screening (HCS) or high-content analysis (HCA) platform, where large numbers of cells are examined using automated workflow and mathematical algorithms to identify and collect imaging-based data in an unbiased manner.

At the forefront of this approach is the Thermo Scientific™ CellInsight™ CX7 HCS Platform. This platform combines confocal, widefield and brightfield imaging modes into one system along with advanced algorithms to allow for deep interrogation of single cells. The CellInsight™ CX7 platform can image cells across multiple preparations, from fixed samples to live cells to complex structures such as organoids. This allows scientists across a wide range of life science disciplines to rapidly and precisely image thousands of cells in a fraction of the time of using conventional microscopy, without any reduction in the depth of data obtained.

In this article collection, we present examples of how high-content screening and analysis can be applied to various research areas, from understanding brain development to the discovery of novel targets for advanced cancer therapeutics. In each article, high content screening was crucial to the advances made.

In our first article, Pirozzi et al (2021), describes the novel discovery of a new genetic variant of *CCDN2* linked in three unrelated families that results in abnormal brain growth and development. They utilized the CellInsight™ CX7 HCS platform to conduct high-content imaging of tens of thousands of cells from patient fibroblast lines for markers of proliferation and mTOR hyperactivation. They found that the novel variant, which impacted the proximal region of the gene, did not cause the same morphological and functional changes as the distal region gene variant. These findings stand to expand the role of the *CCDN2* gene in the axis of the pathways underlying brain growth.

Next, Izmirly *et al* (2022) examined the impact of SARS-CoV-2 vaccination on the disease status of patients with pre-existing systemic lupus erythematosus (SLE) infection. High-content screening of a microneutralization assay for SARS-CoV-2 was utilized to find that SLE patients displayed a significantly decreased antibody response to vaccination compared to controls. These results indicate that specific vaccination protocols for patients on immunosuppressive regimes may need to be developed.

Our third article is Du et al (2018), in which the role of DNA damage-inducible transcript 4 (DDIT4) in the pathology of gastric cancer was investigated. It was determined that DDIT4 is upregulated in gastric cancer cell lines, indicating it could be a druggable target for intervention. It was previously reported that DDIT4 regulates mTOR activity, a pathway commonly impacted in cancer. Through high content screening methods, they found that in the presence of the common anticancer drug 5-fluorouracil (which targets the mTOR pathway), downregulation of DDIT4 reduced cell growth in gastric cancer cell lines indicating this gene can contribute to the sensitivity of gastric cancer to therapeutics.

Lastly, Zecchin et al (2020) performed a whole-genome screen for novel therapeutic targets for triple-negative breast cancer (TNBC). To do so, they infected cancer cells with a screening library of shRNA to identify gene candidates. This identified 96 candidate genes for which CRISPR-Cas9 KO cell lines were generated, utilizing the high-content imaging capabilities of the platform to measure phosphor-S6 levels by fluorescence imaging. This screen identified genes encoding beta and gamma subunits of GPCRs and EGFR (a receptor tyrosine kinase) as part of the pathway underlying resistance to PI3K inhibitor treatment of TNBC. Identifying receptor pathways such as this can lead to new combinatorial treatments for breast cancer.

This article collection provides just a sample of the capabilities and research results that the CellInsight™ CX7 High-Content Screening Platform can produce. We hope that this article collection prompts you to consider how HCS can empower your biological research or drug development pipeline. For more information and testimonials regarding the platform, we encourage you to visit the CX7 High-Content Screening Platforms on the Thermofisher.com website.

By Jeremy Petravicz, PhD, Editor,
Current Protocols

References

Pirozzi, F., et al. (2021), Proximal variants in CCND2 associated with microcephaly, short stature, and developmental delay: A case series and review of inverse brain growth phenotypes. *American Journal of Medical Genetics Part A*, 185A: 2719–2738. https://doi.org/10.1002/ajmg.a.62362

Izmirly, P.M., et al. (2022), Evaluation of Immune Response and Disease Status in Systemic Lupus Erythematosus Patients Following SARS–CoV-2 Vaccination. *Arthritis Rheumatol*, 74: 284-294. https://doi.org/10.1002/art.41937

Du, F., et al. (2018), DDIT4 promotes gastric cancer proliferation and tumorigenesis through the p53 and MAPK pathways. *Cancer Communications*, 38: 1-14 45. https://doi.org/10.1186/s40880-018-0315-y

Zecchin et al. (2020), Combined targeting of G protein-coupled receptor and EGF receptor signaling overcomes resistance to PI3K pathway inhibitors in PTEN-null triple negative breast cancer. *EMBO Mol Med* 12: e11987 https://doi.org/10.15252/emmm.202011987

Received: 7 April 2021 | Revised: 30 April 2021 | Accepted: 4 May 2021

DOI: 10.1002/ajmg.a.62362

RAPID COMMUNICATION

AMERICAN JOURNAL OF medical genetics PART A WILEY

Proximal variants in *CCND2* associated with microcephaly, short stature, and developmental delay: A case series and review of inverse brain growth phenotypes

Filomena Pirozzi[1] | Benson Lee[2] | Nicole Horsley[1] | Deepika D. Burkardt[3] | William B. Dobyns[4] | John M. Graham Jr[5] | Maria L. Dentici[6,7] | Claudia Cesario[8] | Jens Schallner[9] | Joseph Porrmann[10] | Nataliya Di Donato[10] | Pedro A. Sanchez-Lara[5] | Ghayda M. Mirzaa[1,11,12,13]

[1]Center for Integrative Brain Research, Seattle Children's Research Institute, Seattle, Washington, USA

[2]Division of Medical Genetics, Department of Medicine, Veterans Affairs Greater Los Angeles Healthcare System, Los Angeles, California, USA

[3]National Human Genome Research Institute, National Institutes of Health, Bethesda, Maryland, USA

[4]Division of Genetics and Metabolism, Department of Pediatrics, University of Minnesota, Minneapolis, Minnesota, USA

[5]Medical Genetics Institute, Cedars-Sinai Medical Center, David Geffen School of Medicine at UCLA, Los Angeles, California, USA

[6]Medical Genetics Unit, Academic Department of Pediatrics, Bambino Gesù Children's Hospital, IRCSS, Rome, Italy

[7]Genetics and Rare Diseases Research Division, Bambino Gesù Children's Hospital, IRCSS, Rome, Italy

[8]Translational Cytogenomics Research Unit, Bambino Gesù Children's Hospital, IRCCS, Rome, Italy

[9]Department of Neuropediatrics, School of Medicine, Carl Gustav Carus, TU Dresden, Dresden, Germany

[10]Institute for Clinical Genetics, University Hospital, TU Dresden, Dresden, Germany

[11]Division of Medical Genetics, Department of Pediatrics, University of Washington, Seattle, Washington, USA

[12]Brotman-Baty Institute for Precision Medicine, Seattle, Washington, USA

[13]Institute for Stem Cell and Regenerative Medicine, University of Washington, Seattle, Washington, USA

Correspondence
Filomena Pirozzi and Ghayda M. Mirzaa, Center for integrative Brain Research, Seattle Children's Research Institute, Seattle, WA, USA.
Email: filomena.pirozzi@seattlechildrens.org and ghayda.mirzaa@seattlechildrens.org

Funding information
Brotman-Baty Institute; German Research Foundation, Grant/Award Number: DI 2170/3-1; Jordan's Guardian Angels; Sunderland Foundation

Abstract

Cyclin D2 (CCND2) is a critical cell cycle regulator and key member of the cyclin D2-CDK4 (DC) complex. De novo variants of *CCND2* clustering in the distal part of the protein have been identified as pathogenic causes of brain overgrowth (megalencephaly, MEG) and severe cortical malformations in children including the megalencephaly-polymicrogyria-polydactyly-hydrocephalus (MPPH) syndrome. Megalencephaly-associated *CCND2* variants are localized to the terminal exon and result in accumulation of degradation-resistant protein. We identified five individuals from three unrelated families with novel variants in the proximal region of *CCND2* associated with microcephaly, mildly simplified cortical gyral pattern, symmetric short stature, and mild developmental delay. Identified variants include de novo frameshift variants and a dominantly inherited stop-gain variant segregating with the phenotype. This is the first reported association between proximal *CCND2* variants and microcephaly, to our knowledge. This series expands the phenotypic spectrum of *CCND2*-related disorders and suggests that distinct classes of *CCND2* variants are associated with reciprocal effects on human brain growth (microcephaly and megalencephaly

due to possible loss or gain of protein function, respectively), adding to the growing paradigm of inverse phenotypes due to dysregulation of key brain growth genes.

KEYWORDS
cyclin D2, inverse phenotypes, megalencephaly, megalencephaly-polymicrogyria-polydactyly-hydrocephalus syndrome (MPPH syndrome), microcephaly

1 | INTRODUCTION

Overgrowth syndromes are disorders characterized by cellular hyperplasia and/or hypertrophy, which may involve one or more of the three embryonic tissue layers (endoderm, ectoderm, or mesoderm) and present clinically with generalized or segmental overgrowth of the brain or the body (Burkardt et al., 2019; Tatton-Brown & Weksberg, 2013). Undergrowth syndromes or syndromes of growth restriction, on the other hand, are groups of disorders characterized by tissue hypoplasia and growth restriction. Collectively, these syndromes may manifest with localized or generalized growth abnormalities and display considerable heterogeneity in onset, tissue involvement and distribution among other features (Grissom & Reyes, 2013).

The Cyclin D2 Cyclin-dependent kinases 4 (CDK4) family of genes regulates the cell cycle by modulating the G1-to-S phase transition, critical for cell proliferation and development (Jeong et al., 2016). Posttranslational modification by phosphorylation of CCND2, downstream of the phosphatidylinositol 3-kinase (PI3K)/ AK murine Thymoma (AKT)/mammalian target of the rapamycin (MTOR)

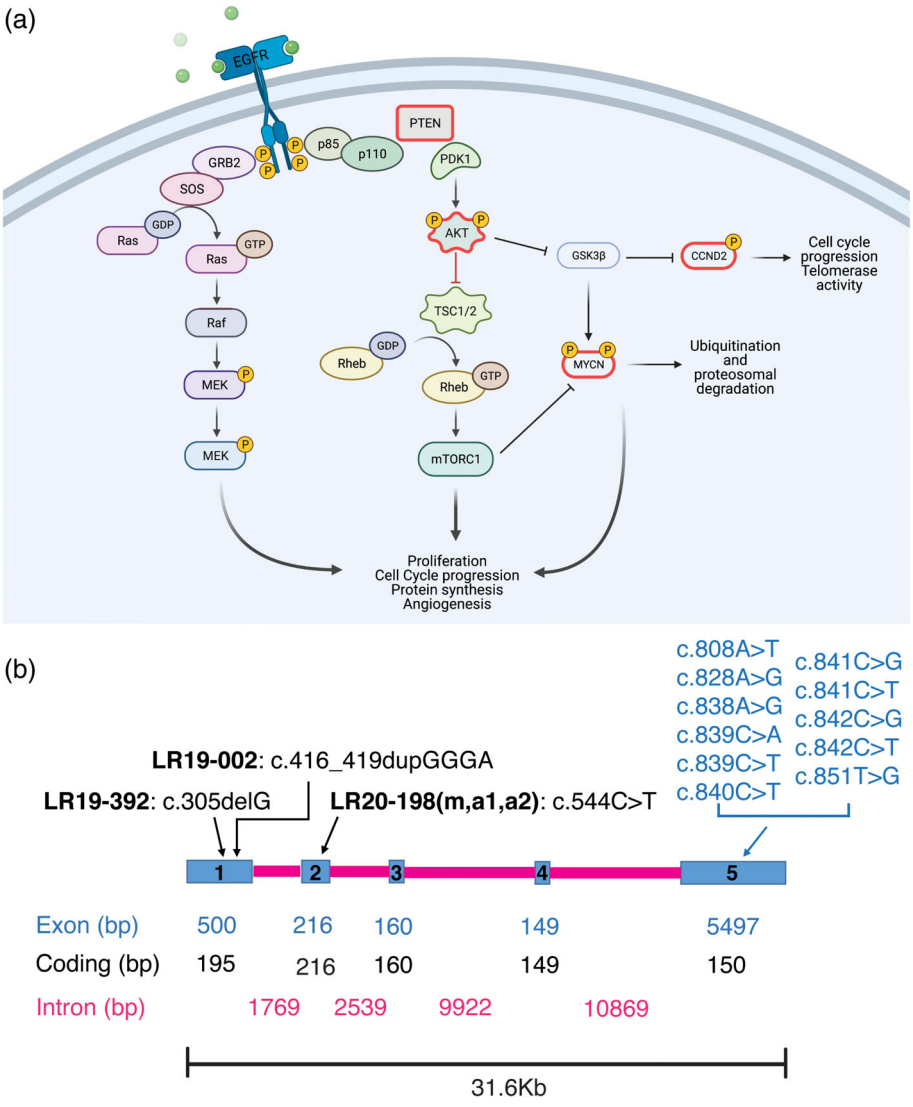

FIGURE 1 *CCND2* gene diagram and role in cell signaling. (a) A schematic representation of the PI3K-AKT-MTOR pathway and its' interaction with the CCND2 protein. Proteins outlined in magenta are the ones with known gain of function and loss of function mutations leading to opposite phenotypes (*PTEN*, *AKT3*, *MYCN*, *CCND2*). Created with BioRender.com. (b) Scheme of the human *CCND2* gene (*Homo sapiens* chromosome 12, GRCh38.p12 CCND2: NC_000012.12 mRNA NM_001759.4 protein NP_001750.1). Blue rectangles represent exons (1–5), while magenta lines represent introns. Exon, coding and intron base pairs length (bp) is shown in the relative colors. Above the gene scheme, putative *CCND2* loss of function (LOF, in black) reported here, and previously published gain of function (GOF, in blue) mutations are reported

signaling pathway inhibits its binding to the transcription factor E2F, allowing the cell to exit the G1 phase of the cell cycle (Becker et al., 2010; Bouchard et al., 1999; Sicinski et al., 1996). A schematic representation of the PI3K-AKT-MTOR pathway and CCND2 interaction is provided in Figure 1a. Cyclin D2 has well-studied roles in brain development and is expressed in dividing cells derived from neuronal precursors in the adult hippocampus (Ross et al., 1996). Hyperactivation of CCND2 has been linked to hematologic malignancies and increased proliferation in human cancer cell lines (Hung et al., 2018; Murai et al., 2001). Further, genetic variants of *CCND2* (MIM #123833), as well as two other key PI3K-AKT-MTOR pathway genes, namely *AKT3* and *PIK3R2*, have been identified as pathogenic causes of the megalencephaly-polymicrogyria-polydactyly-hydrocephalus (MPPH) syndrome (Hiraiwa et al., 2021; G. Mirzaa et al., 2014). MPPH is a rare megalencephaly (MEG) syndrome characterized by congenital or early postnatal brain overgrowth and cortical malformations, most commonly polymicrogyria (PMG). MPPH is also associated with variable degree of ventriculomegaly, with 40–50% of affected individuals progressing to hydrocephalus and necessitating surgical intervention (G. Mirzaa et al., 1993). Most affected children have mild to severe intellectual disability and oromotor dysfunction, including expressive language or speech delays, difficulties handling oral secretions, and dysphagia; with seizures reported in at least 50% of individuals. *CCND2*-related MPPH is characterized by severe and widespread polymicrogyria, typically bilateral perisylvian PMG (BPP) extending to the frontal and/or occipital lobes and correlating with increased severity of epilepsy and intellectual disability (G. Mirzaa et al., 2014). An additional report of a child with the MPPH phenotype in association with the *CCND2* variant, p.Thr280Ile, further expanded the phenotypic spectrum as this individual had additional brain abnormalities including hippocampal hypoplasia with malrotation, diffuse hypomyelination, and abnormalities of the midbrain and cerebellum (Cappuccio et al., 2019).

While overexpression and hyperactivation of CCND2 have been identified in humans and mice, the effects of CCND2 deficiency or loss of function have not been studied in humans. In mice, Ccnd2 knock-out leads to lack of cerebellar stellate interneurons (Garthe et al., 2014; Glickstein et al., 2007) and striking microcephaly (Huard et al., 1999). *CCND2* haploinsufficiency due to 12p13.32 contiguous microdeletion syndromes has been reported in individuals with microcephaly, although the critical region for this microdeletion also encompasses other key genes (Firth et al., 2009; Leyser et al., 2016). In this study, we describe three novel proximal variants in *CCND2* in five individuals from three unrelated families presenting with microcephaly, symmetric short stature, hypotonia and developmental delays. This series suggest that frameshift and stop-gain variants in the proximal portion of *CCND2* are linked to human microcephaly and adds *CCND2* to the growing list of genes associated with reciprocal brain growth dysregulation. All microcephaly- and megalencephaly (including MPPH)-associated variants in *CCND2* identified to date are schematically shown in Figure 1b. Examples of reciprocal gain and loss of protein function resulting in inverse phenotypes are seen in a multitude of abnormal growth syndromes, including mutations in other genes involved in cell growth and cell cycle regulation such as *AKT3*, *PTEN*, *NSD1*, and *MYCN*. These inverse brain growth phenotypes due to reciprocal gene defects are summarized in Table 1 and discussed in depth in the literature review we provide here.

2 | METHODS

2.1 | Human subjects and cell lines

Families were identified through our clinical and research programs, personal communication, as well as the MatchMaker Exchange (MME) including GeneMatcher (http://www.genematcher.org) (Sobreira et al., 2015). Informed consent for publication and analysis of photos, imaging and clinical data was obtained from the patients' legal guardians under an IRB approved protocol at Seattle Children's Hospital (IRB#13291). Brain magnetic resonance imaging (MRI) studies were performed on three individuals (LR19-002, LR20-198a1, and LR20-198a2) and reviewed by the investigators. Fibroblast cell lines were established from one of the patients (LR19-392) with the c.305delG, p.G102Vfs*17 variant (referred to as LR19-392-MIC throughout the manuscript), and compared to a MEG/MPPH fibroblast cell line from a previously published patient (LR07-041) with the *CCND2*, c.839C>A, p.T280N variant (referred to as LR07-041-MEG hereon) (G. Mirzaa et al., 2014), as well as fibroblasts obtained from a healthy unrelated control (UW402-4-CTRL).

2.2 | Western blot analysis

Fibroblast cell lines (LR19-392-MIC, LR07-041-MEG, and UW402-4-CTRL) were expanded to six confluent T-75 flasks each before protein extraction. Cell culture flasks were placed on ice and washed once with 10 mL ice cold TBS. Flasks were then incubated on ice for 5 min with 500 μl cold RIPA buffer (Thermo Scientific, 89900) containing phosphatase and protease inhibitors (Thermo Scientific, 78,430, P5726, and P2850), cells were scraped and collected in 15 mL conical tubes and agitated for 30 minutes at 4C before being centrifuged at 14,000*g* for 15 min. The resulting supernatant was aliquoted into 0.2 mL tubes, snap frozen with liquid N2, and stored at −80°C. Protein concentrations were assessed via the standard Bicinchoninic Acid (BCA) Assay (Thermofisher, 23227). Equal amounts of protein extracts (10 and 20 μg) were heated to 95°C for 5 mins with NuPAGE® LDS Sample Buffer (4×) (Thermofisher, NP0007) and run on NuPAGE® Novex® 4–12% Bis-Tris gels (Thermofisher, NP0326BOX), together with a protein ladder (Pageruler prestained protein ladder, Thermofisher, 26617). Proteins were transferred to nitrocellulose membranes (Thermofisher, 77010). Due to low expression of CCND2 in human fibroblasts, we used 40 μg of protein extracts for its detection via Western Blot analysis. Membranes were blocked at room temperature for 1 h in blocking solution (3% BSA and 10% Donkey Serum in TBS with 0.1% Tween-20). For the CCND2 antibody, the blocking buffer contained 5% nonfat milk in addition to

TABLE 1 A summary of clinical and molecular features of inverse brain growth phenotype due to variants in *CCND2*, *AKT3*, *PTEN*, *NSD1*, *MYCN*, *EZH2*, and *MIR17HG*

Gene	Megalencephaly/macrocephaly Disease (OMIM)	Protein function	Clinical features	Inheritance	Type of variants	Microcephaly Disease (OMIM)	Protein function	Clinical features	Inheritance	Type of variants
CCND2	MPPH3 (#615938)	Gain	Megalencephaly, postaxial polydactyly, hypotonia, epilepsy, intellectual disability, oromotor dysfunction, polymicrogyria	De novo/AD	Missense, nonsense	Microcephaly	Loss[a]	Microcephaly, symmetric short stature, hypotonia, mild intellectual disability, mild motor delay	*De novo*/AD	Missense, small indels
AKT3	MPPH2 (#615937)	Gain	Megalencephaly, polymicrogyria/cortical dysplasia, postaxial polydactyly, hypotonia, epilepsy, intellectual disability, oromotor dysfunction, connective tissue laxity, vascular malformations	De novo/AD	Missense, duplication	Postnatal microcephaly	Haploin sufficiency/ loss	Microcephaly, callosal abnormalities, seizures, hypotonia, dysmorphic features	*De novo*/AD	Microdeletion 1q43-q44
PTEN	Cowden syndrome (CS), Bannayan–Riley–Ruvalcaba syndrome (BRRS); Lhermitte-Duclos disease (LDD); (#158350)	Loss	Megalencephaly, facial trichilemmomas, acral keratoses, papillomatous papules, hamartoma, increased risk for breast, thyroid, and endometrial carcinoma; hamartomatous polyps of the gastrointestinal tract, mucocutaneous lesions, developmental delay, lipomas, hemangiomas	De novo/AD	Missense, nonsense, s mall/large deletions	Microcephaly	Gain	Primary microcephaly, autism spectrum disorder, intellectual disability	AD	Microduplication 10q23.31
	Autism spectrum disorder with macrocephaly (#605309)	Loss	Megalencephaly, abnormal facial features, and delayed psychomotor development resulting in autistic behavior or mental retardation	De novo/AD	Missense, nonsense, small/large deletions					
NSD1	Sotos syndrome (#117550)	Loss	Megalencephaly, somatic overgrowth, dysmorhpic facial features, cardiac issues, skeletal issues, renal anomalies, developmental delay/ intellectual disability	De novo/AD	Missenese, nonsense, splicing defects, frameshift, deletions	Microcephaly	Gain	Microcephaly, short stature, seizures, developmental delay/intellectual disability, dysmorphic facial features	*De novo*/AD	Microduplication 5q35
MYCN	*MYCN* related megalencephaly syndrome	Gain	Brain abnormalities (megalencephaly, ventriculomegaly, hypoplastic corpus callosum); Intellectual disability, polydactyly; neuroblastoma	De novo	Missense (c.173C>T)	Feingold syndrome type 1 (#164280)	Loss	Microcephaly; Limb abnormalities (clinodactyly, syndactyly, thumb hypoplasia); Esophageal and or duodenal atresia; Learning disabilities; Characteristic facial features (micrognathia, short palpebral fissures)	AD/unknown *de novo*	Nonsense, missense, large deletions, partial and entire gene deletions

TABLE 1 (Continued)

Gene	Megalencephaly/macrocephaly Disease (OMIM)	Protein function	Clinical features	Inheritance	Type of variants	Microcephaly Disease (OMIM)	Protein function	Clinical features	Inheritance	Type of variants
EZH2	Weaver syndrome (#277590)	Loss	Megalencephaly, overgrowth, distinctive facial gestalt, accelerated bone maturation, developmental delays	De novo	Missense	Microcephaly and developmental delays	Gain	Growth failure, hypotonia, "clover-leaf" shaped skull, large anterior fontanelle, sparse eyebrows, upslanting palpebral fissures, and small ears, developmental delays	*De novo*	Missense
MIR17HG	*MIR17HG* related overgrowth syndrome	Gain	Megalencephaly, developmental delay, skeletal and digital abnormalities, tall stature	De novo	13q31.3 microduplications	Feingold syndrome type 2 (#614326)	Loss	Microcephaly, brachymesophalangy, toe syndactyly, short stature, cardiac anomalies, growth hormone deficiency, aortic dilation, phalangeal joint contractures, memory, and sleep problems	*De novo*	13q31.3 microdeletions

Notes: When available, the OMIM number is listed, otherwise the disorder has not yet been described in OMIM.
Abbreviations: AD, autosomal dominant; IUGR, intrauterine growth restriction; MPPH, megalencephaly-polymicrogyria-polydactyly-hydrocephalus syndrome; UK, unknown.
[a]Predicted loss of function due to premature stop codon based on the five cases reported here.

3% BSA and 10% Donkey Serum to improve specificity. Membranes were incubated with primary antibody diluted in blocking solution overnight at 4C on an orbital shaker. Primary antibodies were diluted as follows: 1:200 for CCND2 (D52F9, Cell Signaling), 1:2500 for pAKT (Cell signaling, C31E5E), 1:2500 for pan-AKT (Cell Signaling, C67E7), 1:1000 for pS6 (Cell Signaling, 2215), and 1:5000 for β-actin (Abcam, ab8226). Membranes were washed three times for 15 min at room temperature in TBS-Tween 0.1% then incubated with secondary antibody in blocking solution for 1 h at RT. The secondary antibodies Donkey Anti-Mouse IgG H&L HRP (Abcam, ab205724) or Donkey Anti-Rabbit IgG H&L HRP (Abcam, ab97064) were used at 1:10,000 in blocking solution. After three washes at room temperature with TBS-Tween 0.1%, protein signal was detected with Pierce™ ECL Western Blotting Substrate (Thermo Scientific, 32109) and visualized using a ChemiDoc-It®2810 Imager (UltraViolet Products Ltd., Cambridge, UK). If necessary, membranes were stripped and re-probed, probing the antibody for the protein with the weakest signal first, following standard protocols. Six independent experiments were performed for each antibody and images were analyzed, quantified, and normalized against B-Actin using ImageJ24. Statistical analysis and graphs were generated using GraphPad Prism version 9.0.2.

2.3 | High-content imaging

Fibroblast cell lines LR19-392 MIC, LR07-041 MEG, and UW402-CTRL were passaged in an optical 96 well plate coated with 0.1% porcine gelatin and cultured for 48 hours before fixing with cold 4% PFA in TBS (20 min at room temperature). Four wells per cell line were used for immunostaining. Cells were washed twice with cold TBS and permeabilized with TBS-Tween 0.1% for 5 min at room temperature. Immunostaining was performed using standard protocols. Briefly, cells were incubated for 1 hour at room temperature with blocking buffer (TBS-Tween 0.1% with 10% Donkey serum) and then incubated overnight with primary antibodies at 4C. Primary antibodies were diluted as follows: mouse anti-Ki-67 1:300 (Cell Signaling, 9449S) and rabbit anti-pS6 1:100 (Cell Signaling, 2215S). The following day, cells were washed three times with TBS-Tween 0.1% for 15 min and incubated with secondary antibodies diluted in blocking buffer for 1 h at room temperature. Secondary antibodies Donkey Anti-mouse Alexa 594 (Abcam, ab150112) and Donkey Anti-Rabbit Alexa 488 (Abcam, ab150065) and were used at 1:1000 dilution. Cells were washed three times in TBS-Tween 0.1%, followed by one wash in TBS, and stored in Glycerol-TBS (70:30) for acquisition and long-term storage. Image acquisition was performed using the CellInsight CX7 LZR system (Thermofisher). Fifteen fields for each of the 4 replicate wells per cell lines were acquired at 10× and 20× magnification. Images (10× magnification) were analyzed and quantified with a custom algorithm using the HCS Studio software. Statistical analysis was performed using GraphPad Prism version 9.0.2. and specific tests used are described in figure legends.

TABLE 2 Summary of clinical and molecular features for individuals with microcephaly and novel *CCND2* variants

		LR19-002	LR19-392	LR20-198 m	LR20-198a1	LR20-198a2
Genetic testing	Identified variant	*CCND2*: NM_001759.4: c.416_419dupGGGA, p.L141GfsX19	*CCND2*: NM_001759.4:c.305delG, p.G102VfsX17	*CCND2*: NM_001759.4:c.544C>T, p.Q182X (het)		
	Molecular methods and other molecular findings [inheritance]	Exome sequencing; *GBA* (c.882T>G, p.H294Q), het, VUS [pat]; *TENM1* (c.679 C>A, p.P227T), VUS, [mat]	NGS panel; no	Array CGH, targeted sequencing, arr 18q12.3 (37.877.518-37.961.503)x3 (hg18)	Exome sequencing, Array CGH, arr 18q12.3 (37.877.518-37.961.503)x3mat (hg18)	Array CGH, Targeted sequencing, arr 8q23.1 (106.455.702-107.566.961) x3pat,18q12.3 (37.877.518-37.961.503)x3mat (hg18)
Demographics	Sex	M	F	F	M	F
	Age at last assessment	7m	12y2m	30y	12y11m	6y8m
	Ethnicity	ND	ND	Caucasian (Germany)	Caucasian (Germany)	Caucasian (Germany)
	Notable family history	Non-consanguineous, conceived via intrauterine insemination, family history unremarkable	Non-consanguineous, family history unremarkable	Father has boderline ID, short stature and microcephaly without genetic diagnosis	See LR20-198 m. One sibling and two maternal half siblings show normal OFC and normal development and do not carry CCND2 variant	See LR20-198a1
Pregnancy and birth	Pregnancy	G1P1 mother, suspected preeclampsia, vaginal bleeding, IUGR at 32-33gw	G2P2, IUGR at end of second trimester	G1P1	G1P1	G4P3
	Gestational age (weeks/days)	35 + 6	39 + 0	ND	38 + 5	37 + 5
	Birth weight (%le/z-score)	1870 g (2.13%, −2.05 SD)	2320 g (3%, −1.8 SD)	ND	2900 g (10–25%, −1.2 SD)	2480 g (3%, −1.8 SD)
	Birth length (%le/z-score)	43.5 cm (3%, − 1.8 SD)	46 cm (3–10%, −1.5 SD)	ND	49 cm (25–50%, −1 SD)	47 cm (10–25%, − 1.3 SD)
	Birth head circumference (% le/z-score)	30.5 cm (3–10%, −1-2 SD)	32 cm (2%, −2 SD)	ND	29.5 cm (<1%, −4.3 SD)	32 cm (2%, − 2 SD)
Growth	Weight at last assessment (%le/z-score)	6.1 kg (0.48%, −2.6 SD)	25.50 kg (<0.1%, −2.8 SD)	85 kg (95%, +1.68 SD)	34.2 kg (5%, −1.7 SD)	15.2 kg (<1%, −2.8 SD)
	Height at last assessment (% le/z-score)	64.5 cm (5%, − 1.6 SD)	140.5 cm (7%, −1.4 SD)	150 cm (2%, −2 SD)	144.5 cm (7%, −1.5 SD)	111 cm (2%, −2 SD)
	Head circumference at last assessment (%le/z-score)	40.2 cm (<1%, −3.1 SD)	48 cm (<1%, −4.3SD)	51 cm (<1%, −3.1 SD)	48 cm (<1%, −4.2 SD)	45.2 cm (<1%, −5 SD)
	Growth failure	Yes	Yes	Yes	No	Yes
Neurologic findings	Degree of developmental delay or ID	N.E.		Mild	Mild	Mild
	Age—1st walked	N.E.	13 m	2 years	12 month	11 month
	Age—1st words	N.E.		Unknown	Unknown	Unknown
	Speech delays	N.E.	Yes	Unknown	Yes (with 3 years less than 100 words and two-word-sentences)	Yes
	Seizures	No	No	No	No	No
	EEG findings	N.E.	N.E.	N.E.	normal	yes, among others occipital epileptic potentials
	Tone abnormalities	Hypotonia	No	N.E.	No	No

TABLE 2 (Continued)

		LR19-002	LR19-392	LR20-198 m	LR20-198a1	LR20-198a2
	Brain MRI findings	Microcephaly with a mildly simplified gyral pattern	Microcephaly with a mildly simplified gyral pattern	N.E.	Normal	Normal
	Autism	N.E.	No	N.E.	No	No
	ADHD	N.E.	Yes, mild	N.E.	Suspected	N.E.
	Other behavioral issues	N.E.	No		aggressive, impulsive and antisocial behavior	recurring (breath-holding spells), impusive behavior, reduced interaction with peers
	Other neurologic findings	No	No	No	No	No
	Formal developmental or autism assessments	N.E.	Special school	Attended a special school	Attended a special school	Bayley II (23 month): in the lower standard range
Other findings	Dysmorphic facial features	Mild right occipital flattening	Large ears, short philtrum, incomplete single transverse right palmar crease	Sloping forehead, broad nasal tip, upslanting palpebral fissures, long philtrum, thin upper lip vermilion	Sloping forehead, broad nasal base, broad nasal tip, long philtrum, thin upper lip vermilion	Sloping forehead, broad nasal tip
	Heart	N.E.	N.E.	N.E.	N.E.	N.E.
	Eyes	N.E.	Mild myopia	N.E.	N.E.	Normal
	Urogenital system	N.E.	N.E.	N.E.	N.E.	N.E.
	Skeletal	N.E.	Bone age delayed at 2y10m, normalized later	N.E.	Pes planus	Talus obliqus and pes planus unilateral
	GI	N.E.	N.E.	N.E.	N.E.	Nutritional difficulties
	Other medical issues	Mild motor delays at birth, responded well to physical therapy	No	Bilateral inguinal hernia after birth	Asphyxia, anchyloglossia	Respiratory adaptation disorder with CPAP-therapy, failure to thrive

Notes: The table summarizes the clinical features, growth data, and family history for the five individuals with proximal *CCND2* frameshift or stop-gain variants.
Abbreviation: N.E., not evaluated.

3 | RESULTS

3.1 | Clinical reports

Clinical and genetics features for all patients are summarized in Table 2.

3.1.1 | Patient LR19-002

This 7-month-old boy was referred to the genetics clinic for microcephaly, intrauterine growth restriction (IUGR), hypotonia, and mild motor delays. He was the first child of non-consanguineous parents of Armenian descent, a 30-year-old G1P1 mother and 30-year-old father and conceived by intrauterine insemination. Pregnancy was complicated by suspected preeclampsia and vaginal bleeding. No teratogenic exposures were reported. Family anamnesis was unremarkable with no history of microcephaly, delayed growth, or development. At 32–33 weeks of gestation, IUGR and placental insufficiency were reported. The boy was delivered at 35 + 5 weeks of gestation by a scheduled caesarian section. Birth weight was 1870 grams (2nd centile, −2.05 SD), length 42.5 cm (3rd centile, −1.8 SD) and occipitofrontal circumference (OFC) 30.5 cm (3–10th centile, − 1-2 SD). OFC measured again at 36 weeks was 29.9 cm (1–2nd centile, −2.25 SD). The child was also diagnosed with gastroesophageal reflux and allergic colitis. At age 7 months, he was sitting up without assistance, had begun rolling in both directions, grabbed objects with both hands and was beginning to vocalize sounds. OFC was 40.2 cm (<1st centile, − 3.1 SD), weight was 6.1 kg (<1st centile, −2.6 SD), and length was 64.5 cm (5th centile, −1.6 SD). His body habitus was proportionately small with symmetric limbs, clinically apparent microcephaly with mild right occipital flattening but otherwise normal skull shape and no other notable dysmorphic features.

Brain magnetic resonance imaging (MRI) without contrast performed at age 6 months revealed apparent microcephaly with a diffusely simplified gyral pattern (Figure 2a–c). An echocardiogram performed at age 4 months revealed a small patent foramen ovale versus secundum atrial septal defect with left to right shunting.

Chromosomal microarray analysis was normal. Trio exome sequencing on buccal samples identified a heterozygous de novo variant in *CCND2* (NM_001759.4:c.416_419dupGGGA, p.L141GfsX19) (Figure 1b). This frameshift variant causes a premature stop codon at position 19 of the new reading frame and is predicted to cause a loss of normal protein function either through protein truncation or nonsense-mediated mRNA decay. This novel variant has not been observed in over 60,000 apparently normal individuals (Lek et al., 2016) (Table 3). Other reported findings unrelated to the patient's phenotype include a heterozygous paternally-inherited variant of uncertain significance (VUS) in *GBA* (NM_000157.4: c.882T>G, p.H294Q), and a maternally inherited hemizygous VUS in *TENM1* (NM_001163278.1:c.679 C>A, p.P227T) a gene not currently known to be associated with microcephaly or other human Mendelian disorders, but has been reported as possibly associated with cerebral palsy (McMichael et al., 2015), autism spectrum disorder (Yuen et al., 2015), schizophrenia (Gulsuner et al., 2013), and congenital general anosmia (Alkelai et al., 2016).

3.1.2 | Patient LR19-392

This 12-year-old girl presented with a history of IUGR, microcephaly, delayed language skills, mild attention deficit hyperactivity disorder (ADHD), and short stature. She was the second child born to non-consanguineous parents. Family history was unremarkable with no microcephaly, growth, or developmental delay. Pregnancy was uneventful until the end of the second trimester when IUGR was identified. Amniocentesis revealed a normal female karyotype (46,XX). She was delivered at 39 weeks of gestation by scheduled cesarean section due to IUGR. Her birth weight was 2320 grams (3rd centile, − 1.8 SD), length was 46 cm (3–10th centile, −1.5 SD), and OFC was 32 cm (2nd centile, −2 SD). At age 2 years and 10 months, her weight was 9.8 kg (<1st centile, −2.8 SD), length was 89 cm (18th centile, −0.93 SD), and OFC was 43.6 cm (<1st centile, −3.1 SD). Bone age was delayed by 6 months but normalized at later follow-up. Evaluation of growth hormone response to GHRH plus arginine at 8 years of age was normal.

Her motor developmental milestones were within the normal range. She sat without assistance at age 6–7 months and walked unsupported at age13 months. Her language skills were delayed. She had mild attention deficit hyperactivity disorder (ADHD) and attended a special education program at school. Vision assessment revealed mild myopia. At her last evaluation at 12 years and 2 months, weight was 25.50 kg (<1st centile, −2.8 SD), height 140.50 cm (8th centile, −1.42 SD) and OFC was 48 cm (<1st centile, −4.27 SD). Physical examination revealed marked microcephaly with relatively large ears, short philtrum, and an incomplete right single transverse palmar crease.

Head ultrasound performed at birth did not show any structural abnormalities. A brain MRI has not been performed due to the presence of dental braces. An electroencephalogram (EEG) was performed at 12 years and 5 months and was normal.

Targeted multigene NGS panel testing for microcephaly using the NimbleGen SeqCap Target Enrichment kit (Roche) by NextSeq550 Platform (Illumina) revealed a heterozygous de novo variant in *CCND2* (NM_001759.4:c.305delG). This single base deletion is expected to cause a premature stop codon, p.G102Vfsx17 (Figure 1b), with the de novo status confirmed by segregation analysis performed by Sanger sequencing of both parents. This novel variant was not observed in large population cohorts (Table 3). Other microcephaly genes in the panel include *MCPH1*, *WDR62*, *CDK5RAP2*, *CASC5*, *ASPM*, *CENPJ*, *STIL*, *CEP135*, *CEP152*, *CDK6*, *ATR*, *RBBP8*, *CEP63*, *NIN*, and *ATRIP*.

3.1.3 | Family LR20-198

This family includes two siblings: a 12-year-old boy (LR20-198a1) and 6-year-old girl (LR20-198a2) born to their 30-year-old mother (LR20-198 m). LR20-198a1 presented prenatally with IUGR and

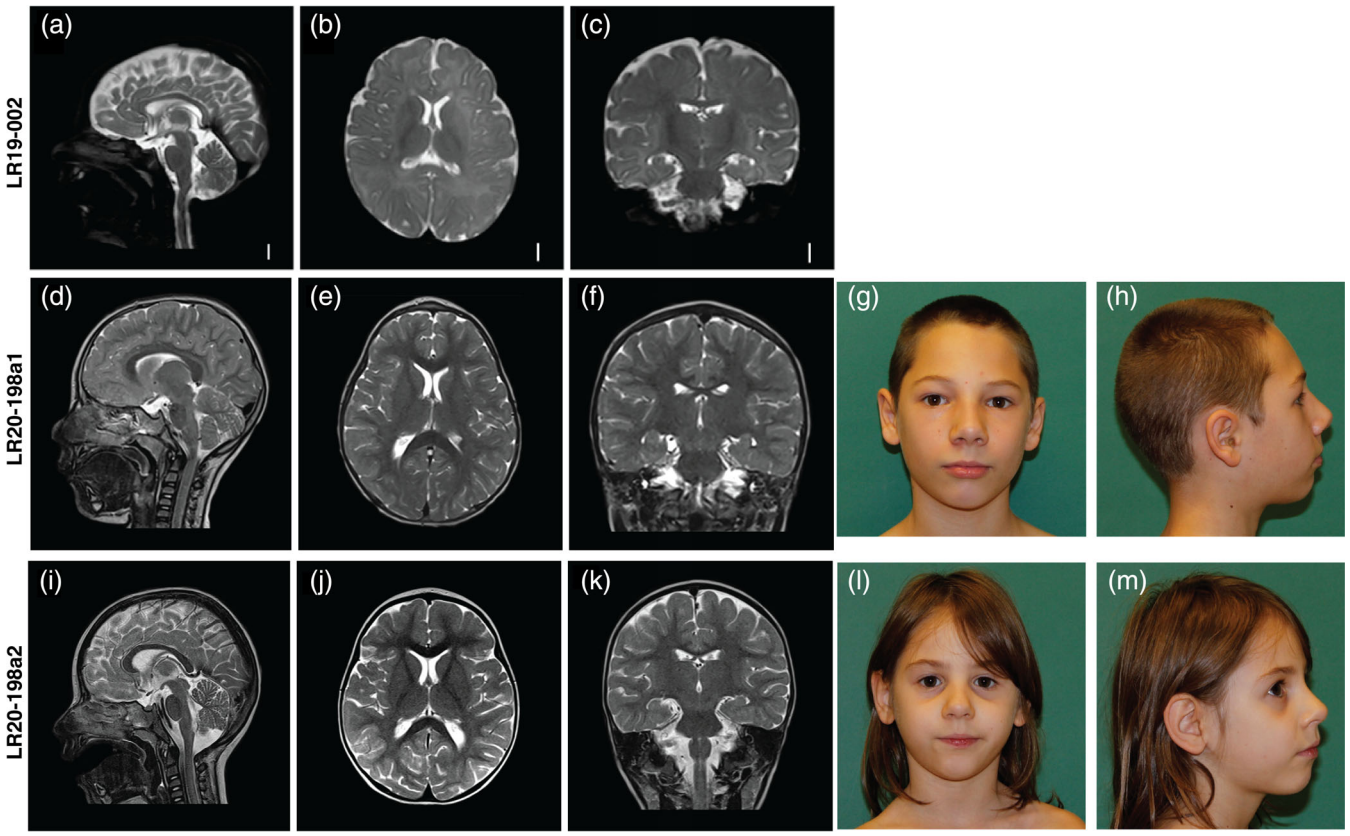

FIGURE 2 Clinical photographs and brain MR images for three individuals with CCND2-associated microcephaly. (a–c) T2-weighted brain MR images of patient LR19-002 at age 6 months. (a) Midsagittal image showing a mildly thin corpus callosum, with a relatively preserved cerebellar vermis; (b) axial image showing an overall simplified gyral pattern with foreshortened frontal lobes, normal ventricles and (c) coronal image showing also an overall simplified gyral pattern. (d–f) MRI of patient LR20-198a1 at age 4 years showing a mildly foreshortened frontal lobe and subtle simplified gyrification with no cortical malformations and no other major anomalies. (g and h) frontal and lateral pictures of individual LR20-198a1. (i–k) MRI of patient LR20-198a2 at age 2 years 5 months showing a normal appearance with no cortical malformations and no other major anomalies. (l and m) frontal and lateral pictures of patient LR10-198a2

TABLE 3 Analysis of variants pathogenicity and frequency in the population

	Variant			Variant frequency		
Gene	CDS	Protein	Mutation Taster	dbSNP	gnomAD (Mut/ref[a])	1000G
CCND2	c.305delG	p.G102Vfsx17	Disease causing	Not present	0/251466	Not present
CCND2	c.416_419dupGGGA	p.L141GfsX19	Disease causing	Not present	0/249026	Not present
CCND2	c.544C>T	p.Q182X	Disease causing	Not present	0/248742	Not present
GBA	c.882T>G	p.H294Q	Disease causing	Not present	0/279868	Not present
TENM1	c.679C>A	p.P227T	Disease causing	Not present	0/156640	Not present

Notes: Genetic variants found in individuals LR19-002, LR19-392, LR20-198 m, LR20-198a1, and LR20-198a2 are listed with their respective prediction of pathogenicity (Mutation Taster) and frequency in the population based on data collected in dbSNP, gnomAD, and 1000 Genome project (1000G) (results as of April 5, 2021).

[a]For gnomAD reference allele frequency, data for the closest variant in the database were used to estimate the coverage of the region.

microcephaly. He was born at 38 + 5 weeks of gestation by emergency cesarean section and had severe perinatal asphyxia (Apgar scores of 1, 6, and 9 at 1, 5, and 10 min, respectively). Developmental delay was documented at the age of 3 years. The child attends special education classes at school and has abnormal behaviors with frequent temper tantrums and aggression. A brain MRI at the age of 4 years shows mildly foreshortened frontal lobes and very subtle simplification of the cortical gyral pattern. Brain MR images

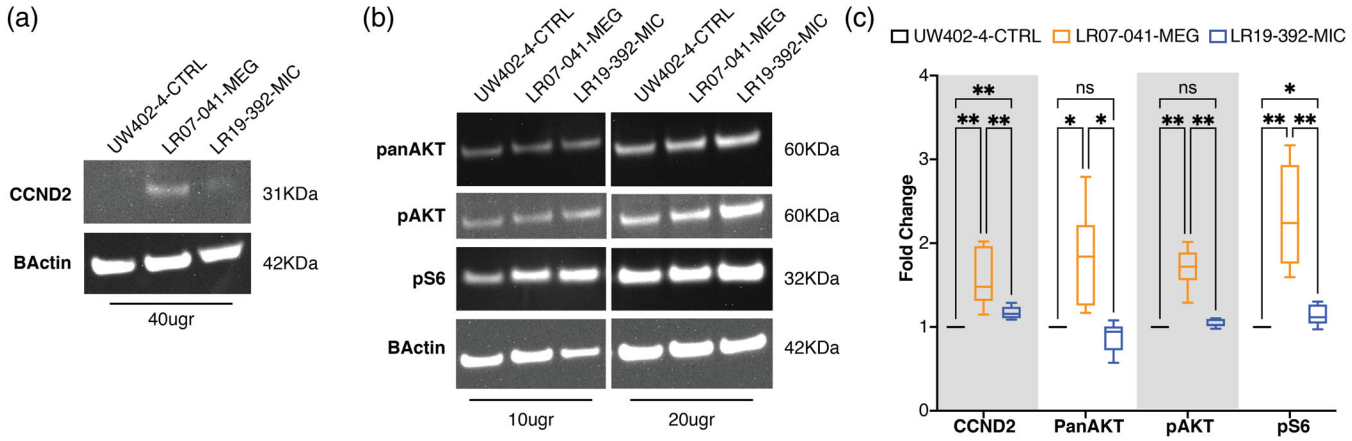

FIGURE 3 Western blot analysis of MIC- and MEG-associated CCND2 cell lines. Six independent experiments were performed using 10, 20, or 40 μg of protein extracts from fibroblasts cell lines obtained from a wild-type (UW402-4-CTRL), a *CCND2* MIC patient (LR19-392-MIC) and a *CCND2* MEG patient (LR07-041-MEG). (a) Representative blots for CCND2 and beta-actin for the three cell lines, with relative molecular weight shown on the left; due to low expression of CCND2 in fibroblasts, 40 μg of protein extracts was used. (b) Representative blots for PanAKT, pAKT, pS6, and beta-actin for the three cell lines. Two different protein extract concentrations were loaded (10 and 20 μg), the relative molecular weight of each detected protein is shown on the left. (c) Quantification of the analyzed proteins as average of the six independent experiments. The box plot represents the 5–95 centile interval, with the line in the box representing the median value, and the error bars indicating the minimum and maximum value. A one-way ANOVA (mixed effect analysis) was performed to identify significant differences among the cell lines. LR07-041-MEG presented increased expression of CCND2, panAKT, pAKT, and pS6 compared to control. LR19-392-MIC showed increased levels of CCND2 compared to control, but lower than LR07-041. While PanAKT and pAKT were not affected by the increase in CCND2, LR19-392-MIC presented increased levels of pS6 compared to control, albeit at lower levels than LR07-041-MEG. Ns, nonsignificant; **p*-value < 0.05; ***p*-value < 0.01. The full range of quantifications is listed in Supplementary Table 1, additional representative western blots are shown in Supplementary Figure 1

and clinical photographs are shown in Figure 2d–h. The younger sister, LR20-198a2, similarly presented with IUGR. Microcephaly was documented at the age of 12 months. She also had short stature from the 2nd year of life, with failure to thrive, feeding difficulties and speech delays. At the age of 4 years, she had several seizure-like episodes and an abnormal EEG pattern, but no antiepileptic treatments were initiated. A brain MRI performed at age 2 years and 5 months was normal. Brain MR images and clinical photographs are shown in Figure 2i–m. The mother of these two siblings, LR20-198 m, also had microcephaly (OFC 51 cm <1st centile, − 3.1 SD) and had short stature (height 150 cm, 2nd centile, −2 SD). She was also identified to have mild intellectual and learning disabilities. She attended special education classes at school and did not graduate. Her health history was otherwise unremarkable.

Exome sequencing performed on LR20-198a1 showed a heterozygous *CCND2* variant (NM_001759.4:c.544C>T, p.Q182X) which was not observed in gnomADv2.1.1 or in-house databases. This nonsense variant is predicted to be deleterious by in silico prediction programs including Combined Annotation Dependent Depletion (CADD) and Mutation Taster (Kircher et al., 2014; Schwarz et al., 2014). Through targeted sequencing, this variant was confirmed in the heterozygous state in both LR20-198a2 and LR20-198 m but was absent in three unaffected siblings. A chromosomal microarray on LR20-198a1 demonstrated an 85 kb intragenic microduplication affecting exons 20–25 of *PIK3C3*. This microduplication was present in LR20-198a2 and LR20-198 m but also in several unaffected relatives and was therefore considered to be benign.

Table 2 summarizes the clinical features and molecular features of the five individuals in this series. We investigated the potential pathogenicity of the three *CCND2* variants, as well as the *TNEM1* variant identified in individual LR19-002 using several in silico prediction programs. All *CCND2* variants were classified as disease causing and were not present in public databases such as dbSNP, 1000Genomes and gnomADv2.1.1 (Auton et al., 2015; Karczewski et al., 2020; Sherry et al., 2001). These results are summarized in Table 3. In gnomAD, coverage of the regions surrounding the three novel *CCND2* variants reported here was good (gnomADv2.1.1, over 240,000 reference alleles), and seven putative loss of function (pLoF) variants are listed in the gene. However, none of them overlap with our variants, six of these are classified as low confidence (variant annotation or quality dubious) pLoF calls, with the remaining pLoF variant, p.Glu272Ter, listed as pathogenic.

3.2 | Western blot analysis of CCND2 mutant fibroblasts

To identify differences in CCND2 expression levels and compare them to expression levels of proteins in the PI3K-AKT-MTOR pathway, including AKT, phosphorylated AKT (pAKT), and phosphorylated S6 (pS6), we performed western blot experiments using protein

extracts from control fibroblasts (UW402-4-CTRL), one *CCND2* MEG patient (LR07-041-MEG, p.T280N) and one *CCND2* MIC patient (LR19-392-MIC, p.G102VfsX17). Due to low expression of CCND2 in primary human fibroblasts, we confirmed the specificity of the CCND2 antibody band at 31KDa using a mouse cerebellar protein extract (Supplementary Figure 1A). When compared to the control human fibroblast cell line, the LR07-041-MEG line had significantly increased levels of CCND2 (average 1.6-fold change) as well as increased levels of panAKT (average 1.71-fold change), pAKT (1.64-fold change) and pS6 (2.41-fold change), as expected (Figure 3a–c, Supplementary Table 1, Supplementary Figure 1C). Interestingly, the LR19-392-MIC line also had significantly increased levels of CCND2 compared to controls (average 1.17-fold change). The increase in CCND2 correlated with a small increase in pS6 levels (average 1.16-fold change), but not of panAKT or pAKT (Figure 3a–c, Supplementary Table 1, Supplementary Figure 1C).

3.3 | High-content imaging of CCND2 mutant fibroblasts

To assess the morphological and functional differences between LR19-392-MIC and LR07-041-MEG cell lines, we performed immunostaining of key markers for proliferation (Ki-67) and MTOR hyperactivation (pS6) using high-content imaging performed with the CellInsight CX7 LZR (Thermofisher). We analyzed 33,218 cells in total for UW402-4-CTRL line; 36,104 cells for the LR19-392-MIC line; and 12,508 cells for the LR07-041-MEG line, as shown in Figure 4. We identified a significant increase in the percentage of pS6 positively staining cells in LR07-041-MEG, but not in LR19-392-MIC cells (Figure 4). The increase in pS6+ cells was accompanied by a significant increase in the percentage of double positive cells (pS6+/Ki-67 +) in LR07-041-MEG. In addition, the intensity (and thus the levels of expression) of both pS6 and Ki-67 were significantly higher in

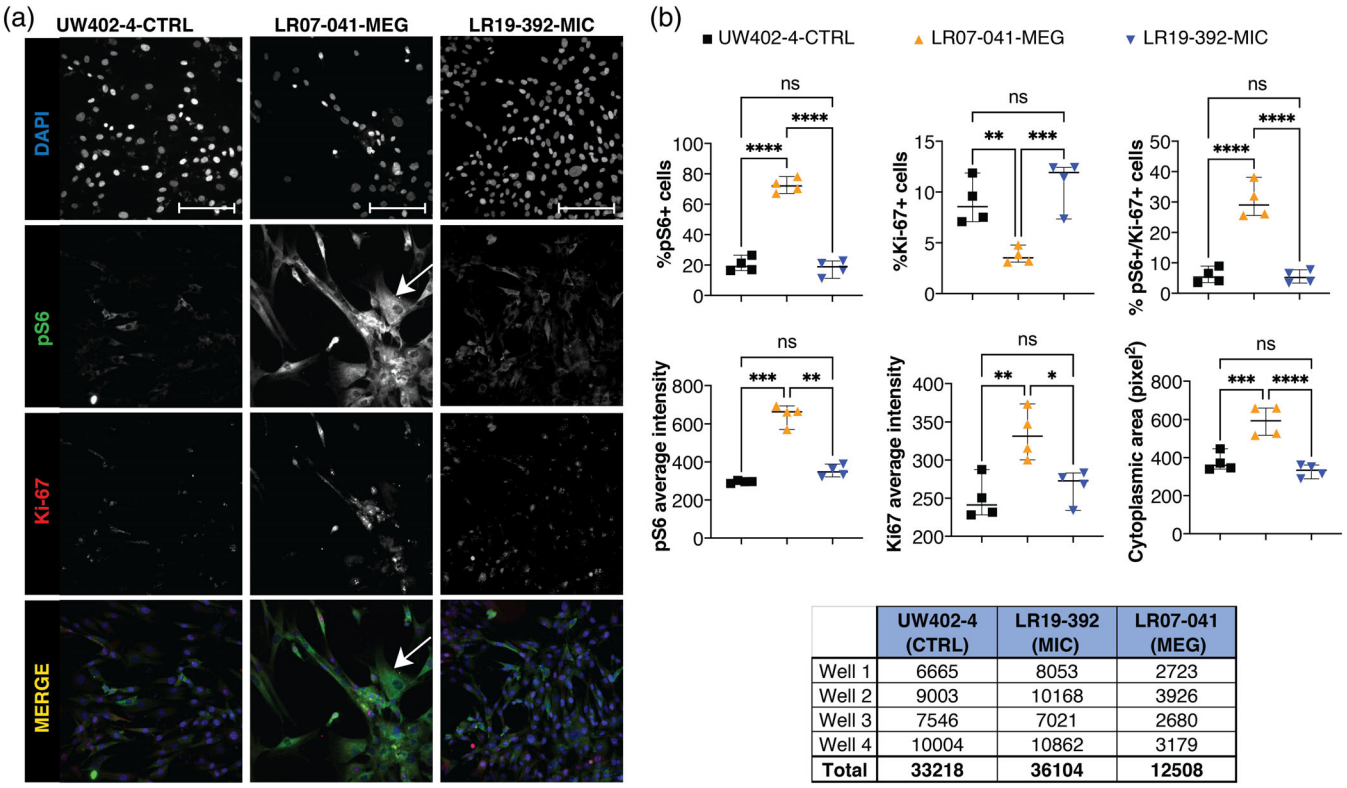

	UW402-4 (CTRL)	LR19-392 (MIC)	LR07-041 (MEG)
Well 1	6665	8053	2723
Well 2	9003	10168	3926
Well 3	7546	7021	2680
Well 4	10004	10862	3179
Total	**33218**	**36104**	**12508**

FIGURE 4 High-content imaging on fibroblast cell lines with *CCND2* MIC and MEG mutations. Fibroblast cell lines from one control (UW402-4-CTRL), one *CCND2* MIC (LR07-041-MIC), and one *CCND2* MEG (LR19-392-MEG) patients were plated in an optical 96 well plate (4 replicates each) and immunostained for proliferation marker Ki-67 and MTOR hyperactivation marker pS6; nuclei were counterstained with DAPI. Image acquisition and quantification was performed using the high-content imaging platform CellInsight CX7 LZR and the HCS studio software. (a) Single channel and overlay immunofluorescence images of one representative field per well per cell line are shown (20× magnification, scale bar 100 μm). For LR07-041-MEG, a hypertrophic fibroblast is indicated by the white arrow. (b) Quantification of the cells analyzed (4 wells per cell line, 15 fields per well) using the HCS software. Each value represents the average per well per cell line. In each graph and for each cell line, the thick bar represents the median, and the error bars represent the 95% confidence interval. One-way ANOVA analysis with multiple comparison was performed using GraphPad Prism software. Ns, nonsignificant; **p*-value < 0.05; ***p*-value < 0.01; ****p*-value < 0.0001; *****p*-value < 0.00001. LR07-041-MEG shows increase in the percentage of pS6+ and ps6/Ki-67+ cells, with a reduction of Ki-67+ cells. The same line also presented increased intensity (level of expression) for pS6 and Ki-67, as well as increased cytoplasmic area. LR19-392-MIC did not show any significant difference when compared to the control. The table below panel B lists the number of cells analyzed per well per cell line, and the relative total number of cells per cell line

LR07-041-MEG but not in LR19-392-MIC (Figure 4). More interestingly, cytoplasmic area assessments via pS6 staining revealed marked hypertrophy in LR07-041-MEG cells (average area 590.93 pixel^2) compared to controls and to the LR19-392-MIC line (376.18 pixel^2 in UW402-4, and 329.13 pixel^2 in LR19-392) (Figure 4b).

3.4 | Literature review of reciprocal brain growth phenotypes

In light of our findings, we reviewed the literature of inverse brain phenotypes similar to *CCND2* associated with reciprocal functional effects of genes. A brief overview of these genes, namely *AKT3*, *PTEN*, *NSD1*, *MYCN*, *EZH2*, and *MIR17HG*, is provided below, and their associated phenotypes are summarized in Table 1.

AKT3

AKT3, also known as protein kinase B (PKB), is located on chromosome 1q43-44 and encodes a serine/threonine protein kinase expressed primarily in the brain. *AKT3* is one of three closely related AKT isoforms and is the primary downstream effector of PI3K signaling. PI3K-AKT-mTOR signaling regulates many important cell functions, including protein synthesis, cell proliferation and survival (Diez et al., 2012; Ersahin et al., 2015; Ling Wang et al., 2017). *AKT3* exerts its regulatory effects through serine and/or threonine phosphorylation of various downstream substrates, one of which is linked to influencing cyclin-D2 levels by S9 residue phosphorylation and subsequent inactivation of glycogen synthase kinase-3 β (GSK-3β) (P. Cohen & Frame, 2001; Hermida et al., 2017; Miao et al., 2016; Ouimet et al., 2019). GSK-3β is a negative regulator of cyclin D1 and D2 by ubiquitin dependent degradation. The AKT family of proteins are implicated in a wide range of human diseases including cancer, diabetes, cardiovascular and neurological disease (Alcantara et al., 2017; Chung et al., 2014; Conti et al., 2015; Dobyns & Mirzaa, 2019; Gai et al., 2015; Grabinski et al., 2011; Hers et al., 2011; Lee et al., 2012; Lopes et al., 2019; Mure et al., 2010; Poduri et al., 2012; Riviere et al., 2012; D. Wang et al., 2013; Yang et al., 2005). Gain-of-function variants in *AKT3* lead to inactivation of GSK-3β which in turn results in stabilization and increased levels of cyclin D2 which has been proposed as the unifying mechanism for MPPH syndrome (G. Mirzaa et al., 2014). Data from humans and animal models suggest a gene dosage effect of *AKT3* resulting in inverse phenotypes. *Akt3* knockout mice display microcephaly suggesting that it plays a critical role in determining brain size (Easton et al., 2005; Yang et al., 2005). Mosaic and constitutional gain-of-function variants of *AKT3* are associated with MPPH syndrome (Lee et al., 2012; Lopes et al., 2019; Poduri et al., 2012; Riviere et al., 2012), with more than 20 patients reported to date with molecularly confirmed *AKT3* related megalencephaly (Alcantara et al., 2017; Harada et al., 2015; Jamuar et al., 2014; Nakamura et al., 2014; Negishi et al., 2017; Nellist et al., 2015; Riviere et al., 2012). A subset of affected individuals is mosaic for the common p.E17K mutation causing hemimegalencephaly (Jansen et al., 2015; Lee et al., 2012; Poduri et al., 2012; Riviere et al., 2012). Duplications of 1q43-q44 encompassing *AKT3* have also been reported to cause macrocephaly (Chung et al., 2014; Hemming et al., 2016; Luo et al., 2018; D. Wang et al., 2013). Heterozygous deletions of 1q43-q44 involving *AKT3*, on the other hand, result in postnatal microcephaly and agenesis of the corpus callosum (Gai et al., 2015; Hemming et al., 2016; Lopes et al., 2019).

PTEN

Loss-of-function variants in *PTEN*, which encodes for phosphatase and tensin homolog and tumor suppressor, cause a spectrum of clinical megalencephaly disorders including Cowden syndrome (CS), Bannayan–Riley–Ruvalcaba syndrome (BRRS), and autism spectrum disorder with macrocephaly (Gorlin et al., 1992; Herman et al., 2007; Marsh et al., 1998; Orrico et al., 2009; Varga et al., 2009; Zhou et al., 2003). These syndromes share characteristic features including overgrowth and predisposition to various tumors. PTEN suppresses phosphoinositide 3-kinase (PI3K) signaling that activates cell growth and tumorigenesis. Mice deficient in nuclear PTEN have microcephaly persisting into adulthood (Igarashi et al., 2018; Kwon et al., 2001; Kwon et al., 2003; Kwon et al., 2006). Further, deletions of the 10q23 locus encompassing *PTEN* are associated with macrocephaly, hypotonia, and increased predisposition to various malignancies, including juvenile polyposis syndrome (Babovic et al., 2010). In contrast, microduplications of this locus have recently been identified in association with autosomal dominant primary microcephaly and decreased mTOR signaling (Oliveira et al., 2019).

NSD1

NSD1, located on chromosome 5q35.3, encodes for nuclear receptor binding (SET) domain histone methyltransferase that methylates lysine 36 of histone 3 (H3K36) (Graham et al., 2016). This histone modifier regulates the activity of several genes involved in growth and development. Haploinsufficiency of *NSD1* causes Sotos syndrome characterized by brain and somatic overgrowth, distinctive facial features (broad, prominent forehead, dolichocephaly, spares frontotemporal hair, long chin, long narrow face, malar flushing, down-slanting palpebral fissures), and intellectual disability (Kurotaki et al., 2002). Other major features include behavioral problems, advanced bone age, cardiac defects, cranial abnormalities, skeletal abnormalities including joint hyperlaxity and scoliosis, renal defects, and seizures. A minority of affected individuals (<15%) have other features such as hemihypertrophy, conductive hearing loss, pectus excavatum, and strabismus. Loss-of-function variants and deletions of 5q35 encompassing *NSD1* have been identified in approximately 90% of individuals with Sotos syndrome (Tatton-Brown et al., 2005). Conversely, *NSD1* duplications result in growth retardation and microcephaly (Dikow et al., 2013; Franco et al., 2010; Lucio-Eterovic

et al., 2010; Sachwitz et al., 2017; Sellars et al., 2011; Tracy et al., 2011; J. C. Wang et al., 2007; Zhang et al., 2011). Further, murine models carrying a heterozygous 1.5-Mb deletion of 36 genes including *Nsd1* syntenic with 5q35.2-q35.3 in humans had a phenotype characterized by small gestational age and decreased postnatal growth (Migdalska et al., 2012).

MYCN

MYCN, located on chromosome 2p24.3, encodes for N-Myc protein, a transcription factor critical to normal embryonic development and postnatal brain size. The *MYCN* gene is part of the Myc family of proto-oncogenes critical for regulating cell differentiation and growth (Henriksson & Luscher, 1996). Much of the function of the Myc family of proteins is through downstream activation and repression of specific target genes (Eisenman, 2001). These targets include the cyclin-dependent kinase *CDK4*, a Cdc25A phosphatase that activates CDKs, cyclin D2 and the E2F family (Bouchard et al., 1999; Galaktionov et al., 1996; Leone et al., 2001). Amplification of *MYCN* is associated with various cancers including prostate cancer (Dardenne et al., 2016), retinoblastoma (Rushlow et al., 2013), and aggressive forms of neuroblastoma (Higashi et al., 2019; Otto et al., 2009; Tavana et al., 2016; Xue et al., 2016). The carcinogenic potential of N-Myc is likely due to its ability to drive cells into the cell cycle. A mouse model showed that *N-myc* plays a vital role in neurogenesis and that homozygous absence of *N-myc* results in a twofold decrease in brain mass that disproportionately affects the cerebellum and cerebral cortex (Knoepfler et al., 2002). This same study suggested that the decrease in brain size is due to downregulation of a subset of cyclin-dependent kinase inhibitors and disruption of *CCND2* expression. Germline loss of function variants of *MYCN* cause Feingold syndrome type 1 characterized by microcephaly, limb abnormalities, atresia of the gastrointestinal tract, learning disabilities, and dysmorphic facial features. Deletions involving the *MYCN* locus have also been reported as a cause of Feingold Syndrome (Chen et al., 2012; Mercedes Bloch et al., 2014). Although there is variable expressivity, there are no significant genotype–phenotype differences between individuals with Feingold Syndrome (Marcelis et al., 2008). Further, an *MYCN* gain-of-function variant resulting in increased *CCND1* and *CCND2* expression has recently been reported to cause a novel megalencephaly syndrome that is similar but distinct from MPPH syndrome (Kato et al., 2018).

EZH2

Enhancer of Zeste, Drosophila, homolog 2 (*EZH2*, MIM: 601573) encodes for part of the polycomb repressive complex 2 (PRC2), which mediates suppression of transcription via chromatin condensation through methylation of histone H3 (lysine 27) (Cao et al., 2002). Variants in this gene are the primary cause of Weaver Syndrome (WS), characterized by overgrowth, facial gestalt, accelerated bone maturation and variable degree of intellectual disability (A. S. Cohen et al., 2016; Gibson et al., 2012; Lui et al., 2018; Tatton-Brown et al., 2011; Tatton-Brown et al., 2013). Studies in humans and mice have demonstrated that *EZH2* variants associated with WS are mainly due to reduced methyltransferase activity, and thus are classified as loss of function (A. S. Cohen & Gibson, 2016; Lui et al., 2018). Recently, an elegant study utilized DNA methylation signature to classify missense variants in *EZH2* as pathogenic or benign, and provided insights into gain of function mutations and mosaicism (Choufani et al., 2020). Notably, gain of methylation at the same CpG sites associated with WS, lead to transcriptional changes during development resulting in growth restriction in one patient (Choufani et al., 2020). This evidence adds *EZH2* to the growing list of genes with epigenetic functions that can affect cell growth through changes in their transcriptional profiles, similarly to *NSD1* (Aref-Eshghi et al., 2018; Butcher et al., 2017; Choufani et al., 2015).

MIR17HG and 13q31.3

MIR17HG gene encodes the miR-17 ~92 polycistronic microRNA (miRNA) cluster, a family of six highly conserved miRNA (Han et al., 2015). Focal amplifications of this region are present in many types of cancer, with ectopic expression of this locus associated with acceleration of tumor formation in murine models (Han et al., 2015). Microdeletions of chromosome 13q that include the *MIR17HG* gene are associated with Feingold 2 syndrome, with features of microcephaly, brachymesophalangy, toe syndactyly, short stature, cardiac anomalies, growth hormone deficiency, aortic dilation, phalangeal joint contractures, memory, and sleep problems (de Pontual et al., 2011; Muriello et al., 2019). Recently, a de novo 13q31.3 microduplication encompassing *MIR17HG* was described in a female patient with developmental delay, skeletal and digital abnormalities, and tall stature and macrocephaly (Siavriene et al., 2020).

4 | DISCUSSION

The *CCND2* gene, located on 12p13.32, encodes the protein Cyclin D2 and is a member of the highly conserved cyclin family, regulating the G1 to S phase transition in the cell cycle (Z. Wang et al., 2008; Xiong et al., 1992). Gain-of-function (GoF) variants in *CCND2*, *AKT3* and *PIK3R2* have been implicated in MPPH syndrome. Megalencephaly-associated variants in components of the PI3K-AKT-MTOR pathway, including variants within the terminal exon of *CCND2*, share the same functional endpoint, namely inhibition of proteasomal degradation of cyclin D2 (G. Mirzaa et al., 2014). This influences many important cell functions including cell growth and division, protein synthesis and cell survival. Although not directly in the PI3K-AKT-MTOR pathway, *MCYN* indirectly participates through upstream modulation of *CCND1* and *CCND2* expression (Kato et al., 2018). Further, copy number

abnormalities, namely 12p13.32 deletions encompassing *CCND2*, have been identified in individuals with microcephaly and a wide spectrum of clinical features including intellectual disability, short stature, developmental delays, and dysmorphic features. However, the highly variable presentation and high gene content of this microdeletion syndrome provided limited evidence regarding the role of *CCND2*. (Firth et al., 2009). This is the first series reporting on individuals with heterozygous frameshift and stop gain *CCND2* variants resulting in microcephaly, to our knowledge. All affected individuals demonstrated poor growth, in association with neurodevelopmental issues, among other features.

CCND2 is highly expressed in pluripotent human embryonic stem cells (Becker et al., 2010), and is postnatally expressed at high levels in the human brain, adrenal gland, heart, and colon (Fagerberg et al., 2014). CCND2 is a regulatory subunit of the Cyclin D2-CDK4 complex, which phosphorylates and inhibits members of the retinoblastoma (RB) family of proteins including RB1. Phosphorylation of RB1 allows dissociation of the transcription factor E2F from the RB/E2F complex and the subsequent transcription of E2F target genes responsible for progression through the G1 phase of the cell cycle. Cyclin D2 is also a substrate for SMAD3, phosphorylating SMAD3 in a cell-cycle-dependent manner and repressing its transcriptional activity. Cyclin D2 has been found to be highly expressed in the adult mouse brain suggesting that cyclin D2 carries out a unique role in terminally differentiated neurons (Ross et al., 1996). Murine knockout models of *Ccnd2* lack adult neurogenesis almost entirely (Kondratiuk et al., 2015). A deficit in parvalbumin positive (PV+) GABAergic interneurons in *Ccnd2* null mice have been observed in both the cortex and the hippocampus leading to a decrease in cortical inhibition (Glickstein et al., 2007). Evidence of this cortical inhibition was demonstrated on EEGs of awake *cD2*-null mice showing increased frequency and amplitude of paroxysmal cortical discharges (Glickstein et al., 2007). Furthermore, gene dose dependent differences in brain cortical surface area have been observed in mouse models with heterozygous knockouts of *Ccnd2* resulting in an intermediate phenotype (Glickstein et al., 2007). *Ccnd2* null mice had microcephaly with either a relatively preserved or mildly decreased body size with catch up growth and an increase in seizure activity as they age (M. Elizabeth Ross, personal communication, April 25, 2019).

Our series of five individuals with microcephaly and three novel variants in *CCND2* expands the genotype–phenotype spectrum for this gene. Our functional analysis revealed increased levels of CCND2 and other key PI3K-AKT-MTOR markers in *CCND2* mutant fibroblasts derived from a child with MPPH, confirming previous findings by our group (G. Mirzaa et al., 2014). Immunostaining also revealed marked increase in Ki-67 expression, suggesting that increased proliferation is a mechanism for CCND2-related MEG, as demonstrated by our prior work on *CCND2* (G. Mirzaa et al., 2014). Our data further show that an increase in cell size, or cellular hypertrophy, is likely another feature of *CCND2*-related MEG, as demonstrated by the significant enlargement of cytoplasmic area, and similar to the MTOR-dependent hypertrophy identified in *Pten*-deficient mice (Kwon et al., 2001; Kwon et al., 2003). Despite the increase in pS6+ and Ki-67+/pS6+ cells, the LR07-041 MEG cell line showed a reduced overall percentage of Ki67+ cells, due to the overall lower number of cells present in the wells, as cells occupy a larger volume (12,508 cells for LR07-041 MEG vs. 33,218 cells in the control). Similar assays on the *CCND2*-associated microcephaly cell line revealed lower levels of *CCND2* compared to the MEG cell line. However, levels were surprisingly slightly higher than the control line. We were able to detect the CCND2 protein in the LR19-392 MIC cell line despite the premature stop codon as the antibody recognized an epitope in the N-terminus, suggesting expression of a truncated isoform of the protein in this patient. We therefore hypothesize that the increase in CCND2 levels in the MIC cell line could be due to accumulation of unphosphorylated degradation-resistant cyclin D2, similarly to what demonstrated for *CCND2* -related MPPH (G. Mirzaa et al., 2014), albeit with distinct functional consequences in the developing brain. We also hypothesize that this mild increase in protein level is likely insufficient to cause hyperplasia or hypertrophy, as the LR19-392-MIC cells were not significantly different in size or number from controls. We previously identified a nonsense variant in the terminal exon of *CCND2* in association with MPPH (p.Lys270X) (G. Mirzaa et al., 2014), thus we postulate that variants in distinct regions of the gene (proximal vs. distal) are directly relevant to the functional consequences and associated phenotypes of *CCND2*-related disorders.

We considered whether the *TENM1* hemizygous variant in individual LR19-002 could contribute to the phenotype. However, we believe this is less likely as *TENM1* is not known to be associated with microcephaly, to date. Notably, individual LR19-392 in our study underwent only targeted multigene sequencing. Therefore, we cannot rule out the possibility that this individual may carry other variants that might contribute to the phenotype. Finally, additional functional studies in more relevant models, such as human induced pluripotent stem cell-derived neurons, are needed to confirm some of the above hypotheses regarding the role of *CCND2* in regulating brain size and the exact molecular mechanisms of *CCND2*-related microcephaly in humans.

In summary, our study expands the phenotypic spectrum of *CCND2*-related disorders in humans and suggests that distinct classes of genetic variants within different domains of the gene—namely proximal versus distal variants—have different functional consequences on the developing human brain and are likely associated with reciprocal effects on early brain growth—with more proximal and potentially loss of function variants causing protein truncation associated with microcephaly, and distal variants abolishing phosphorylation-dependent ubiquitination sites resulting in megalencephaly. This study further highlights the diversity of the molecular mechanisms that cause brain growth syndromes and the paradigm of reciprocal genetic variants leading to inverse brain phenotypes.

ACKNOWLEDGMENTS

We thank the patients, their families and care providers for their contribution to this study. We thank Dr. M. Elizabeth Ross, Professor of Neurology and Neuroscience, and the Ross Laboratory at Weill Cornell Medicine for their expert input regarding the function and role of CCND2 in brain development. We also thank Dr. Daniel Doherty,

Professor of Pediatrics and Developmental Medicine, for providing the control fibroblast cell line used in this manuscript (UW402-4). Research reported in this publication was supported by Jordan's Guardian Angels and the Sunderland Foundation (to Filomena Pirozzi and Ghayda M. Mirzaa), and the Brotman-Baty Institute (to Ghayda M. Mirzaa); Nataliya Di Donato work was supported by German Research Foundation (DI 2170/3-1). The content is solely the responsibility of the authors and does not necessarily represent the official views of the National Institutes of Health. The funding sources had no role in the design and conduct of the study, collection, management, analysis and interpretation of the data, preparation, review or approval of the manuscript, or decision to submit the manuscript for publication.

CONFLICT OF INTEREST

The authors declare no conflict of interest.

AUTHOR CONTRIBUTIONS

Filomena Pirozzi and Ghayda M. Mirzaa conceptualized and designed the study, and analyzed all the clinical, molecular and functional data. Filomena Pirozzi performed western blot analysis, high-content imaging analysis, analyzed clinical and molecular data, and drafted the manuscript; Nicole Horsley performed cell culture, protein extraction, western blot experiments, and contributed to drafting of the manuscript; Benson Lee, Deepika D. Burkardt, William B. Dobyns, John M. Graham Jr., Maria L. Dentici, Claudia Cesario, Jens Schallner, Nataliya Di Donato, Pedro A. Sanchez-Lara, and Ghayda M. Mirzaa contributed to the acquisition of the data, drafting, and critical revision of the manuscript and associated data.

DATA AVAILABILITY STATEMENT

The authors confirm that the data supporting the findings of this study are available within the article and its supplementary material. The raw data that support the findings of this study, including the genetic analyses and the high content imaging results are available on request to the corresponding authors.

ORCID

Filomena Pirozzi https://orcid.org/0000-0002-7603-662X
Deepika D. Burkardt https://orcid.org/0000-0002-1743-7503
William B. Dobyns https://orcid.org/0000-0002-7681-2844
John M. Graham Jr https://orcid.org/0000-0003-4297-1078
Maria L. Dentici https://orcid.org/0000-0002-9505-5906
Nataliya Di Donato https://orcid.org/0000-0001-9439-4677
Pedro A. Sanchez-Lara https://orcid.org/0000-0003-1181-7828
Ghayda M. Mirzaa https://orcid.org/0000-0003-2648-7657

REFERENCES

Alcantara, D., Timms, A. E., Gripp, K., Baker, L., Park, K., Collins, S., Cheng, C., Stewart, F., Mehta, S. G., Saggar, A., Sztriha, L., Zombor, M., Caluseriu, O., Mesterman, R., Van Allen, M. I., Jacquinet, A., Ygberg, S., Bernstein, J. A., Wenger, A. M., … Mirzaa, G. M. (2017). Mutations of AKT3 are associated with a wide spectrum of developmental disorders including extreme megalencephaly. *Brain*, *140*(10), 2610–2622. https://doi.org/10.1093/brain/awx203

Alkelai, A., Olender, T., Haffner-Krausz, R., Tsoory, M. M., Boyko, V., Tatarskyy, P., Gross-Isseroff, R., Milgrom, R., Shushan, S., Blau, I., Cohn, E., Beeri, R., Levy-Lahad, E., Pras, E., & Lancet, D. (2016). A role for TENM1 mutations in congenital general anosmia. *Clinical Genetics*, *90*(3), 211–219. https://doi.org/10.1111/cge.12782

Aref-Eshghi, E., Rodenhiser, D. I., Schenkel, L. C., Lin, H., Skinner, C., Ainsworth, P., Paré, G., Hood, R. L., Bulman, D. E., Kernohan, K. D., Care4Rare Canada Consortium, Boycott, K. M., Campeau, P. M., Schwartz, C., & Sadikovic, B. (2018). Genomic DNA methylation signatures enable concurrent diagnosis and clinical genetic variant classification in neurodevelopmental syndromes. *American Journal of Human Genetics*, *102*(1), 156–174. https://doi.org/10.1016/j.ajhg.2017.12.008

Auton, A., Brooks, L. D., Durbin, R. M., Garrison, E. P., Kang, H. M., Korbel, J. O., Marchini, J. L., McCarthy, S., McVean, G. A., Abecasis, G. R., & Genomes Project, C. (2015). A global reference for human genetic variation. *Nature*, *526*(7571), 68–74. https://doi.org/10.1038/nature15393

Babovic, N., Simmons, P. S., Moir, C., Thorland, E. C., Scheithauer, B., Gliem, T. J., & Babovic-Vuksanovic, D. (2010). Mucinous cystadenoma of ovary in a patient with juvenile polyposis due to 10q23 microdeletion: Expansion of phenotype. *American Journal of Medical Genetics. Part A*, *152A*(10), 2623–2627. https://doi.org/10.1002/ajmg.a.33637

Becker, K. A., Ghule, P. N., Lian, J. B., Stein, J. L., van Wijnen, A. J., & Stein, G. S. (2010). Cyclin D2 and the CDK substrate p220(NPAT) are required for self-renewal of human embryonic stem cells. *Journal of Cellular Physiology*, *222*(2), 456–464. https://doi.org/10.1002/jcp.21967

Bouchard, C., Thieke, K., Maier, A., Saffrich, R., Hanley-Hyde, J., Ansorge, W., Reed, S., Sicinski, P., Bartek, J., & Eilers, M. (1999). Direct induction of cyclin D2 by Myc contributes to cell cycle progression and sequestration of p27. *The EMBO Journal*, *18*(19), 5321–5333. https://doi.org/10.1093/emboj/18.19.5321

Burkardt, D. D., Tatton-Brown, K., Dobyns, W., & Graham, J. M., Jr. (2019). Approach to overgrowth syndromes in the genome era. *American Journal of Medical Genetics. Part C, Seminars in Medical Genetics*, *181*(4), 483–490. https://doi.org/10.1002/ajmg.c.31757

Butcher, D. T., Cytrynbaum, C., Turinsky, A. L., Siu, M. T., Inbar-Feigenberg, M., Mendoza-Londono, R., Chitayat, D., Walker, S., Machado, J., Caluseriu, O., Dupuis, L., Grafodatskaya, D., Reardon, W., Gilbert-Dussardier, B., Verloes, A., Bilan, F., Milunsky, J. M., Basran, R., Papsin, B., … Weksberg, R. (2017). CHARGE and kabuki syndromes: Gene-specific DNA methylation signatures identify epigenetic mechanisms linking these clinically overlapping conditions. *American Journal of Human Genetics*, *100*(5), 773–788. https://doi.org/10.1016/j.ajhg.2017.04.004

Cao, R., Wang, L., Wang, H., Xia, L., Erdjument-Bromage, H., Tempst, P., Jones, R. S., & Zhang, Y. (2002). Role of histone H3 lysine 27 methylation in Polycomb-group silencing. *Science*, *298*(5595), 1039–1043. https://doi.org/10.1126/science.1076997

Cappuccio, G., Ugga, L., Parrini, E., D'Amico, A., & Brunetti-Pierri, N. (2019). Severe presentation and complex brain malformations in an individual carrying a CCND2 variant. *Molecular Genetics & Genomic Medicine*, *7*(6), e708. https://doi.org/10.1002/mgg3.708

Chen, C. P., Lin, S. P., Chern, S. R., Wu, P. S., Chang, S. D., Ng, S. H., Liu, Y. P., Su, J. W., & Wang, W. (2012). A de novo 4.4-Mb microdeletion in 2p24.3→p24.2 in a girl with bilateral hearing impairment, microcephaly, digit abnormalities and Feingold syndrome. *European Journal of Medical Genetics*, *55*(11), 666–669. https://doi.org/10.1016/j.ejmg.2012.07.003

Choufani, S., Cytrynbaum, C., Chung, B. H., Turinsky, A. L., Grafodatskaya, D., Chen, Y. A., Cohen, A. S., Dupuis, L., Butcher, D. T., Siu, M. T., Luk, H. M., Lo, I. F., Lam, S. T., Caluseriu, O., Stavropoulos, D. J., Reardon, W., Mendoza-Londono, R., Brudno, M., Gibson, W. T., … Weksberg, R. (2015). NSD1 mutations generate a genome-wide DNA methylation signature. *Nature Communications*, *6*, 10207. https://doi.org/10.1038/ncomms10207

Choufani, S., Gibson, W. T., Turinsky, A. L., Chung, B. H. Y., Wang, T., Garg, K., Vitriolo, A., Cohen, A. S. A., Cyrus, S., Goodman, S., Chater-Diehl, E., Brzezinski, J., Brudno, M., Ming, L. H., White, S. M., Lynch, S. A., Clericuzio, C., Temple, I. K., Flinter, F., … Weksberg, R. (2020). DNA methylation signature for EZH2 functionally classifies sequence variants in three PRC2 complex genes. *American Journal of Human Genetics*, *106*(5), 596–610. https://doi.org/10.1016/j.ajhg.2020.03.008

Chung, B. K., Eydoux, P., Van Karnebeek, C. D., & Gibson, W. T. (2014). Duplication of AKT3 is associated with macrocephaly and speech delay. *American Journal of Medical Genetics. Part A*, *164A*(7), 1868–1869. https://doi.org/10.1002/ajmg.a.36521

Cohen, A. S., & Gibson, W. T. (2016). EED-associated overgrowth in a second male patient. *Journal of Human Genetics*, *61*(9), 831–834. https://doi.org/10.1038/jhg.2016.51

Cohen, A. S., Yap, D. B., Lewis, M. E., Chijiwa, C., Ramos-Arroyo, M. A., Tkachenko, N., Milano, V., Fradin, M., McKinnon, M. L., Townsend, K. N., Xu, J., Van Allen, M. I., Ross, C. J. D., Dobyns, W. B., Weaver, D. D., & Gibson, W. T. (2016). Weaver syndrome-associated EZH2 protein variants show impaired histone methyltransferase function in vitro. *Human Mutation*, *37*(3), 301–307. https://doi.org/10.1002/humu.22946

Cohen, P., & Frame, S. (2001). The renaissance of GSK3. *Nature Reviews. Molecular Cell Biology*, *2*(10), 769–776. https://doi.org/10.1038/35096075

Conti, V., Pantaleo, M., Barba, C., Baroni, G., Mei, D., Buccoliero, A. M., Giglio, S., Giordano, F., Baek, S. T., Gleeson, J. G., & Guerrini, R. (2015). Focal dysplasia of the cerebral cortex and infantile spasms associated with somatic 1q21.1-q44 duplication including the AKT3 gene. *Clinical Genetics*, *88*(3), 241–247. https://doi.org/10.1111/cge.12476

Dardenne, E., Beltran, H., Benelli, M., Gayvert, K., Berger, A., Puca, L., Cyrta, J., Sboner, A., Noorzad, Z., MacDonald, T., Cheung, C., Yuen, K. S., Gao, D., Chen, Y., Eilers, M., Mosquera, J. M., Robinson, B. D., Elemento, O., Rubin, M. A., … Rickman, D. S. (2016). N-Myc induces an EZH2-mediated transcriptional program driving neuroendocrine prostate cancer. *Cancer Cell*, *30*(4), 563–577. https://doi.org/10.1016/j.ccell.2016.09.005

de Pontual, L., Yao, E., Callier, P., Faivre, L., Drouin, V., Cariou, S., Van Haeringen, A., Geneviève, D., Goldenberg, A., Oufadem, M., Manouvrier, S., Munnich, A., Vidigal, J. A., Vekemans, M., Lyonnet, S., Henrion-Caude, A., Ventura, A., & Amiel, J. (2011). Germline deletion of the miR-17 approximately 92 cluster causes skeletal and growth defects in humans. *Nature Genetics*, *43*(10), 1026–1030. https://doi.org/10.1038/ng.915

Diez, H., Garrido, J. J., & Wandosell, F. (2012). Specific roles of Akt iso forms in apoptosis and axon growth regulation in neurons. *PLoS One*, *7*(4), e32715. https://doi.org/10.1371/journal.pone.0032715

Dikow, N., Maas, B., Gaspar, H., Kreiss-Nachtsheim, M., Engels, H., Kuechler, A., Garbes, L., Netzer, C., Neuhann, T. M., Koehler, U., Casteels, K., Devriendt, K., Janssen, J. W. G., Jauch, A., Hinderhofer, K., & Moog, U. (2013). The phenotypic spectrum of duplication 5q35.2-q35.3 encompassing NSD1: Is it really a reversed Sotos syndrome? *American Journal of Medical Genetics. Part A*, *161A*(9), 2158–2166. https://doi.org/10.1002/ajmg.a.36046

Dobyns, W. B., & Mirzaa, G. M. (2019). Megalencephaly syndromes associated with mutations of core components of the PI3K-AKT-MTOR pathway: PIK3CA, PIK3R2, AKT3, and MTOR. *American Journal of Medical Genetics. Part C, Seminars in Medical Genetics*, *181*, 582–590. https://doi.org/10.1002/ajmg.c.31736

Easton, R. M., Cho, H., Roovers, K., Shineman, D. W., Mizrahi, M., Forman, M. S., Lee, V. M. Y., Szabolcs, M., De Jong, R., Oltersdorf, T., Ludwig, T., Efstratiadis, A., & Birnbaum, M. J. (2005). Role for Akt3/protein kinase Bgamma in attainment of normal brain size. *Molecular and Cellular Biology*, *25*(5), 1869–1878. https://doi.org/10.1128/MCB.25.5.1869-1878.2005

Eisenman, R. N. (2001). Deconstructing myc. *Genes & Development*, *15*(16), 2023–2030. https://doi.org/10.1101/gad928101

Ersahin, T., Tuncbag, N., & Cetin-Atalay, R. (2015). The PI3K/AKT/mTOR interactive pathway. *Molecular BioSystems*, *11*(7), 1946–1954. https://doi.org/10.1039/c5mb00101c

Fagerberg, L., Hallstrom, B. M., Oksvold, P., Kampf, C., Djureinovic, D., Odeberg, J., Habuka, M., Tahmasebpoor, S., Danielsson, A., Edlund, K., Asplund, A., Sjöstedt, E., Lundberg, E., Szigyarto, C. A., Skogs, M., Takanen, J. O., Berling, H., Tegel, H., Mulder, J., … Uhlén, M. (2014). Analysis of the human tissue-specific expression by genome-wide integration of transcriptomics and antibody-based proteomics. *Molecular & Cellular Proteomics*, *13*(2), 397–406. https://doi.org/10.1074/mcp.M113.035600

Firth, H. V., Richards, S. M., Bevan, A. P., Clayton, S., Corpas, M., Rajan, D., van Vooren, S., Moreau, Y., Pettett, R. M., & Carter, N. P. (2009). *DECIPHER: Database of Chromosomal Imbalance and Phenotype in Humans using Ensembl Resources*. https://doi.org/10/1016/j.ajhg.2009.03.010

Franco, L. M., de Ravel, T., Graham, B. H., Frenkel, S. M., Van Driessche, J., Stankiewicz, P., Lupski, J. R., Vermeesch, J. R., & Cheung, S. W. (2010). A syndrome of short stature, microcephaly and speech delay is associated with duplications reciprocal to the common Sotos syndrome deletion. *European Journal of Human Genetics*, *18*(2), 258–261. https://doi.org/10.1038/ejhg.2009.164

Gai, D., Haan, E., Scholar, M., Nicholl, J., & Yu, S. (2015). Phenotypes of AKT3 deletion: A case report and literature review. *American Journal of Medical Genetics. Part A*, *167A*(1), 174–179. https://doi.org/10.1002/ajmg.a.36710

Galaktionov, K., Chen, X., & Beach, D. (1996). Cdc25 cell-cycle phosphatase as a target of c-myc. *Nature*, *382*(6591), 511–517. https://doi.org/10.1038/382511a0

Garthe, A., Huang, Z., Kaczmarek, L., Filipkowski, R. K., & Kempermann, G. (2014). Not all water mazes are created equal: Cyclin D2 knockout mice with constitutively suppressed adult hippocampal neurogenesis do show specific spatial learning deficits. *Genes, Brain, and Behavior*, *13*(4), 357–364. https://doi.org/10.1111/gbb.12130

Gibson, W. T., Hood, R. L., Zhan, S. H., Bulman, D. E., Fejes, A. P., Moore, R., Mungall, A. J., Eydoux, P., Babul-Hirji, R., An, J., Marra, M. A., FORGE Canada Consortium, Chitayat, D., Boycott, K. M., Weaver, D. D., & Jones, S. J. (2012). Mutations in EZH2 cause Weaver syndrome. *American Journal of Human Genetics*, *90*(1), 110–118. https://doi.org/10.1016/j.ajhg.2011.11.018

Glickstein, S. B., Moore, H., Slowinska, B., Racchumi, J., Suh, M., Chuhma, N., & Ross, M. E. (2007). Selective cortical interneuron and GABA deficits in cyclin D2-null mice. *Development*, *134*(22), 4083–4093. https://doi.org/10.1242/dev.008524

Gorlin, R. J., Cohen, M. M., Jr., Condon, L. M., & Burke, B. A. (1992). Bannayan–Riley–Ruvalcaba syndrome. *American Journal of Medical Genetics*, *44*(3), 307–314. https://doi.org/10.1002/ajmg.1320440309

Grabinski, N., Bartkowiak, K., Grupp, K., Brandt, B., Pantel, K., & Jucker, M. (2011). Distinct functional roles of Akt isoforms for proliferation, survival, migration and EGF-mediated signalling in lung cancer derived disseminated tumor cells. *Cellular Signalling*, *23*(12), 1952–1960. https://doi.org/10.1016/j.cellsig.2011.07.003

Graham, S. E., Tweedy, S. E., & Carlson, H. A. (2016). Dynamic behavior of the post-SET loop region of NSD1: Implications for histone binding and drug development. *Protein Science*, *25*(5), 1021–1029. https://doi.org/10.1002/pro.2912

Grissom, N. M., & Reyes, T. M. (2013). Gestational overgrowth and undergrowth affect neurodevelopment: Similarities and differences from behavior to epigenetics. *International Journal of Developmental Neuroscience*, *31*(6), 406–414. https://doi.org/10.1016/j.ijdevneu.2012.11.006

Gulsuner, S., Walsh, T., Watts, A. C., Lee, M. K., Thornton, A. M., Casadei, S., Rippey, C., Shahin, H., Consortium on the Genetics of Schizophrenia (COGS), PAARTNERS Study Group, Nimgaonkar, V. L., Go, R. C., Savage, R. M., Swerdlow, N. R., Gur, R. E., Braff, D. L., King, M. C., & McClellan, J. M. (2013). Spatial and temporal mapping of de novo mutations in schizophrenia to a fetal prefrontal cortical network. *Cell*, *154*(3), 518–529. https://doi.org/10.1016/j.cell.2013.06.049

Han, Y. C., Vidigal, J. A., Mu, P., Yao, E., Singh, I., Gonzalez, A. J., Concepcion, C. P., Bonetti, C., Ogrodowski, P., Carver, B., Selleri, L., Betel, D., Leslie, C., & Ventura, A. (2015). An allelic series of miR-17 approximately 92-mutant mice uncovers functional specialization and cooperation among members of a microRNA polycistron. *Nature Genetics*, *47*(7), 766–775. https://doi.org/10.1038/ng.3321

Harada, A., Miya, F., Utsunomiya, H., Kato, M., Yamanaka, T., Tsunoda, T., Kosaki, K., Kanemura, Y., & Yamasaki, M. (2015). Sudden death in a case of megalencephaly capillary malformation associated with a de novo mutation in AKT3. *Child's Nervous System*, *31*(3), 465–471. https://doi.org/10.1007/s00381-014-2589-y

Hemming, I. A., Forrest, A. R., Shipman, P., Woodward, K. J., Walsh, P., Ravine, D. G., & Heng, J. I. (2016). Reinforcing the association between distal 1q CNVs and structural brain disorder: A case of a complex 1q43-q44 CNV and a review of the literature. *American Journal of Medical Genetics. Part B, Neuropsychiatric Genetics*, *171B*(3), 458–467. https://doi.org/10.1002/ajmg.b.32427

Henriksson, M., & Luscher, B. (1996). Proteins of the Myc network: Essential regulators of cell growth and differentiation. *Advances in Cancer Research*, *68*, 109–182.

Herman, G. E., Butter, E., Enrile, B., Pastore, M., Prior, T. W., & Sommer, A. (2007). Increasing knowledge of PTEN germline mutations: Two additional patients with autism and macrocephaly. *American Journal of Medical Genetics. Part A*, *143A*(6), 589–593. https://doi.org/10.1002/ajmg.a.31619

Hermida, M. A., Dinesh Kumar, J., & Leslie, N. R. (2017). GSK3 and its interactions with the PI3K/AKT/mTOR signalling network. *Advances in Biological Regulation*, *65*, 5–15. https://doi.org/10.1016/j.jbior.2017.06.003

Hers, I., Vincent, E. E., & Tavare, J. M. (2011). Akt signalling in health and disease. *Cellular Signalling*, *23*(10), 1515–1527. https://doi.org/10.1016/j.cellsig.2011.05.004

Higashi, M., Sakai, K., Fumino, S., Aoi, S., Furukawa, T., & Tajiri, T. (2019). The roles played by the MYCN, Trk, and ALK genes in neuroblastoma and neural development. *Surgery Today*, *49*(9), 721–727. https://doi.org/10.1007/s00595-019-01790-0

Hiraiwa, A., Matsui, K., Nakayama, Y., Komatsubara, T., Magara, S., Kobayashi, Y., Hojo, M., Kato, M., Yamamoto, T., & Tohyama, J. (2021). Polymicrogyria with calcification in Pallister-Killian syndrome detected by microarray analysis. *Brain Dev*, *43*(3), 448–453. https://doi.org/10.1016/j.braindev.2020.11.003

Huard, J. M., Forster, C. C., Carter, M. L., Sicinski, P., & Ross, M. E. (1999). Cerebellar histogenesis is disturbed in mice lacking cyclin D2. *Development*, *126*(9), 1927–1935.

Hung, C. S., Wang, S., Yen, Y. T., Lee, T. H., Wen, W. C., & Lin, R. K. (2018). Hypermethylation of CCND2 in lung and breast cancer is a potential biomarker and drug target. *International Journal of Molecular Sciences*, *19*(10), 3096. https://doi.org/10.3390/ijms19103096

Igarashi, A., Itoh, K., Yamada, T., Adachi, Y., Kato, T., Murata, D., Sesaki, H., & Iijima, M. (2018). Nuclear PTEN deficiency causes microcephaly with decreased neuronal soma size and increased seizure susceptibility. *The Journal of Biological Chemistry*, *293*(24), 9292–9300. https://doi.org/10.1074/jbc.RA118.002356

Jamuar, S. S., Lam, A. T., Kircher, M., D'Gama, A. M., Wang, J., Barry, B. J., Zhang, X., Hill, R. S., Partlow, J. N., Rozzo, A., Servattalab, S., Mehta, B. K., Topcu, M., Amrom, D., Andermann, E., Dan, B., Parrini, E., Guerrini, R., Scheffer, I. E., … Walsh, C. A. (2014). Somatic mutations in cerebral cortical malformations. *The New England Journal of Medicine*, *371*(8), 733–743. https://doi.org/10.1056/NEJMoa1314432

Jansen, L. A., Mirzaa, G. M., Ishak, G. E., O'Roak, B. J., Hiatt, J. B., Roden, W. H., Gunter, S. A., Christian, S. L., Collins, S., Adams, C., Riviére, J. B., St-Onge, J., Ojemann, J. G., Shendure, J., Hevner, R. F., & Dobyns, W. B. (2015). PI3K/AKT pathway mutations cause a spectrum of brain malformations from megalencephaly to focal cortical dysplasia. *Brain*, *138*(Pt 6), 1613–1628. https://doi.org/10.1093/brain/awv045

Jeong, O. S., Chae, Y. C., Jung, H., Park, S. C., Cho, S. J., Kook, H., & Seo, S. (2016). Long noncoding RNA linc00598 regulates CCND2 transcription and modulates the G1 checkpoint. *Scientific Reports*, *6*, 32172. https://doi.org/10.1038/srep32172

Karczewski, K. J., Francioli, L. C., Tiao, G., Cummings, B. B., Alfoldi, J., Wang, Q., Collins, R. L., Laricchia, K. M., Ganna, A., Birnbaum, D. P., Gauthier, L. D., Brand, H., Solomonson, M., Watts, N. A., Rhodes, D., Singer-Berk, M., England, E. M., Seaby, E. G., Kosmicki, J. A., … MacArthur, D. G. (2020). The mutational constraint spectrum quantified from variation in 141,456 humans. *Nature*, *581*(7809), 434–443. https://doi.org/10.1038/s41586-020-2308-7

Kato, K., Miya, F., Hamada, N., Negishi, Y., Narumi-Kishimoto, Y., Ozawa, H., Ito, H., Hori, I., Hattori, A., Okamoto, N., Kato, M., Tsunoda, T., Kanemura, Y., Kosaki, K., Takahashi, Y., Nagata, K. I., & Saitoh, S. (2018). MYCN de novo gain-of-function mutation in a patient with a novel megalencephaly syndrome. *Journal of Medical Genetics*, *56*, 388–395. https://doi.org/10.1136/jmedgenet-2018-105487

Kircher, M., Witten, D. M., Jain, P., O'Roak, B. J., Cooper, G. M., & Shendure, J. (2014). A general framework for estimating the relative pathogenicity of human genetic variants. *Nature Genetics*, *46*(3), 310–315. https://doi.org/10.1038/ng.2892

Knoepfler, P. S., Cheng, P. F., & Eisenman, R. N. (2002). N-myc is essential during neurogenesis for the rapid expansion of progenitor cell populations and the inhibition of neuronal differentiation. *Genes & Development*, *16*(20), 2699–2712. https://doi.org/10.1101/gad.1021202

Kondratiuk, I., Plucinska, G., Miszczuk, D., Wozniak, G., Szydlowska, K., Kaczmarek, L., Filipkowski, R. K., & Lukasiuk, K. (2015). Epileptogenesis following kainic acid-induced status epilepticus in cyclin D2 knock-out mice with diminished adult neurogenesis. *PLoS One*, *10*(5), e0128285. https://doi.org/10.1371/journal.pone.0128285

Kurotaki, N., Imaizumi, K., Harada, N., Masuno, M., Kondoh, T., Nagai, T., Ohashi, H., Naritomi, K., Tsukahara, M., Makita, Y., Sugimoto, T., Sonoda, T., Hasegawa, T., Chinen, Y., Tomita, H. A., Kinoshita, A., Mizuguchi, T., Yoshiura, K. I., Ohta, T., … Matsumoto, N. (2002). Haploinsufficiency of NSD1 causes Sotos syndrome. *Nature Genetics*, *30*(4), 365–366. https://doi.org/10.1038/ng863

Kwon, C. H., Luikart, B. W., Powell, C. M., Zhou, J., Matheny, S. A., Zhang, W., Li, Y., Baker, S. J., & Parada, L. F. (2006). Pten regulates neuronal arborization and social interaction in mice. *Neuron*, *50*(3), 377–388. https://doi.org/10.1016/j.neuron.2006.03.023

Kwon, C. H., Zhu, X., Zhang, J., & Baker, S. J. (2003). mTor is required for hypertrophy of Pten-deficient neuronal soma in vivo. *Proceedings of the National Academy of Sciences of the United States of America*, *100*(22), 12923–12928. https://doi.org/10.1073/pnas.2132711100

Kwon, C. H., Zhu, X., Zhang, J., Knoop, L. L., Tharp, R., Smeyne, R. J., Eberhart, C. G., Burger, P. C., & Baker, S. J. (2001). Pten regulates neuronal soma size: A mouse model of Lhermitte–Duclos disease. *Nature Genetics*, *29*(4), 404–411. https://doi.org/10.1038/ng781

Lee, J. H., Huynh, M., Silhavy, J. L., Kim, S., Dixon-Salazar, T., Heiberg, A., Scott, E., Bafna, V., Hill, K. J., Collazo, A., Funari, V., Russ, C.,

Gabriel, S. B., Mathern, G. W., & Gleeson, J. G. (2012). De novo somatic mutations in components of the PI3K-AKT3-mTOR pathway cause hemimegalencephaly. *Nature Genetics*, *44*(8), 941–945. https://doi.org/10.1038/ng.2329

Lek, M., Karczewski, K. J., Minikel, E. V., Samocha, K. E., Banks, E., Fennell, T., O'Donnell-Luria, A. H., Ware, J. S., Hill, A. J., Cummings, B. B., Tukiainen, T., Birnbaum, D. P., Kosmicki, J. A., Duncan, L. E., Estrada, K., Zhao, F., Zou, J., Pierce-Hoffman, E., Berghout, J., … Exome Aggregation Consortium (2016). Analysis of protein-coding genetic variation in 60,706 humans. *Nature*, *536*(7616), 285–291. https://doi.org/10.1038/nature19057

Leone, G., Sears, R., Huang, E., Rempel, R., Nuckolls, F., Park, C. H., Giangrande, P., Wu, L., Saavedra, H. I., Field, S. J., Thompson, M. A., Yang, H., Fujiwara, Y., Greenberg, M. E., Orkin, S., Smith, C., & Nevins, J. R. (2001). Myc requires distinct E2F activities to induce S phase and apoptosis. *Molecular Cell*, *8*(1), 105–113.

Leyser, M., Dias, B. L., Coelho, A. L., Vasconcelos, M., & Nascimento, O. J. (2016). 12p deletion spectrum syndrome: A new case report reinforces the evidence regarding the potential relationship to autism spectrum disorder and related developmental impairments. *Molecular Cytogenetics*, *9*, 75. https://doi.org/10.1186/s13039-016-0278-0

Ling Wang, D. H., Jiang, Z., Luo, Y., Norris, C., Zhang, M., Tian, X., & Tang, Y. (2017). Akt3 is responsible for the survival and proliferation of embryonic stem cells. *Biol Open*, *6*(6), 850–861.

Lopes, F., Torres, F., Soares, G., van Karnebeek, C. D., Martins, C., Antunes, D., Silva, J., Muttucomaroe, L., Botelho, L. F., Sousa, S., Rendeiro, P., Tavares, P., Van Esch, H., Rajcan-Separovic, E., & Maciel, P. (2019). The role of AKT3 copy number changes in brain abnormalities and neurodevelopmental disorders: Four new cases and literature review. *Frontiers in Genetics*, *10*, 58. https://doi.org/10.3389/fgene.2019.00058

Lucio-Eterovic, A. K., Singh, M. M., Gardner, J. E., Veerappan, C. S., Rice, J. C., & Carpenter, P. B. (2010). Role for the nuclear receptor-binding SET domain protein 1 (NSD1) methyltransferase in coordinating lysine 36 methylation at histone 3 with RNA polymerase II function. *Proceedings of the National Academy of Sciences of the United States of America*, *107*(39), 16952–16957. https://doi.org/10.1073/pnas.1002653107

Lui, J. C., Barnes, K. M., Dong, L., Yue, S., Graber, E., Rapaport, R., Dauber, A., Nilsson, O., & Baron, J. (2018). Ezh2 mutations found in the weaver overgrowth syndrome cause a partial loss of H3K27 histone methyltransferase activity. *The Journal of Clinical Endocrinology and Metabolism*, *103*(4), 1470–1478. https://doi.org/10.1210/jc.2017-01948

Luo, A., Cheng, D., Yuan, S., Li, H., Du, J., Zhang, Y., Yang, C., Lin, G., Zhang, W., & Tan, Y. Q. (2018). Maternal interchromosomal insertional translocation leading to 1q43-q44 deletion and duplication in two siblings. *Molecular Cytogenetics*, *11*, 24. https://doi.org/10.1186/s13039-018-0371-7

Marcelis, C. L., Hol, F. A., Graham, G. E., Rieu, P. N., Kellermayer, R., Meijer, R. P., Lugtenberg, D., Scheffer, H., van Bokhoven, H., Brunner, H. G., & de Brouwer, A. P. (2008). Genotype–phenotype correlations in MYCN-related Feingold syndrome. *Human Mutation*, *29*(9), 1125–1132. https://doi.org/10.1002/humu.20750

Marsh, D. J., Coulon, V., Lunetta, K. L., Rocca-Serra, P., Dahia, P. L., Zheng, Z., Liaw, D., Caron, S., Duboué, B., Lin, A. Y., Richardson, A. L., Bonnetblanc, J. M., Bressieux, J. M., Cabarrot-Moreau, A., Chompret, A., Demange, L., Eeles, R. A., Yahanda, A. M., Fearon, E. R., … Eng, C. (1998). Mutation spectrum and genotype–phenotype analyses in Cowden disease and Bannayan–Zonana syndrome, two hamartoma syndromes with germline PTEN mutation. *Human Molecular Genetics*, *7*(3), 507–515.

McMichael, G., Bainbridge, M. N., Haan, E., Corbett, M., Gardner, A., Thompson, S., Van Bon, B. W. M., Van Eyk, C. L., Broadbent, J., Reynolds, C., O'Callaghan, M. E., Nguyen, L. S., Adelson, D. L., Russo, R., Jhangiani, S., Doddapaneni, H., Muzny, D. M., Gibbs, R. A., Gecz, J., & MacLennan, A. H. (2015). Whole-exome sequencing points to considerable genetic heterogeneity of cerebral palsy. *Molecular Psychiatry*, *20*(2), 176–182. https://doi.org/10.1038/mp.2014.189

Mercedes Bloch, A. L., Diplas, A. A., Pepermans, X., Emanuel, B. S., Rocca, M. S., Revencu, N., & Sznajer, Y. (2014). Further phenotype description, genotype characterization in patients with de novo interstitial deletion on 2p23.2-24.1. *American Journal of Medical Genetics. Part A*, *164A*(7), 1789–1794. https://doi.org/10.1002/ajmg.a.36516

Miao, L., Yang, L., Huang, H., Liang, F., Ling, C., & Hu, Y. (2016). mTORC1 is necessary but mTORC2 and GSK3beta are inhibitory for AKT3-induced axon regeneration in the central nervous system. *eLife*, *5*, e14908. https://doi.org/10.7554/eLife.14908

Migdalska, A. M., van der Weyden, L., Ismail, O., Sanger Mouse Genetics, P., Rust, A. G., Rashid, M., White, J. K., Sánchez-Andrade, G., Lupski, J. R., Logan, D. W., Arends, M. J., & Adams, D. J. (2012). Generation of the Sotos syndrome deletion in mice. *Mammalian Genome*, *23*(11–12), 749–757. https://doi.org/10.1007/s00335-012-9416-0

Mirzaa, G. M. (1993). MPPH syndrome. In MP Adams, HH Ardinger, RA Pagon, SE Wallace, LJH Bean, GM Mirzaa, & A Anemiya (Eds.), GeneReviews®. Seattle (WA): University of Washington, Seattle.

Mirzaa, G., Parry, D. A., Fry, A. E., Giamanco, K. A., Schwartzentruber, J., Vanstone, M., Logan, C. V., Roberts, N., Johnson, C. A., Singh, S., Kholmanskikh, S. S., Adams, C., Hodge, R. D., Hevner, R. F., Bonthron, D. T., Braun, K., Faivre, L., Riviére, J. B., St-Onge, J., Gripp, K. W., … Sheridan, E. G. (2014). De novo CCND2 mutations leading to stabilization of cyclin D2 cause megalencephaly-polymicrogyria-polydactyly-hydrocephalus syndrome. *Nature Genetics*, *46*(5), 510–515. https://doi.org/10.1038/ng.2948

Murai, Y., Dobashi, Y., Okada, E., Ishizawa, S., Shiota, M., Mori, S., & Takano, Y. (2001). Study on the role of G1 cyclins in Epstein-Barr virus-associated human lymphomas maintained in severe combined immune deficiency (SCID) mice. *International Journal of Cancer*, *92*(2), 232–239. https://doi.org/10.1002/1097-0215(200102)9999:9999<::aid-ijc1171>3.0.co;2-r

Mure, H., Matsuzaki, K., Kitazato, K. T., Mizobuchi, Y., Kuwayama, K., Kageji, T., & Nagahiro, S. (2010). Akt2 and Akt3 play a pivotal role in malignant gliomas. *Neuro-Oncology*, *12*(3), 221–232. https://doi.org/10.1093/neuonc/nop026

Muriello, M., Kim, A. Y., Sondergaard Schatz, K., Beck, N., Gunay-Aygun, M., & Hoover-Fong, J. E. (2019). Growth hormone deficiency, aortic dilation, and neurocognitive issues in Feingold syndrome 2. *American Journal of Medical Genetics. Part A*, *179*(3), 410–416. https://doi.org/10.1002/ajmg.a.61037

Nakamura, K., Kato, M., Tohyama, J., Shiohama, T., Hayasaka, K., Nishiyama, K., Kodera, H., Nakashima, M., Tsurusaki, Y., Miyake, N., Matsumoto, N., & Saitsu, H. (2014). AKT3 and PIK3R2 mutations in two patients with megalencephaly-related syndromes: MCAP and MPPH. *Clinical Genetics*, *85*(4), 396–398. https://doi.org/10.1111/cge.12188

Negishi, Y., Miya, F., Hattori, A., Johmura, Y., Nakagawa, M., Ando, N., Hori, I., Togawa, T., Aoyama, K., Ohashi, K., Fukumura, S., Mizuno, S., Umemura, A., Kishimoto, Y., Okamoto, N., Kato, M., Tsunoda, T., Yamasaki, M., Kanemura, Y., … Saitoh, S. (2017). A combination of genetic and biochemical analyses for the diagnosis of PI3K-AKT-mTOR pathway-associated megalencephaly. *BMC Medical Genetics*, *18*(1), 4. https://doi.org/10.1186/s12881-016-0363-6

Nellist, M., Schot, R., Hoogeveen-Westerveld, M., Neuteboom, R. F., van der Louw, E. J., Lequin, M. H., Bindels-de Heus, K., Sibbles, B. J., de Coo, R., Brooks, A., & Mancini, G. M. (2015). Germline activating AKT3 mutation associated with megalencephaly, polymicrogyria, epilepsy and hypoglycemia. *Molecular Genetics and Metabolism*, *114*(3), 467–473. https://doi.org/10.1016/j.ymgme.2014.11.018

Oliveira, D., Leal, G. F., Sertie, A. L., Caires, L. C., Jr., Goulart, E., Musso, C. M., Oliveira, J., Krepischi, A., Vianna-Morgante, A. M., & Zatz, M. (2019). 10q23.31 microduplication encompassing PTEN decreases mTOR signalling activity and is associated with autosomal dominant primary microcephaly. *Journal of Medical Genetics*, *56*(8), 543–547. https://doi.org/10.1136/jmedgenet-2018-105471

Orrico, A., Galli, L., Buoni, S., Orsi, A., Vonella, G., & Sorrentino, V. (2009). Novel PTEN mutations in neurodevelopmental disorders and macrocephaly. *Clinical Genetics*, *75*(2), 195–198. https://doi.org/10.1111/j.1399-0004.2008.01074.x

Otto, T., Horn, S., Brockmann, M., Eilers, U., Schuttrumpf, L., Popov, N., Kenney, A. M., Schulte, J. H., Beijersbergen, R., Christiansen, H., Berwanger, B., & Eilers, M. (2009). Stabilization of N-Myc is a critical function of Aurora A in human neuroblastoma. *Cancer Cell*, *15*(1), 67–78. https://doi.org/10.1016/j.ccr.2008.12.005

Ouimet, B., Pepin, E., Bergeron, Y., Chagniel, L., Beaulieu, J. M., Massicotte, G., & Cyr, M. (2019). Motor learning deficits and striatal GSK-3 hyperactivity in Akt3 knockout mice. *Behavioral Neuroscience*, *133*(1), 135–143. https://doi.org/10.1037/bne0000292

Poduri, A., Evrony, G. D., Cai, X., Elhosary, P. C., Beroukhim, R., Lehtinen, M. K., Hills, L. B., Heinzen, E. L., Hill, A., Hill, R. S., Barry, B. J., Bourgeois, B. F. D., Riviello, J. J., Barkovich, A. J., Black, P. M., Ligon, K. L., & Walsh, C. A. (2012). Somatic activation of AKT3 causes hemispheric developmental brain malformations. *Neuron*, *74*(1), 41–48. https://doi.org/10.1016/j.neuron.2012.03.010

Riviere, J. B., Mirzaa, G. M., O'Roak, B. J., Beddaoui, M., Alcantara, D., Conway, R. L., St-Onge, J., Schwartzentruber, J. A., Gripp, K. W., Nikkel, S. M., Worthylake, T., Sullivan, C. T., Ward, T. R., Butler, H. E., Kramer, N. A., Albrecht, B., Armour, C. M., Armstrong, L., Caluseriu, O., … Dobyns, W. B. (2012). De novo germline and postzygotic mutations in AKT3, PIK3R2 and PIK3CA cause a spectrum of related megalencephaly syndromes. *Nature Genetics*, *44*(8), 934–940. https://doi.org/10.1038/ng.2331

Ross, M. E., Carter, M. L., & Lee, J. H. (1996). MN20, a D2 cyclin, is transiently expressed in selected neural populations during embryogenesis. *The Journal of Neuroscience*, *16*(1), 210–219.

Rushlow, D. E., Mol, B. M., Kennett, J. Y., Yee, S., Pajovic, S., Theriault, B. L., Prigoda-Lee, N. L., Spencer, C., Dimaras, H., Corson, T. W., Pang, R., Massey, C., Godbout, R., Jiang, Z., Zacksenhaus, E., Paton, K., Moll, A. C., Houdayer, C., Raizis, A., … Gallie, B. L. (2013). Characterisation of retinoblastomas without RB1 mutations: Genomic, gene expression, and clinical studies. *The Lancet Oncology*, *14*(4), 327–334. https://doi.org/10.1016/S1470-2045(13)70045-7

Sachwitz, J., Meyer, R., Fekete, G., Spranger, S., Matuleviciene, A., Kucinskas, V., Bach, A., Luczay, A., Brüchle, N. O., Eggermann, K., Zerres, K., Elbracht, M., & Eggermann, T. (2017). NSD1 duplication in Silver–Russell syndrome (SRS): Molecular karyotyping in patients with SRS features. *Clinical Genetics*, *91*(1), 73–78. https://doi.org/10.1111/cge.12803

Schwarz, J. M., Cooper, D. N., Schuelke, M., & Seelow, D. (2014). MutationTaster2: Mutation prediction for the deep-sequencing age. *Nature Methods*, *11*(4), 361–362. https://doi.org/10.1038/nmeth.2890

Sellars, E. A., Zimmerman, S. L., Smolarek, T., & Hopkin, R. J. (2011). Ventricular noncompaction and absent thumbs in a newborn with tetrasomy 5q35.2-5q35.3: An association with hunter-McAlpine syndrome? *American Journal of Medical Genetics. Part A*, *155A*(6), 1409–1413. https://doi.org/10.1002/ajmg.a.33997

Sherry, S. T., Ward, M. H., Kholodov, M., Baker, J., Phan, L., Smigielski, E. M., & Sirotkin, K. (2001). dbSNP: The NCBI database of genetic variation. *Nucleic Acids Research*, *29*(1), 308–311. https://doi.org/10.1093/nar/29.1.308

Siavriene, E., Preikšaitiene, E., Maldžiene, Ž., Mikstiene, V., Rančelis, T., Ambrozaityte, L., Gueneau, L., Reymond, A., & Kučinskas, V. (2020). A de novo 13q31.3 microduplication encompassing the miR-17 ~92 cluster results in features mirroring those associated with Feingold syndrome 2. *Gene*, *753*, 144816. https://doi.org/10.1016/j.gene.2020.144816

Sicinski, P., Donaher, J. L., Geng, Y., Parker, S. B., Gardner, H., Park, M. Y., Robker, R. L., Richards, J. A. S., McGinnis, L. K., Biggers, J. D., Eppig, J. J., Bronson, R. T., Elledge, S. J., & Weinberg, R. A. (1996). Cyclin D2 is an FSH-responsive gene involved in gonadal cell proliferation and oncogenesis. *Nature*, *384*(6608), 470–474. https://doi.org/10.1038/384470a0

Sobreira, N., Schiettecatte, F., Valle, D., & Hamosh, A. (2015). GeneMatcher: A matching tool for connecting investigators with an interest in the same gene. *Human Mutation*, *36*(10), 928–930. https://doi.org/10.1002/humu.22844

Tatton-Brown, K., Douglas, J., Coleman, K., Baujat, G., Cole, T. R., Das, S., Horn, D., Hughes, H. E., Temple, I. K., Faravelli, F., Waggoner, D., Turkmen, S., Cormier-Daire, V., Irrthum, A., Rahman, N., & Childhood Overgrowth Collaboration (2005). Genotype–phenotype associations in Sotos syndrome: An analysis of 266 individuals with NSD1 aberrations. *American Journal of Human Genetics*, *77*(2), 193–204. https://doi.org/10.1086/432082

Tatton-Brown, K., Hanks, S., Ruark, E., Zachariou, A., Duarte, S., Ramsay, E., Snape, K., Murray, A., Perdeaux, E. R., Seal, S., Loveday, C., Banka, S., Clericuzio, C., Flinter, F., Magee, A., McConnell, V., Patton, M., Raith, W., Rankin, J., … Rahman, N. (2011). Germline mutations in the oncogene EZH2 cause Weaver syndrome and increased human height. *Oncotarget*, *2*(12), 1127–1133. https://doi.org/10.18632/oncotarget.385

Tatton-Brown, K., Murray, A., Hanks, S., Douglas, J., Armstrong, R., Banka, S., Bird, L. M., Clericuzio, C. L., Cormier-Daire, V., Cushing, T., Flinter, F., Jacquemont, M. L., Joss, S., Kinning, E., Lynch, S. A., Magee, A., McConnell, V., Medeira, A., Ozono, K., … Rahman, N. (2013). Weaver syndrome and EZH2 mutations: Clarifying the clinical phenotype. *American Journal of Medical Genetics. Part A*, *161A*(12), 2972–2980. https://doi.org/10.1002/ajmg.a.36229

Tatton-Brown, K., & Weksberg, R. (2013). Molecular mechanisms of childhood overgrowth. *American Journal of Medical Genetics. Part C, Seminars in Medical Genetics*, *163C*(2), 71–75. https://doi.org/10.1002/ajmg.c.31362

Tavana, O., Li, D., Dai, C., Lopez, G., Banerjee, D., Kon, N., Chen, C., Califano, A., Yamashiro, D. J., Sun, H., & Gu, W. (2016). HAUSP deubiquitinates and stabilizes N-Myc in neuroblastoma. *Nature Medicine*, *22*(10), 1180–1186. https://doi.org/10.1038/nm.4180

Tracy, B., Graham, J. M., Jr., Feldman, G., Perin, J., Catherwood, A., Knowlton, R., Rappaport, E. F., Emanuel, B., Driscoll, D. A., & Saitta, S. C. (2011). High-resolution genomic arrays identify CNVs that phenocopy the chromosome 22q11.2 deletion syndrome. *Human Mutation*, *32*(1), 91–97. https://doi.org/10.1002/humu.21395

Varga, E. A., Pastore, M., Prior, T., Herman, G. E., & McBride, K. L. (2009). The prevalence of PTEN mutations in a clinical pediatric cohort with autism spectrum disorders, developmental delay, and macrocephaly. *Genetics in Medicine*, *11*(2), 111–117. https://doi.org/10.1097/GIM.0b013e31818fd762

Wang, D., Zeesman, S., Tarnopolsky, M. A., & Nowaczyk, M. J. (2013). Duplication of AKT3 as a cause of macrocephaly in duplication 1q43q44. *American Journal of Medical Genetics. Part A*, *161A*(8), 2016–2019. https://doi.org/10.1002/ajmg.a.35999

Wang, J. C., Steinraths, M., Dang, L., Lomax, B., Eydoux, P., Stockley, T., Yong, S. L., & Van Allen, M. I. (2007). Craniosynostosis associated with distal 5q-trisomy: Further evidence that extra copy of MSX2 gene leads to craniosynostosis. *American Journal of Medical Genetics. Part A*, *143A*(24), 2931–2936. https://doi.org/10.1002/ajmg.a.31946

Wang, Z., Xie, Y., Zhang, L., Zhang, H., An, X., Wang, T., & Meng, A. (2008). Migratory localization of cyclin D2-Cdk4 complex suggests a spatial regulation of the G1-S transition. *Cell Structure and Function*, *33*(2), 171–183.

Xiong, Y., Menninger, J., Beach, D., & Ward, D. C. (1992). Molecular cloning and chromosomal mapping of CCND genes encoding human D-type cyclins. *Genomics*, *13*(3), 575–584.

Xue, C., Yu, D. M., Gherardi, S., Koach, J., Milazzo, G., Gamble, L., Liu, B., Valli, E., Russell, A. J., London, W. B., Liu, T., Cheung, B. B., Marshall, G. M., Perini, G., Haber, M., & Norris, M. D. (2016). MYCN promotes neuroblastoma malignancy by establishing a regulatory circuit with transcription factor AP4. *Oncotarget*, *7*(34), 54937–54951. https://doi.org/10.18632/oncotarget.10709

Yang, Z. Z., Tschopp, O., Di-Poi, N., Bruder, E., Baudry, A., Dummler, B., Wahli, W., & Hemmings, B. A. (2005). Dosage-dependent effects of Akt1/protein kinase Balpha (PKBalpha) and Akt3/PKBgamma on thymus, skin, and cardiovascular and nervous system development in mice. *Molecular and Cellular Biology*, *25*(23), 10407–10418. https://doi.org/10.1128/MCB.25.23.10407-10418.2005

Yuen, R. K., Thiruvahindrapuram, B., Merico, D., Walker, S., Tammimies, K., Hoang, N., Chrysler, C., Nalpathamkalam, T., Pellecchia, G., Liu, Y., Gazzellone, M. J., D'Abate, L., Deneault, E., Howe, J. L., Liu, R. S., Thompson, A., Zarrei, M., Uddin, M., Marshall, C. R., Ring, R. H., … Scherer, S. W. (2015). Whole-genome sequencing of quartet families with autism spectrum disorder. *Nature Medicine*, *21*(2), 185–191. https://doi.org/10.1038/nm.3792

Zhang, H., Lu, X., Beasley, J., Mulvihill, J. J., Liu, R., Li, S., & Lee, J. Y. (2011). Reversed clinical phenotype due to a microduplication of Sotos syndrome region detected by array CGH: Microcephaly, developmental delay and delayed bone age. *American Journal of Medical Genetics. Part A*, *155A*(6), 1374–1378. https://doi.org/10.1002/ajmg.a.33769

Zhou, X. P., Waite, K. A., Pilarski, R., Hampel, H., Fernandez, M. J., Bos, C., Dasouki, M., Feldman, G. L., Greenberg, L. A., Ivanovich, J., Matloff, E., Patterson, A., Pierpont, M. E., Russo, D., Nassif, N. T., & Eng, C. (2003). Germline PTEN promoter mutations and deletions in Cowden/Bannayan–Riley–Ruvalcaba syndrome result in aberrant PTEN protein and dysregulation of the phosphoinositol-3-kinase/Akt pathway. *American Journal of Human Genetics*, *73*(2), 404–411. https://doi.org/10.1086/377109

SUPPORTING INFORMATION

Additional supporting information may be found online in the Supporting Information section at the end of this article.

American College of Rheumatology
Empowering Rheumatology Professionals

Arthritis & Rheumatology
Vol. 74, No. 2, February 2022, pp 284–294
DOI 10.1002/art.41937

Evaluation of Immune Response and Disease Status in Systemic Lupus Erythematosus Patients Following SARS–CoV-2 Vaccination

Peter M. Izmirly,[1] Mimi Y. Kim,[2] Marie Samanovic,[1] Ruth Fernandez-Ruiz,[1] Sharon Ohana,[1] Kristina K. Deonaraine,[1] Alexis J. Engel,[1] Mala Masson,[1] Xianhong Xie,[2] Amber R. Cornelius,[1] Ramin S. Herati,[1] Rebecca H. Haberman,[1] Jose U. Scher,[1] Allison Guttmann,[1] Rebecca B. Blank,[1] Benjamin Plotz,[1] Mayce Haj-Ali,[1] Brittany Banbury,[1] Sara Stream,[1] Ghadeer Hasan,[1] Gary Ho,[1] Paula Rackoff,[1] Ashira D. Blazer,[1] Chung-E Tseng,[1] H. Michael Belmont,[1] Amit Saxena,[1] Mark J. Mulligan,[1] Robert M. Clancy,[1] and Jill P. Buyon[1]

Objective. To evaluate seroreactivity and disease flares after COVID-19 vaccination in a multiethnic/multiracial cohort of patients with systemic lupus erythematosus (SLE).

Methods. Ninety SLE patients and 20 healthy controls receiving a complete COVID-19 vaccine regimen were included. IgG seroreactivity to the SARS–CoV-2 spike receptor-binding domain (RBD) and SARS–CoV-2 microneutralization were used to evaluate B cell responses; interferon-γ (IFNγ) production was measured by enzyme-linked immunospot (ELISpot) assay in order to assess T cell responses. Disease activity was measured by the hybrid SLE Disease Activity Index (SLEDAI), and flares were identified according to the Safety of Estrogens in Lupus Erythematosus National Assessment–SLEDAI flare index.

Results. Overall, fully vaccinated SLE patients produced significantly lower IgG antibodies against SARS–CoV-2 spike RBD compared to fully vaccinated controls. Twenty-six SLE patients (28.8%) generated an IgG response below that of the lowest control (<100 units/ml). In logistic regression analyses, the use of any immunosuppressant or prednisone and a normal anti–double-stranded DNA antibody level prior to vaccination were associated with decreased vaccine responses. IgG seroreactivity to the SARS–CoV-2 spike RBD strongly correlated with the SARS–CoV-2 microneutralization titers and correlated with antigen-specific IFNγ production determined by ELISpot. In a subset of patients with poor antibody responses, IFNγ production was similarly diminished. Pre- and postvaccination SLEDAI scores were similar in both groups. Postvaccination flares occurred in 11.4% of patients; 1.3% of these were severe.

Conclusion. In a multiethnic/multiracial study of SLE patients, 29% had a low response to the COVID-19 vaccine which was associated with receiving immunosuppressive therapy. Reassuringly, severe disease flares were rare. While minimal protective levels remain unknown, these data suggest that protocol development is needed to assess the efficacy of booster vaccination.

INTRODUCTION

As scientific advances have been applied with unprecedented speed during the COVID-19 pandemic, physicians and their patients have pivoted from treatment of infection and passive immunization to full-scale preventative measures, particularly in high-risk individuals (1,2). Patients with systemic lupus erythematosus (SLE) comprise a unique population with regard to risk for infection and outcomes associated with SARS–CoV-2, given underlying demographics, associated organ damage, and

Supported by the National Institute of Arthritis and Musculoskeletal and Skin Diseases, NIH (grant P50-AR-07059), the National Institute of Allergy and Infectious Diseases, NIH (grant AI-148574), and a Bloomberg Philanthropies COVID-19 Response Initiative grant.

[1]Peter M. Izmirly, MD, Marie Samanovic, PhD, Ruth Fernandez-Ruiz, MD, Sharon Ohana, BS, Kristina K. Deonaraine, MSc, Alexis J. Engel, BS, Mala Masson, BA, Amber R. Cornelius, MS, Ramin S. Herati, MD, Rebecca H. Haberman, MD, Jose U. Scher, MD, Allison Guttmann, MD, Rebecca B. Blank, MD, Benjamin Plotz, MD, Mayce Haj-Ali, MD, Brittany Banbury, MD, Sara Stream, MD, Ghadeer Hasan, MD, Gary Ho, MD, Paula Rackoff, MD, Ashira D. Blazer, MD, Chung-E Tseng, MD, H. Michael Belmont, MD, Amit Saxena, MD, Mark J. Mulligan, MD, Robert M. Clancy, PhD, Jill P. Buyon, MD: New York University Grossman School of Medicine, New York, New York;

[2]Mimi Y. Kim, ScD, Xianhong Xie, PhD: Albert Einstein College of Medicine, New York, New York.

Drs. Izmirly, Kim, Samanovic, and Fernandez-Ruiz contributed equally to this work. Drs. Mulligan, Clancy, and Buyon contributed equally to this work.

Author disclosures are available at https://onlinelibrary.wiley.com/action/downloadSupplement?doi=10.1002%2Fart.41937&file=art41937-sup-0001-Disclosureform.pdf.

Address correspondence to Peter M. Izmirly, MD, NYU Langone Health, 550 First Avenue, Medical Science Building 625, New York, NY 10016. Email: peter.izmirly@nyulangone.org.

Submitted for publication June 4, 2021; accepted in revised form July 29, 2021.

comorbidities. In addition, medications commonly used to treat SLE have been associated with an increased risk of death from COVID-19 (3). Early data provided evidence that patients with SLE have a high risk of hospitalization from COVID-19, with factors including race/ethnicity, comorbidities such as cardiovascular disease and renal insufficiency, and higher body mass index identified as independent predictors of hospitalization (1,4). Further raising concern, infection was reported to be associated with flares of disease (5). In subsequent studies, patients with SLE and confirmed COVID-19 were demonstrated to generate and maintain serologic responses despite the use of a variety of immunosuppressants (6). These data provided reassurance regarding the efficacy and durability of humoral immunity and protection against reinfection with SARS–CoV-2, as well as potential insights into the efficacy of active immunization in SLE patients.

Since the phase III clinical studies of all 3 vaccines excluded patients treated with immunosuppressants or immune-modifying drugs within 6 months of enrollment, data on SLE are virtually absent (7–9). Furthermore, given the potential for disease flares following immunization, it is not surprising that a recent study reported hesitancy for vaccination in patients with rheumatic diseases, including SLE (10). Accordingly, the current study was initiated to address these critical gaps and examine the efficacy of these promising COVID-19 vaccines in patients with SLE. This was accomplished by evaluating a multiethnic/multiracial cohort of SLE patients using assessments of serologic responses which were compared to healthy controls. The assays included antibodies to the spike protein receptor-binding domain (RBD), virus-neutralizing antibodies, and antigen-specific T cell production of interferon-γ (IFNγ), both prior to and after vaccination. Factors associated with the level of responsiveness were sought. In addition, SLE disease activity pre- and postvaccination was measured, as well as the rate of flare postvaccination.

PATIENTS AND METHODS

Study population and inclusion/exclusion criteria. Patients were recruited from the established New York University (NYU) Lupus Cohort, a prospective convenience registry open to enrolling any patient with SLE seen at NYU Langone Health and Bellevue Hospital Center since 2014. All SLE patients in the NYU Lupus Cohort are age 18 or older and fulfill ≥1 of the following criteria: 1) the American College of Rheumatology (ACR) revised classification criteria (11); 2) the Systemic Lupus International Collaborating Clinics classification criteria (12); and/or 3) the European Alliance of Associations for Rheumatology/ACR classification criteria (13). All NYU Lupus Cohort patients and controls provided written informed consent, which was available in English, Spanish, and Mandarin. All adult patients with SLE planning to receive any of the available COVID-19 vaccines were eligible for inclusion. Exclusion criteria included unwillingness to provide blood after the second dose of the vaccine, incomplete vaccination schedule, and speaking a language other than English, Spanish, or Mandarin. Healthy controls were ≥18 years of age, had no known rheumatic diseases and were receiving no immunosuppressive medications. The study protocol and the NYU Lupus Cohort and recruitment of controls were approved by the NYU and Bellevue Hospital Institutional Review Boards.

Study design and data collection. Patients were recruited using convenience sampling, with inclusion and exclusion criteria as stated above. For most patients, blood samples were available pre- and postvaccination. Disease activity measures and laboratory data prior to vaccination were available as part of the NYU Lupus Cohort but were limited to patients seen within 4 months of their first vaccine dose. Postvaccination follow-ups were scheduled ~2 weeks after the second dose of the messenger RNA (mRNA) vaccines (i.e., BNT162b2 [Pfizer/BioNTech] or mRNA-1273 [Moderna]) or after 1 dose of Ad26.COV2.S (Johnson & Johnson) to collect postvaccination blood samples and assess for any change in SLE activity. Disease activity was measured by the hybrid Safety of Estrogens in Lupus Erythematosus National Assessment (SELENA)–SLE Disease Activity Index (SLEDAI) (urine protein:creatinine ratios >0.5 were always counted), and flares were assessed by the SELENA–SLEDAI flare index (14–16). In addition, the use and doses of immunosuppressive medications were recorded at each visit, including, among others, glucocorticoids, hydroxychloroquine (HCQ), azathioprine, mycophenolate mofetil (MMF), methotrexate (MTX), belimumab, and tacrolimus. Any cyclophosphamide, obinutuzumab, or rituximab administered within 6 months of the patient's visit was also recorded. Considering that our patients were largely enrolled before the ACR updated their guidelines to temporarily hold MMF used to treat more severe manifestations such as nephritis, that medication was not held. We did advise patients to hold MTX and adjusted other medications as recommended per this guidance (17).

Enzyme-linked immunosorbent assay (ELISA) for recombinant SARS–CoV-2 spike protein. Ninety-six–well plates were coated with 1 μg/ml recombinant SARS–CoV-2 spike RBD (no. BT10500; R&D Systems), diluted in phosphate buffered saline (PBS) and incubated overnight at 4°C. Plates were blocked with 0.1% gelatin in PBS. Plasma (spun 10,000 rpm for 1 minute) were diluted 1:200–1:100,000 and added to the plate for 1 hour at room temperature. Samples were run in triplicate. With each run, 2 positive controls were included in the 96-well plate: plasma from control (non-SLE) participants postvaccination, with high and low IgG titers, each diluted 1:500 to ensure that measurements were captured across the assay range. Detection relies on an enzyme-labeled secondary antibody, alkaline phosphatase–conjugated rabbit anti-human IgG (γ-chain–

Table 1. Characteristics of the vaccinated SLE patients and healthy controls*

	Controls (n = 20)	SLE patients (n = 90)
Age, mean ± SD years	45.3 ± 14.2	45.5 ± 14.2
Sex†		
Female	12 (60.0)	79 (87.8)
Male	8 (40.0)	11 (12.2)
Race		
White	13 (65.0)	43 (47.8)
Black	2 (10.0)	16 (17.8)
Asian	4 (20.0)	17 (18.9)
Other	1 (5.0%)	14 (15.5)
Ethnicity		
Hispanic/Latino	1 (5.0)	34 (37.8)
COVID-19 vaccine		
BNT162b2 (Pfizer)	17 (85.0)	61 (67.8)
mRNA-1273 (Moderna)	3 (15.0)	24 (26.7)
Ad26.COV2.S (Johnson & Johnson)	0 (0)	5 (5.5)
Days between 2nd vaccine dose and postvaccine blood draw, mean (range)	23 (14–31)	24 (5–69)
Prior history of COVID-19 (PCR or IgG)	2 (10.0)	11 (12.2)
SLE risk factors		
History of LN	N/A	40 (44.4)
Kidney transplant recipient	N/A	5 (5.6)
APS	N/A	9 (10.0)
Medication(s)		
HCQ	–	71 (79)
Dose, mean ± SD mg	–	321.0 ± 89.7
Chloroquine	–	1 (1)
Dose, mg	–	250.0
Prednisone	–	26 (29)
Dose, mean ± SD mg	–	7.2 ± 7.6
Immunosuppressants	–	38 (42)
AZA	–	5 (6)
Dose, mean ± SD mg	–	130.0 ± 27.4
MMF	–	19 (21)
Dose, mean ± SD mg	–	1,967.1 ± 731.1
Mycophenolic acid	–	2 (2)
Dose, mean ± SD mg	–	900.0 ± 254.6
Tacrolimus	–	5 (6)
Dose, mean ± SD mg	–	4.0 ± 2.3
MTX	–	8 (9)
Dose, mean ± SD mg‡	–	14.6 ± 6.0
Belimumab	–	10 (11)
Cyclophosphamide	–	0 (0)
Rituximab	–	3 (3)
Leflunomide	–	1 (1)
Abatacept	–	1 (1)
Adalimumab	–	1 (1)
Obinutuzumab	–	1 (1)
Eculizumab	–	1 (1)
Apremilast	–	1 (1)
SLE clinical trial	–	1 (1)
Prednisone + immunosuppressant	–	22 (24)
Combination immunosuppressants	–	15 (17)

* Except where indicated otherwise, values are the number (%) of subjects. SLE = systemic lupus erythematosus; PCR = polymerase chain reaction; LN = lupus nephritis; APS = antiphospholipid syndrome; N/A = not applicable; HCQ = hydroxychloroquine; AZA = azathioprine; MMF = mycophenolate mofetil.
† $P = 0.007$.
‡ Includes 1 patient with an unknown dose of methotrexate (MTX), prescribed at an outside institution.

specific) (Sigma) diluted 1:2,000. After developing with the addition of phosphatase substrate, the optical density (OD) was measured at 405 nm, and the reaction was evaluated when the low positive control reached an OD of 1. The OD measured for a tested sample was multiplied by the dilution factor, which gave an OD in the range of 0.3–0.8.

SARS–CoV-2 microneutralization assay. Viral neutralization activity of plasma was measured in an immunofluorescence-based microneutralization assay by detecting the neutralization of infectious virus in cultured Vero E6 cells (no. CRL-1586, African green monkey kidney cells; ATCC). Cells were maintained according to standard ATCC protocols. Briefly, Vero E6 cells were grown in minimum essential medium (MEM) supplemented with 10% heat-inactivated fetal bovine serum (FBS), 2 m*M* L-glutamine, and 1% of MEM Nonessential Amino Acid Solution (no. MT25025CI; Fisher). Cell cultures were grown in 75 or 150 cm^2 flasks at 37°C with 5% CO_2 and passaged 2–3 times per week using trypsin–EDTA. Cell cultures used for virus testing were prepared as subconfluent monolayers. All incubations containing cells were performed at 37°C with 5% CO_2. All SARS–CoV-2 infection assays were performed in the Centers for Disease Control and Prevention (CDC)/US Department of Agriculture–approved biosafety level 3 facility in compliance with NYU Grossman School of Medicine guidelines for biosafety level 3. SARS–CoV-2 isolate USA-WA1/2020, deposited by the CDC, was obtained through BEI Resources, National Institute of Allergy and Infectious Diseases, National Institutes of Health (NR-52281, GenBank accession no. MT233526). Serial dilutions of heat-inactivated plasma (56°C for 1 hour) were incubated with USA-WA1/2020 stock (at fixed 1×10^6 plaque-forming units/ml) for 1 hour at 37°C. One hundred microliters of the plasma–virus mix was then added to the cells and incubated at 37°C with 5% CO_2. Twenty-four hours postinfection, cells were fixed with 10% formalin solution (4% active formaldehyde) for 1 hour, stained with an anti-SARS–CoV-2 nucleocapsid antibody (no 10-605; ProSci), and a goat anti-mouse IgG Alexa Fluor 647 secondary antibody along with DAPI and visualized by microscopy with the CellInsight CX7 High-Content Screening Platform (ThermoFisher) and high-content software.

Enzyme-linked immunospot (ELISpot). ELISpot plates (Human IFNγ ELISpot Plus, no. 3420-4HPT-2) were preseeded under sterile conditions following the recommendations of the manufacturer (Mabtech) in duplicates with 250,000 cells per well from cryopreserved peripheral blood mononuclear cells (PBMCs) isolated from each participant. Cells were incubated for 24 hours with SARS–CoV-2 spike protein S1 (1 μg/well) (no. RP-87681; Invitrogen) or vehicle, in the presence of anti-CD28 (1 μg/ml) (Biolegend). Cells were removed by washing the wells with PBS + 1% FBS. Membrane was probed with a 1:1,000 dilution of the detection antibody provided by the manufacturer (1 hour at 22°C). After washing, plates were developed using tetramethylbenzidine substrate solution. Spots were imaged and counted using an ImmunoSpot S6 Analyzer (Cellular Technology Limited). For each sample, the monoclonal antibody CD3-2 was used to capture cytokine production as a positive control.

Statistical analysis. Categorical variables were summarized by computing counts and proportions of patients. Continuous variables are expressed as the mean ± SD or the median and interquartile range (IQR) or range, as appropriate. Two-group comparisons were performed using the chi-square or Fisher's exact test for categorical variables and the 2-sample *t*-test or Mann–Whitney U test for continuous variables. Spearman's rank correlation coefficient was computed for the association between the ELISA and microneutralization assays. An exploratory logistic regression analysis was also conducted to identify potential independent predictors of low postvaccine ELISA antibody response (≤100 units/ml, the lowest value seen in controls). Variable selection in the final model was based on both statistical significance ($P < 0.10$, given limited sample size and power of the study) as

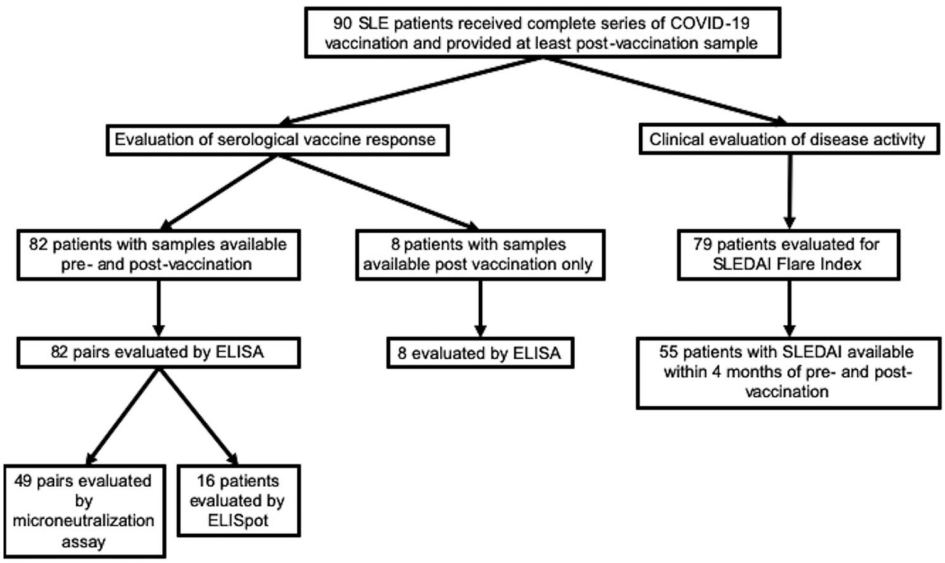

Figure 1. Flow diagram of the systemic lupus erythematosus (SLE) patients included in each analysis. ELISA = enzyme-linked immunosorbent assay; ELISpot = enzyme-linked immunospot; SLEDAI = SLE Disease Activity Index.

well as clinical considerations. All statistical analyses were performed using SAS version 9.4.

RESULTS

Patient population. A total of 90 patients with SLE and 20 controls were included in this study. Table 1 shows the demographics of the patients and controls in addition to SLE-specific information. Cases and controls were relatively well-matched; however, controls were more likely to be male ($P = 0.007$). Whereas controls only received the BNT162b2 and mRNA-1273 vaccines, SLE patients received all 3 vaccines currently available in the US, including Ad26.COV2.S. In addition, 12% of the SLE patients had a history of prior COVID-19 infection compared to 10% of controls. Forty-four percent of patients had a history of lupus nephritis (LN), 10% had secondary antiphospholipid syndrome (APS), and 5.6% had received a kidney transplant. The majority of SLE patients (79%) were receiving HCQ, and 29% were receiving systemic glucocorticoids (mean dose of 7 mg prednisone). Forty-two percent were receiving ≥1 immunosuppressant, with MMF being the most common (21%), followed by belimumab (11%). In addition, 17% of patients were receiving a combination of immunosuppressants. Figure 1 shows the number of SLE patients included in each subsequent analysis.

Decreased COVID-19 antibody responses in SLE patients compared to controls. Ninety SLE patients (82 with data from pre- and postvaccination analyses) and 20 healthy controls (all with data from pre- and postvaccination analyses) were evaluated for IgG antibody levels against the RBD of SARS–CoV-2 spike protein (anti-RBD) (Figures 2A–D). Overall, prevaccine levels in patients with SLE were significantly lower (median 9.1 [IQR 2.8–23.9]) than in controls (median 34.5 [IQR 11.2–74.0]; $P = 0.001$), as were the postvaccine levels (median 235.2 [IQR 75.9–531.4] versus median 435.7 [IQR 269.0–768.6], respectively; $P = 0.01$). Postvaccine antibody levels in 26 SLE patients (28.8%) fell below the lowest level of the controls (≤100 units/ml), which is shown in Figure 2D.

To address the functionality of the antibody responses assessed by ELISA, pre- and postvaccine samples from 49 SLE patients and 18 controls were also evaluated by the SARS–CoV-2 live microneutralization assay. As shown in Figure 2E, there was a strong correlation between the 2 assays (R = 0.76, $P < 0.0001$), suggesting that the ELISA is a good end point assay to evaluate the immune response to the vaccines. Similar to what we observed with the ELISA results, postvaccine microneutralization titers were significantly lower in SLE patients compared to controls ($P = 0.0075$) (Figure 2F).

A comparison of clinical and laboratory factors in the 64 SLE patients who generated responses to COVID-19 vaccine that were compatible with controls and the 26 patients with low responses who had ELISA results ≤100 units/ml is shown in Table 2. In unadjusted analyses, subjects with low responses were more likely to be receiving prednisone, MMF or mycophenolic acid, a combination of prednisone and ≥1 immunosuppressant, or ≥2 immunosuppressants, while those with high responses were more likely to only be receiving antimalarials or receiving no medication. In addition, low responders were

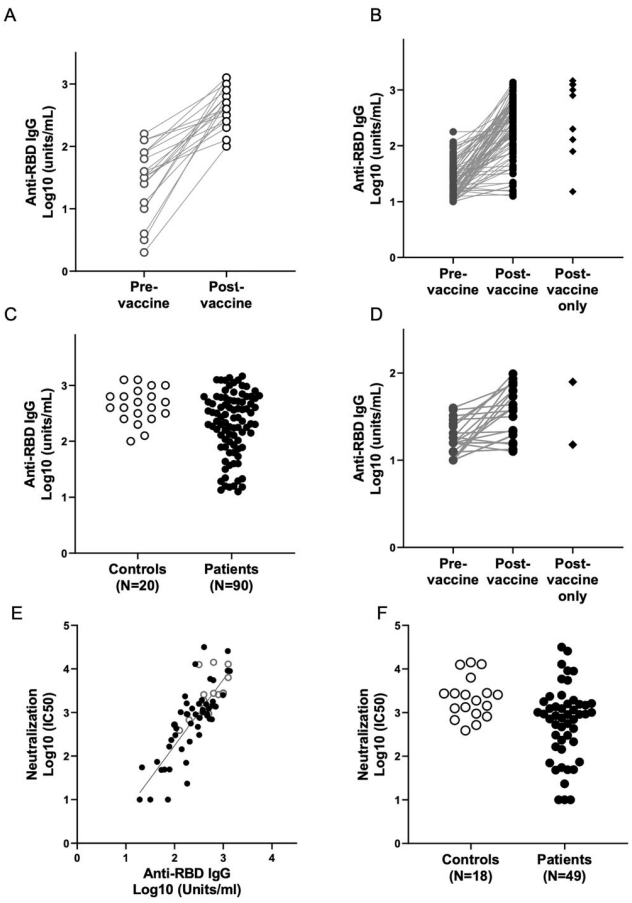

Figure 2. Antibody response to COVID-19 vaccine in SLE patients. Throughout, open circles represent controls, and solid circles represent SLE patients. Serum IgG titers against the SARS–CoV-2 spike protein receptor-binding domain (RBD) were obtained by direct ELISA. Binding of human IgG to recombinant SARS–CoV-2 RBD was performed as described in Patients and Methods. **A**, IgG titers of 20 controls pre- and postvaccination. **B**, IgG titers of 81 SLE patients pre- and postvaccination and 9 SLE patients with only postvaccination data available. **C**, Comparison of IgG titers postvaccination between the 2 groups, with controls showing significantly higher titers than SLE patients. **D**, IgG titers of a subgroup of patients (n = 24) from **B** with anti-RBD IgG ≤100 units/ml (the lowest response in controls). **E**, Correlation of SARS–CoV-2 virus neutralization titers in the sera of vaccinated subjects with IgG titers. Each dot represents the serum evaluation of a participant with binding of human IgG to recombinant SARS–CoV-2 RBD (x-axis) versus live virus neutralization at 50% inhibition concentration (IC_{50}; y-axis). There is a strong correlation between spike RBD IgG and live virus neutralization (R = 0.76, $P < 0.0001$). **F**, Log_{10} postvaccination neutralization titers for controls compared to SLE patients. See Figure 1 for other definitions.

Table 2. Bivariate analysis of predictors for poor postvaccine ELISA antibody response (≤100 units/ml) among the SLE patients*

	Postvaccine ELISA antibody response		
	≤100 units/ml (n = 26)	>100 units/ml (n = 64)	*P*
Age, mean ± SD years	47.7 ± 13.3	44.6 ± 14.5	0.36
Sex			0.29
Female	21 (80.8)	58 (90.6)	
Male	5 (19.2)	6 (9.4)	
Race			0.46
White	11 (42.3)	32 (50.0)	
Black	3 (11.5)	13 (20.3)	
Asian	7 (26.9)	10 (15.6)	
Other	5 (19.2)	9 (14.1)	
Ethnicity			0.93
Hispanic	10 (38.5)	24 (37.5)	
Non-Hispanic	16 (61.5)	40 (62.5)	
Days between 2nd vaccine dose and postvaccine blood draw, median (IQR)	19.5 (14.0–44.0)	17.0 (12.0–26.0)	0.11
Vaccine type			0.039
BNT162b2	15 (57.7)	46 (71.9)	
mRNA-1273	7 (26.9)	17 (26.6)	
Ad26.COV2.S	4 (15.4)	1 (1.6)	
Prior history of COVID-19 (PCR or IgG)	4 (18.2)	7 (13.7)	0.72
History of LN	15 (57.7)	25 (39.7)	0.12
Kidney transplant recipient	3 (11.5)	2 (3.1)	0.14
APS	0 (0)	9 (14.1)	0.055
Prednisone + ≥1 immunosuppressant	10 (38.5)	12 (18.8)	0.049
Combination immunosuppressants	9 (34.6)	6 (9.4)	0.01
Only antimalarials (HCQ + chloroquine) among those receiving medication	3 (12.0)	33 (56.9)	0.0002
Any MMF (MMF + mycophenolic acid)	12 (46.2)	9 (14.1)	0.001
Any prednisone	12 (46.2)	14 (21.9)	0.021
Any belimumab	4 (15.4)	6 (9.4)	0.47
No immunosuppressants	1 (3.8)	6 (9.4)	0.67
Only HCQ or no medications	4 (15.4)	39 (60.9)	<0.0001
Prevaccine anti-dsDNA antibody level†			0.023
Normal	14 (87.5)	28 (56.0)	
High	2 (12.5)	22 (44.0)	
C3 level			0.35
Low	3 (18.8)	17 (34.0)	
Normal	13 (81.3)	33 (66.0)	
C4 level			1.00
Low	4 (25.0)	12 (24.0)	
Normal	12 (75.0)	38 (76.0)	
SLEDAI score, mean ± SD†	2.00 ± 2.34	3.46 ± 4.16	0.085
Platelet count, mean ± SD × 10^3/μl†	202.81 ± 78.37	243.74 ± 85.60	0.095
Urine protein:creatinine ratio, mean ± SD†	0.17 ± 0.18	0.28 ± 0.58	0.26
Lymphocyte count, mean ± SD × 10^3/μl†	1.19 ± 0.65	1.36 ± 0.97	0.43

* Except where indicated otherwise, values are the number (%) of subjects. ELISA = enzyme-linked immunosorbent assay; SLE = systemic lupus erythematosus; IQR = interquartile range; PCR = polymerase chain reaction; LN = lupus nephritis; APS = antiphospholipid syndrome; HCQ = hydroxychloroquine; MMF = mycophenolate mofetil; anti-dsDNA = anti–double-stranded DNA (see Table 1 for other definitions).
† Laboratory measures and SLE Disease Activity Index (SLEDAI) scores were based on patients with prevaccine data available within 4 months of vaccine (n = 66).

more likely to have received Ad26.COV2.S, although sample sizes were limited, and to have had a normal anti–double-stranded DNA (anti-dsDNA) antibody level prior to vaccination (Table 2). Logistic regression analysis yielded a final model that included the following 4 independent predictors of low ELISA response among SLE patients: receiving any immunosuppressive therapy other than antimalarials (adjusted odds ratio [OR] 15.14 [95% CI 2.80–82.03] compared to antimalarials/no medications; $P = 0.002$), normal anti-dsDNA antibody level prior to vaccination (OR 14.50 [95% CI 2.20–95.66] compared to abnormal anti-dsDNA antibody level; $P = 0.006$), lower platelet count (OR 1.55 [95% CI 0.96–2.51] per 50 × 10^9 cells/liter decrease; $P = 0.07$), and normal C3 level (OR 4.95 [95% CI 0.91–26.0] compared to low C3 level; $P = 0.06$). A separate subgroup analysis including only those patients who were receiving any immunosuppressants confirmed the association of a normal anti-dsDNA

Table 3. Demographic information and medications of the SLE patients with lower vaccine responses (n = 26)*

Patient	Age	Sex	Vaccine type	Medication(s)
1	39	Male	BNT162b2	HCQ, MMF, obinutuzumab
2	71	Female	BNT162b2	MTX, abatacept
3	57	Female	BNT162b2	HCQ, belimumab
4	57	Female	BNT162b2	Prednisone (4 mg), HCQ, MTX, adalimumab
5	61	Female	BNT162b2	HCQ, MMF
6	42	Female	BNT162b2	HCQ, tacrolimus, rituximab
7	38	Female	BNT162b2	Prednisone (5 mg), mycophenolic acid, tacrolimus
8	59	Female	BNT162b2	Prednisone (5 mg), HCQ
9	62	Male	BNT162b2	HCQ, belimumab
10	54	Female	BNT162b2	HCQ
11	49	Female	BNT162b2	Prednisone (3 mg), MMF, belimumab
12	53	Female	BNT162b2	MMF
13	47	Female	BNT162b2	Prednisone (10 mg), HCQ, MMF
14	40	Male	BNT162b2	Prednisone (5 mg), HCQ, MMF
15	29	Female	BNT162b2	Prednisone (2.5 mg), HCQ, MMF
16	39	Male	mRNA-1273	HCQ, rituximab
17	46	Female	mRNA-1273	Prednisone (5 mg), HCQ, MMF
18	35	Female	mRNA-1273	HCQ, AZA, belimumab
19	66	Female	mRNA-1273	Prednisone (5 mg)
20	28	Female	mRNA-1273	HCQ
21	44	Female	mRNA-1273	HCQ
22	41	Female	mRNA-1273	Prednisone (20 mg), MMF
23	55	Female	Ad26.COV2.S	Prednisone (5 mg), HCQ, mycophenolic acid
24	72	Female	Ad26.COV2.S	None
25	27	Female	Ad26.COV2.S	HCQ, MMF
26	28	Male	Ad26.COV2.S	Prednisone (10 mg), MTX

* SLE = systemic lupus erythematosus; HCQ = hydroxychloroquine; MMF = mycophenolate mofetil; MTX = methotrexate; AZA = azathioprine.

antibody level with poor antibody response (OR 8.98 [95%CI 1.89–42.6]; $P = 0.006$ after adjustment for platelet and C3). Further details about the patients with lower responses are provided in Table 3.

Evaluation of IFNγ secretion in response to SARS–CoV-2 spike protein S1. Sixteen SLE patients (of whom 4 had pre- and postvaccine data available) and 2 controls (both with pre- and postvaccine data available) were further evaluated addressing T cell reactivity, which was operationally reported by the release of IFNγ in response to challenge of PBMCs in the absence and presence of the full-length S1 protein (COVID-19 antigen), as described in Patients and Methods. Individuals were chosen to represent a range of responses to the SARS–CoV-2 spike protein and SARS–CoV-2 microneutralization assay but with a particular focus on the patients with low seroreactivity on both assays. As shown in Supplementary Figure 1 (available on the *Arthritis & Rheumatology* website at http://onlinelibrary.wiley.com/doi/10.1002/art.41937/abstract), there was a correlation between the postvaccine ELISpot number and ELISA evaluations ($R = 0.57$, $P = 0.0135$). In a subset of patients with poor antibody responses, IFNγ production was likewise diminished (Supplementary Figure 1).

Stable disease activity in the majority of SLE patients after COVID-19 vaccination. Of the 90 patients evaluated, 55 patients had completed a SLEDAI assessment within 4 months of their first vaccine dose, which was then compared to their postvaccine SLEDAI assessment that was completed an average of 23.6 days (range 5–70) after the final vaccine dose (Supplementary Table 1, http://onlinelibrary.wiley.com/doi/10.1002/art.41937/abstract). Overall, there was no meaningful difference in SLEDAI score between pre- and postvaccine visits (3.2 versus 2.9). There were no changes in the percentages of patients with abnormal anti-dsDNA antibodies and/or abnormal complement levels; likewise, the levels of C3 and C4 were similar pre- and postvaccination (Supplementary Table 1). Nine of the 79 patients (11.4%) experienced a postvaccination flare, with all but 1 considered to be mild/moderate (2 in new organ systems: arthritis with no treatment and pericarditis treated with naproxen). The severe flare was characterized by arthritis and treated with MTX; the patient had discontinued HCQ due to maculopathy several years prior to vaccination. Further details of the flares are provided in Table 4.

DISCUSSION

To our knowledge, this is the first reported study focused on patients with SLE who received full regimens of a COVID-19 vaccine, and overall IgG antibody responses against the SARS–CoV-2 spike protein RBD were significantly decreased compared to vaccinated controls, with 28.8% of patients generating responses falling below the lowest level observed in the healthy

Table 4. SLE flares postvaccination*

Flare severity	Flare type	Flare details	Timing of flare	Vaccine type	Treatment
Mild/moderate	Pleuritis	Recurrent mild pleuritis	After 1st dose	BNT162b2	No treatment
Mild/moderate	Arthritis	Recurrent mild joint pain and swelling	After 2nd dose	BNT162b2	No treatment
Mild/moderate	Renal	Recurrent proteinuria; urine protein:creatinine ratio increased from 0.8 to 1.4	After 2nd dose	BNT162b2	Rituximab/tacrolimus changed to voclosporin
Mild/moderate	Oral ulcers	Recurrent oral ulcers; patient had been off of belimumab for 3 months	After 2nd dose	mRNA-1273	No treatment
Mild/moderate	Pericarditis	New presumed pericarditis, EKG negative; resolved with naproxen	After 2nd dose (2 weeks)	BNT162b2	Naproxen
Severe	Arthritis	Recurrent arthritis	After 2nd dose	mRNA-1273	Methotrexate
Mild/moderate	Thrombocytopenia	Recurrent thrombocytopenia within patient's range	After 2nd dose	BNT162b2	No treatment
Mild/moderate	Arthritis	New mild joint pain and swelling	After 2nd dose	BNT162b2	No treatment
Mild/moderate†	Thrombocytopenia	Recurrent thrombocytopenia	After 2nd dose	BNT162b2	No treatment
Non–SLE-related event	COPD/asthma flare		After 2nd dose	BNT162b2	Treated in emergency room with steroids, then released

* EKG = electrocardiogram; COPD = chronic obstructive pulmonary disease.
† A patient with systemic lupus erythematosus (SLE), antiphospholipid syndrome, and end-stage renal disease was admitted 13 days after the second vaccine dose. The patient had anticoagulation therapy temporarily withheld for a procedure, presented with shortness of breath, and was found to have superior vena cava syndrome. The patient had a prolonged hospital course, complicated by bleeding and sepsis, and was transitioned to hospice care and died 50 days after the second dose.

controls. Receiving any immunosuppressive agent other than antimalarials and having a normal anti-dsDNA antibody level prior to vaccination were identified as independent predictors for poor response to the COVID-19 vaccine. Seroreactivity to the SARS–CoV-2 spike RBD strongly correlated with the functional SARS–CoV-2 microneutralization assay and correlated with the ELISpot assay. Overall, there was no change in SLEDAI score pre- and postvaccination, with 11.4% of patients having a flare and 1.3% of those flares being severe, supporting the relative safety of the vaccination in SLE patients.

The finding of anti-dsDNA antibodies positively correlating with higher responses to COVID-19 vaccination was initially unexpected, especially given that this finding persisted even after controlling for medication use. Moreover, disease activity per se was not associated with more effective seroreactivity. It could be hypothesized that the presence of anti-dsDNA antibodies is a proxy of elevated type I IFN activity in these patients. Indeed, studies have shown that high IFNα activity in patients with SLE is associated with the presence of disease-specific autoantibodies, such as anti-dsDNA (18). These autoantibodies can form immune complexes, further stimulating type I IFN production (19). Besides their potent antiviral properties, type I IFNs induce the maturation and activation of myeloid dendritic cells, and promote B cell survival and differentiation into antibody-producing cells (20,21). These considerations support the hypothesis that those with stronger responses to the COVID-19 vaccines could have higher baseline type I IFN activity, due to its potential to enhance antibody responses to foreign antigens. Thus, patients with anti-dsDNA antibodies, despite receiving immunosuppressive therapy, may be more likely to develop a strong humoral response to the COVID-19 vaccines. Alternatively, these analyses did not account for patient adherence to medication or the possibility that elevated dsDNA antibodies reflects inefficacy of immunosuppression, which might account for these findings. These potential insights merit further investigation.

Given the exclusion of patients receiving immunosuppressants from the regulatory vaccine studies, several groups have already explored the influence of immunosuppressive medications on the response to vaccination. Boyarsky et al evaluated patients with organ transplants and reported that antimetabolite maintenance immunosuppression was associated with an absent or reduced anti-RBD spike response after the first dose of the vaccine (22). A follow-up study from the same group in 658 transplant recipients who received the second dose of the SARS–CoV-2 mRNA vaccine showed an increase in seroreactivity in response to the second dose; however, poor responses were associated with antimetabolite immunosuppressive treatment (23).

Concordant with our results, several studies have shown decreased vaccine-induced seroreactivity in patients with rheumatic diseases. In 123 such patients, including 24 with SLE, those receiving MMF or rituximab were less likely to develop an antibody response to the spike protein after the first dose of the SARS–CoV-2 mRNA vaccine; these findings were confirmed in a larger study of 404 patients, including 87 with SLE, after the second dose (24,25). In an analysis of 26 patients with chronic

inflammatory diseases (CIDs) that included 2 patients with SLE who were receiving HCQ, SARS–CoV-2 antibodies were significantly lower in patients, compared to controls, after both doses of BNT162b2 or mRNA-1273. No patients experienced a disease flare after both doses of the vaccine (26). A large study of 133 patients with CIDs, including 15 patients with SLE, who received an mRNA vaccine showed that patients with CIDs had a 3-fold reduction in anti–spike protein IgG response with B cell depletion, glucocorticoids, and antimetabolites (27). A subsequent analysis of 89 patients that included 10 patients with SLE showed that rituximab was associated with impaired serologic response to the SARS–CoV-2 vaccine (28). Haberman et al demonstrated that MTX adversely affected both the humoral and cellular immune responses to COVID-19 mRNA vaccines in patients with immune-mediated inflammatory diseases (29). A large study from Furer et al that included 101 patients with SLE showed that older age and treatment with glucocorticoids, rituximab, MMF, and abatacept were associated with reduced immunogenicity as measured by serum IgG antibody levels against SARS–CoV-2 spike S1/S2 proteins 2–6 weeks after vaccination (30). Our study showed that receiving any non-antimalarial immunosuppressive therapy was independently associated with decreased response to COVID-19 vaccines in patients with SLE.

In addition to concerns regarding inefficient immune responses to COVID vaccination, it may be the case that vaccination induces increased autoantibody production and disease activity. As speculated by Tang et al, delivery of mRNA encoding S protein via the vaccine, likely degraded by normal cellular processes, could interact with a number of cytoplasmic RNA-binding proteins involved in the posttranscriptional regulation of inflammation and result in worsening SLE (5). Similarly, RNA vaccines may trigger Toll-like receptors, generating further production of type I IFN, already well-recognized to be elevated in most SLE patients (19). It has been reported that influenza vaccines triggered a transient increase in several autoantibody specificities in 72 SLE patients, with a flare rate of 19.4% within 6 weeks postvaccination; 10 (13.9%) were mild/moderate and 4 (5.6%) were severe (31). In a study evaluating SLE flares after immunization against poliomyelitis, only 4 of 73 patients (5%) experienced flares (32). In aggregate, despite apprehensions, the data presented herein did not support significantly increased anti-dsDNA antibody production or flares postvaccination. These results are consistent with a recent study which showed that the majority of vaccinated SLE patients had no change or decrease in disease activity after COVID-19 vaccination as measured by the SLEDAI (30).

Our study has several limitations. Similar to other studies evaluating potential surrogate markers for vaccine efficacy, it is premature to assign a threshold level of protection based on either the IgG response to the anti-RBD of SARS–CoV-2 spike protein or the microneutralization assay given the number of controls. There was vaccine hesitancy among patients in the NYU Lupus Cohort, in large part due to concern regarding the potential effect on lupus activity, and thus the patients in this study may not be fully representative of the patients seen in our cohort. While known prior COVID-19 infection was accounted for in all patients, it remains possible that asymptomatic or mild infection occurred between prevaccine blood draw and vaccination, which could influence subsequent seroreactivity. While this study included 90 patients with SLE, the number of patients receiving individual medications was too small to draw any definitive conclusions about their effects on vaccine response in SLE patients, and in our analyses, receiving any non-antimalarial immunosuppressive agent was ultimately the strongest predictor of a poor antibody response to the COVID-19 vaccines. Another limitation of the work is the absence of a direct comparator of SLE flare rates over the same time period. It also remains possible that a perceived SLE flare could have been a vaccine side effect.

This study has several strengths. In contrast to previous reports, the focus was limited to patients with SLE and assessed the COVID-19 vaccines' effects on lupus-specific disease activity with availability of a validated disease index pre- and postvaccination in the majority of patients. Flares were rare, with only 1.3% being severe. These data are reassuring and support the notion that vaccines do not exacerbate disease activity, a finding that should hopefully alleviate vaccine hesitancy. Our study assessed 2 surrogate markers for B cell reactivity and a surrogate for T cell–mediated responses. Although the latter was limited to fewer patients, it was particularly applied to evaluate those with lower humoral responses and reinforced the concern about vaccine efficacy in a subset of these individuals.

In summary, in a multiracial/multiethnic study of SLE patients receiving a complete COVID-19 vaccine regimen, nearly 30% had a low response. Having a normal anti-dsDNA antibody level and taking any immunosuppressive medication other than antimalarials were independently associated with a decreased vaccine response. While minimal protective antibody levels remain unknown, these results, supported by other studies, raise concerns for our lupus patients, many of whom rely on medications to maintain low disease activity. Accordingly, the next phase of scientific inquiry and advance should focus on protocols addressing additional vaccination. Reassuringly, severe disease flares are infrequent, which should encourage patients to consider vaccination.

ACKNOWLEDGMENTS

The authors would like to thank the patients who participated in the study. They would also like to acknowledge Ranit Shriky and Rebecca Cohen for their assistance with regulatory matters and Benjamin Wainwright for his contributions to the manuscript.

AUTHOR CONTRIBUTIONS

All authors were involved in drafting the article or revising it critically for important intellectual content, and all authors approved the final version to be published. Dr. Izmirly had full access to all of the data in the study and takes responsibility for the integrity of the data and the accuracy of the data analysis.

Study conception and design. Izmirly, Kim, Samanovic, Fernandez-Ruiz, Haberman, Scher, Mulligan, Clancy, Buyon.
Acquisition of data. Izmirly, Samanovic, Fernandez-Ruiz, Ohana, Deonaraine, Engel, Masson, Cornelius, Herati, Guttmann, Blank, Plotz, Haj-Ali, Banbury, Stream, Hasan, Ho, Rackoff, Blazer, Tseng, Belmont, Saxena, Mulligan, Clancy, Buyon.
Analysis and interpretation of data. Izmirly, Kim, Samanovic, Fernandez-Ruiz, Xie, Belmont, Saxena, Mulligan, Clancy, Buyon.

REFERENCES

1. Fernandez-Ruiz R, Masson M, Kim MY, Myers B, Haberman RH, Castillo R, et al. Leveraging the United States epicenter to provide insights on COVID-19 in patients with systemic lupus erythematosus. Arthritis Rheumatol 2020;72:1971–80.
2. Fernandez-Ruiz R, Paredes JL, Niewold TB. COVID-19 in patients with systemic lupus erythematosus: lessons learned from the inflammatory disease [review]. Transl Res 2021;232:13–36.
3. Strangfeld A, Schäfer M, Gianfrancesco MA, Lawson-Tovey S, Liew JW, Ljung L, et al. Factors associated with COVID-19-related death in people with rheumatic diseases: results from the COVID-19 Global Rheumatology Alliance physician-reported registry. Ann Rheum Dis 2021;80:930–42.
4. Gianfrancesco M, Hyrich KL, Al-Adely S, Carmona L, Danila MI, Gossec L, et al. Characteristics associated with hospitalisation for COVID-19 in people with rheumatic disease: data from the COVID-19 Global Rheumatology Alliance physician-reported registry. Ann Rheum Dis 2020;79:859–66.
5. Tang W, Askanase AD, Khalili L, Merrill JT. SARS–CoV-2 vaccines in patients with SLE. Lupus Sci Med 2021;8:e000479.
6. Saxena A, Guttmann A, Masson M, Kim MY, Haberman RH, Castillo R, et al. Evaluation of SARS–CoV-2 IgG antibody reactivity in patients with systemic lupus erythematosus: analysis of a multi-racial and multi-ethnic cohort. Lancet Rheumatol 2021;3:e585–94.
7. Polack FP, Thomas SJ, Kitchin N, Absalon J, Gurtman A, Lockhart S, et al. Safety and efficacy of the BNT162b2 mRNA Covid-19 vaccine. New Engl J Med 2020;383:2603–15.
8. Baden LR, El Sahly HM, Essink B, Kotloff K, Frey S, Novak R, et al. Efficacy and safety of the mRNA-1273 SARS–CoV-2 vaccine. New Engl J Med 2020;384:403–16.
9. Sadoff J, Gray G, Vandebosch A, Cárdenas V, Shukarev G, Grinsztejn B, et al. Safety and efficacy of single-dose Ad26.COV2.S vaccine against Covid-19. New Engl J Med 2021;384:2187–201.
10. Boekel L, Hooijberg F, van Kempen ZL, Vogelzang EH, Tas SW, Killestein J, et al. Perspective of patients with autoimmune diseases on COVID-19 vaccination. Lancet Rheumatol 2021;3:e241–3.
11. Hochberg MC. Updating the American College of Rheumatology revised criteria for the classification of systemic lupus erythematosus. Arthritis Rheum 1997;40:1725–34.
12. Petri M, Orbai AM, Alarcón GS, Gordon C, Merrill JT, Fortin PR, et al. Derivation and validation of the Systemic Lupus International Collaborating Clinics classification criteria for systemic lupus erythematosus. Arthritis Rheum 2012;64:2677–86.
13. Aringer M, Costenbader K, Daikh D, Brinks R, Mosca M, Ramsey-Goldman R, et al. 2019 European League Against Rheumatism/American College of Rheumatology classification criteria for systemic lupus erythematosus. Arthritis Rheumatol 2019;71:1400–12.
14. Gladman DD, Ibanez D, Urowitz MB. Systemic lupus erythematosus disease activity index 2000. J Rheumatol 2002;29:288–91.
15. Buyon JP, Petri MA, Kim MY, Kalunian KC, Grossman J, Hahn BH, et al. The effect of combined estrogen and progesterone hormone replacement therapy on disease activity in systemic lupus erythematosus: a randomized trial. Ann Intern Med 2005;142:953–62.
16. Touma Z, Gladman DD, Ibanez D, Urowitz MB. Development and initial validation of the systemic lupus erythematosus disease activity index 2000 responder index 50. J Rheumatol 2011;38:275–84.
17. Curtis JR, Johnson SR, Anthony DD, Arasaratnam RJ, Baden LR, Bass AR, et al. American College of Rheumatology guidance for COVID-19 vaccination in patients with rheumatic and musculoskeletal diseases: version 2. Arthritis Rheumatol 2021;73:e30–45.
18. Niewold TB, Hua J, Lehman TJ, Harley JB, Crow MK. High serum IFN-α activity is a heritable risk factor for systemic lupus erythematosus. Genes Immun 2007;8:492–502.
19. Postal M, Vivaldo JF, Fernandez-Ruiz R, Paredes JL, Appenzeller S, Niewold TB. Type I interferon in the pathogenesis of systemic lupus erythematosus [review]. Curr Opin Immunol 2020;67:87–94.
20. López P, Rodríguez-Carrio J, Caminal-Montero L, Mozo L, Suárez A. A pathogenic IFNα, BLyS and IL-17 axis in systemic lupus erythematosus patients. Sci Rep 2016;6:20651.
21. Psarras A, Emery P, Vital EM. Type I interferon-mediated autoimmune diseases: pathogenesis, diagnosis and targeted therapy [review]. Rheumatology (Oxford) 2017;56:1662–75.
22. Boyarsky BJ, Werbel WA, Avery RK, Tobian AA, Massie AB, Segev DL, et al. Immunogenicity of a single dose of SARS–CoV-2 messenger RNA vaccine in solid organ transplant recipients. JAMA 2021;325:1784–6.
23. Boyarsky BJ, Werbel WA, Avery RK, Tobian AA, Massie AB, Segev DL, et al. Antibody response to 2-Dose SARS–CoV-2 mRNA vaccine series in solid organ transplant recipients. JAMA 2021;21:2204–6.
24. Boyarsky BJ, Ruddy JA, Connolly CM, Ou MT, Werbel WA, Garonzik-Wang JM, et al. Antibody response to a single dose of SARS–CoV-2 mRNA vaccine in patients with rheumatic and musculoskeletal diseases. Ann Rheum Dis 2021. doi: 10.1136/annrheumdis-2021-220289. E-pub ahead of print.
25. Ruddy JA, Connolly CM, Boyarsky BJ, Werbel WA, Christopher-Stine L, Garonzik-Wang J, et al. High antibody response to two-dose SARS–CoV-2 messenger RNA vaccination in patients with rheumatic and musculoskeletal diseases. Ann Rheum Dis 2021. doi: 0.1136/annrheumdis-2021-220656. E-pub ahead of print.
26. Geisen UM, Berner DK, Tran F, Sümbül M, Vullriede L, Ciripoi M, et al. Immunogenicity and safety of anti-SARS–CoV-2 mRNA vaccines in patients with chronic inflammatory conditions and immunosuppressive therapy in a monocentric cohort. Ann Rheum Dis 2021. doi: 10.1136/annrheumdis-2021-220272. E-pub ahead of print.
27. Deepak P, Kim W, Paley MA, Yang M, Carvidi AB, El-Qunni AA, et al. Glucocorticoids and B Cell depleting agents substantially impair immunogenicity of mRNA vaccines to SARS–CoV-2 [preprint]. medRxiv 2021. doi: 10.1101/2021.04.05.21254656. E-pub ahead of print.
28. Spiera R, Jinich S, Jannat-Khah D. Rituximab, but not other antirheumatic therapies, is associated with impaired serological response to SARS- CoV-2 vaccination in patients with rheumatic diseases. Ann Rheum Dis 2021. doi: 10.1136/annrheumdis-2021-220604. E-pub ahead of print.
29. Haberman RH, Herati R, Simon D, Samanovic M, Blank RB, Tuen M, et al. Methotrexate hampers immunogenicity to BNT162b2 mRNA COVID-19 vaccine in immune-mediated inflammatory disease. Ann Rheum Dis 2021. doi: 10.1101/2021.05.11.21256917. E-pub ahead of print.
30. Furer V, Eviatar T, Zisman D, Peleg H, Paran D, Levartovsky D, et al. Immunogenicity and safety of the BNT162b2 mRNA COVID-19 vaccine in adult patients with autoimmune inflammatory rheumatic

diseases and in the general population: a multicentre study. Ann Rheum Dis 2021. doi: 10.1136/annrheumdis-2021-220647. E-pub ahead of print.

31. Crowe SR, Merrill JT, Vista ES, Dedeke AB, Thompson DM, Stewart S, et al. Influenza vaccination responses in human systemic lupus erythematosus: impact of clinical and demographic features. Arthritis Rheum 2011;63:2396–406.
32. Schattner A, Ben-Chetrit E, Schmilovitz H. Poliovaccines and the course of systemic lupus erythematosus—a retrospective study of 73 patients. Vaccine 1992;10:98–100.

Cancer Communications

ORIGINAL ARTICLE Open Access

DDIT4 promotes gastric cancer proliferation and tumorigenesis through the p53 and MAPK pathways

Feng Du†, Lina Sun†, Yi Chu†, Tingyu Li, Chao Lei, Xin Wang, Mingzuo Jiang, Yali Min, Yuanyuan Lu*, Xiaodi Zhao*, Yongzhan Nie and Daiming Fan*

Abstract

Background: Gastric cancer (GC) is one of the most common malignancies worldwide, particularly in China. DNA damage-inducible transcript 4 (DDIT4) is a mammalian target of rapamycin inhibitor and is induced by various cellular stresses; however, its critical role in GC remains poorly understood. The present study aimed to investigate the potential relationship and the underlying mechanism between DDIT4 and GC development.

Methods: We used western blotting, real-time polymerase chain reaction, and immunohistochemical or immunofluorescence to determine DDIT4 expression in GC cells and tissues. High-content screening, cell counting kit-8 assays, colony formation, and in vivo tumorigenesis assays were performed to evaluate cell proliferation. Flow cytometry was used to investigate cell apoptosis and cell cycle distribution.

Results: DDIT4 was upregulated in GC cells and tissue. Furthermore, downregulating DDIT4 in GC cells inhibited proliferation both in vitro and in vivo and increased 5-fluorouracil-induced apoptosis and cell cycle arrest. In contrast, ectopic expression of DDIT4 in normal gastric epithelial cells promoted proliferation and attenuated chemosensitivity. Further analysis indicated that the mitogen-activated protein kinase and p53 signaling pathways were involved in the suppression of proliferation, and increased chemosensitivity upon DDIT4 downregulation.

Conclusion: DDIT4 promotes GC proliferation and tumorigenesis, providing new insights into the role of DDIT4 in the tumorigenesis of human GC.

Keywords: DNA damage-inducible transcript 4, Gastric cancer, Proliferation, Mitogen-activated protein kinase, p53

Background

Gastric cancer (GC) is one of the most common malignancies worldwide and remains the second leading cause of cancer-related death in China [1]. Despite the declining incidence of GC, the 5-year overall survival rate remains low at less than 30% [2]. Two of the major causes of the poor prognosis of GC are metastasis and multiple drug resistance, which greatly hamper the success of treatment modalities [1]. Genetic alterations are generally considered to drive cancer development and progression, and emerging evidence indicates that the complex molecular heterogeneity of GC underlies most, if not all, of the general ineffectiveness of current chemotherapeutics for GC [3]. Hence, improvements in the treatment of GC must be developed from a better understanding of its elaborate regulatory network because the underlying molecular mechanisms of GC tumorigenesis remain unclear.

DNA damage-inducible transcript 4 (DDIT4), also known as DNA damage response 1 (REDD1) and stress-triggered protein (RTP801), is induced by a variety of stress conditions, including oxidative stress, endoplasmic reticulum stress, hypoxia, and starvation [4]. DDIT4 protein inhibits mammalian target of rapamycin complex 1

*Correspondence: luyuandreamer@aliyun.com; leedyzhao@fmmu.edu.cn; daimingfan@fmmu.edu.cn
†Feng Du, Lina Sun and Yi Chu contributed equally to this work
State Key Laboratory of Cancer Biology, National Clinical Research Center for Digestive Diseases and Xijing Hospital of Digestive Diseases, Fourth Military Medical University, 127 Chang Le West Road, Xi'an 710032, China

(mTORC1) by stabilizing the tuberous sclerosis complex (TSC1–TSC2) [5]. Over the past decades, DDIT4 dysregulation has been observed in numerous human malignancies. In prostate cancer (PC) cells, DDIT4 enhances CCAAT/enhancer-binding protein beta (C/EBPbeta)-mediated autophagosome-lysosome fusion and desensitizes the cells to bortezomib [6]. Additionally, baicalein upregulates DDIT4 and inhibits mTORC1 and the proliferation of platinum-resistant cancer cells, indicating that DDIT4 expression has potential as a chemotherapeutic and chemoprevention agent [7]. Although mammalian target of rapamycin (mTOR) pathway inhibition is a current strategy for the treatment of cancer [8, 9], paradoxically, several in vitro and in vivo studies indicate that DDIT4 has a protective role against apoptosis [10–12]; *DDIT4* knockdown increases dexamethasone-induced cell death in murine lymphocytes [10]. Additionally, DDIT4 expression was significantly increased in serous adenocarcinoma compared with other histological types, and this increase was positively associated with ascites formation and late-stage disease in ovarian cancer (OC) [11]. A recent in silico evaluation of the online datasets Kaplan–Meier plotter and SurvExpress indicated that high DDIT4 levels were significantly associated with a worse prognosis in acute myeloid leukemia, glioblastoma multiforme, and breast, colon, skin and lung cancer [12]. However, in GC, the second most common type of cancer in Asia in terms of incidence and cancer mortality, the clinical significance and biological role of DDIT4 remain to be elucidated.

In the present study, we examined DDIT4 expression levels in GC tissue samples and cell lines, and investigated the role of DDIT4 and the mechanism by which it is dysregulated in gastric cancer.

Methods

Cell culture and tissue collection

The human GC cell lines SGC7901, BGC823, MKN45, and AGS, and the immortalized gastric epithelial cell line GES were purchased from the Cell Resource Center of the Chinese Academy of Sciences, Shanghai, China. Cells were maintained in Dulbecco's Modified Eagle's Medium (Thermo Scientific HyClone, Beijing, China) supplemented with 10% fetal bovine serum (HyClone), 100 U/mL penicillin, and 100 U/mL streptomycin (HyClone) in a 37 °C humidified incubator with a mixture of 95% air and 5% CO_2.

A total of 20 fresh primary GC samples and matched adjacent non-cancerous tissues were obtained from patients undergoing surgery at Xijing Hospital, Xi'an, China. All samples were confirmed by the Department of Pathology at Xijing Hospital and stored in a liquid nitrogen canister. All patients provided informed consent for excess specimens to be used for research purposes and all protocols employed in the present study were approved by the Medical Ethics Committee of Xijing Hospital.

Mice

Female BALB/c nude mice were provided by the Experimental Animal Center of the Fourth Military Medical University and were housed in pathogen-free conditions. All animal studies complied with the Fourth Military Medical University animal use guidelines, and the protocol was approved by the Fourth Military Medical University Animal Care Committee.

Reagent and inhibitor

5-Fluorouracil was purchased from Sigma (Sigma-Aldrich Corporation, Los Angeles, CA, USA), and MAPK/ERK inhibitor (PD98059) and p53 inhibitor (A15201) were purchased from Invitrogen (Thermo Fisher Scientific, Cambridge, Massachusetts, USA); all were stored according to the manufacturer's instructions.

RNA extraction and real-time polymerase chain reaction (PCR)

Total RNA was extracted from cell lines using the RNeasy Plus Universal Tissue Mini Kit (Qiagen, Hilden, Germany) according to the manufacturer's instructions. The PCR primers for *DDIT4* and *ACTB* were synthesized by TaKaRa (Dalian, China). The sequences were as follows: *DDIT4*, 5′-GGACCAAGTGTGTTTGTTGTTTG-3′ (Forward) and 5′-CACCCACCCCTT CCTACTCTT-3′ (Reverse); *ACTB*, 5′-TCATGAAGTGTGACGTTGACA TCCGT- 3′ (Forward) and 5′-CCTAGAAGCATTTGC GGTGCACGATG-3′ (Reverse). cDNA was synthesized using the PrimeScript RT Reagent Kit (TaKaRa, Dalian, China). Real-time PCR was performed using SYBR Premix Ex Taq II (TaKaRa). Fluorescence was measured using a LightCycler 480 system (Roche, Basel, Switzerland). *ACTB* was used as an internal control for mRNA analysis. Each sample was run in triplicate.

Protein extraction and western blotting

Total proteins were prepared from fresh frozen tissue or cultured cells in radio immunoprecipitation assay (RIPA) lysis and extraction buffer (Beyotime Biotechnology, Shanghai, China) with protease and phosphatase inhibitors. Denatured proteins (20–50 mg) were separated by sodium dodecyl sulfate–polyacrylamide gel electrophoresis and transferred to polyvinylidene difluoride membranes. The following primary antibodies were used according to the manufacturer's instructions: anti-DDIT4 (Dilution 1:500, Abcam, Cambridge, MA, USA) and anti-β-actin (Dilution 1:2000), anti-Ki67 (Dilution 1:1000), anti-p53 (Dilution 1:1000), anti-p-p53 (p-Ser6) (Dilution

1:1000), anti-p-p53 (p-Ser315) (Dilution 1:1000), anti-$p21^{Cip1}$ (Dilution 1:500), anti-p-$p21^{Cip1}$ (p-Thr145) (Dilution 1:500), anti-MEK1 (Dilution 1:1000), anti-p-MEK1 (p-Ser221) (Dilution 1:1000), anti-p42/44MAPK (Dilution 1:1000), and anti-p-p42/44MAPK (p-Thr202 and p-Tyr204) (Dilution 1:1000) (Cell Signaling Technology, Beverly, MA, USA). Densitometry of specific blotted bands was analyzed by ImageJ 1.48 software (Image-Processing and Analysis in Java; National Institutes of Health, Bethesda, MD, USA; http://imagej.nih.gov/), and the intensity values were normalized against the β-actin loading control.

Tissue microarray immunohistochemistry

GC tissue microarrays were purchased from Superchip (Shanghai, China). Each array contained 90 cases of paired adjacent gastric tissues and primary GC tissues. Immunohistochemical (IHC) staining was performed using anti-DDIT4 and anti-Ki67 antibodies as per the manufacturer's instructions. IHC results were scored independently by two pathologists in a blinded manner. The scoring was based on the intensity and extent of staining. Staining intensity was graded as follows: 0, negative staining; 1, weak staining; 2, moderate staining; and 3, strong staining. The proportion of stained cells per specimen was determined semi-quantitatively as follows: 0, <1%; 1, 1–25%; 2, 26–50%; 3, 51–75%; and 4, >75%. The histological score (H-score) for each specimen was computed using the following formula: H-score = proportion score × intensity score. The samples were further characterized by H-score as negative (−, score: 0), weak (+, score: 1–4), moderate (++, score: 5–8), and strong (+++, score: 9–12). Samples with an H-score of >4 were considered to exhibit high expression, and samples with an H-score of ≤4 were considered to exhibit low expression.

Immunofluorescence staining

Cells were plated onto glass coverslips, fixed with 4% paraformaldehyde for 20 min and permeabilized with 0.1% Triton X-100 in PBS for 15 min. Blocking solution was applied at room temperature for 1 h. Rabbit anti-human DDIT4 primary antibody (Abcam) was applied at 4 °C overnight. FITC-conjugated goat anti-rabbit and Cy3-conjugated goat anti-mouse secondary antibodies were incubated on the coverslips at room temperature for 2 h. Immunostaining signals and DAPI-stained nuclei were visualized at room temperature using a confocal microscope (FV10i; Olympus, Tokyo, Japan) equipped with a 10×/0.30 numerical aperture objective lens (Olympus) and Fluoview software (version 4.3; Olympus). No imaging medium was used. For better visualization, the images were adjusted using the level and brightness/contrast tools in Photoshop according to the guidelines for the presentation of digital data.

Lentivirus infection

DDIT4-overexpression or sh-DDIT4 lentivirus infection was conducted by GeneChem (Shanghai, China). Target cells (1×10^5) were infected with 1×10^7 lentivirus-transducing units in the presence of 5 mg/mL polybrene. An empty lentiviral vector was used as a negative control. After transfection and antibiotic selection for 6 weeks, cells were collected for further investigation.

High-content screening assay

Cells transfected with lentivirus stably expressing green fluorescent protein (GFP) were seeded into 96-well plates and treated with increasing doses of 5-FU (0, 10, 20 μg/mL for GC cells or 0, 2, 4 μg/mL for GES cells). Cells were imaged every 4 h for 48 h using the Thermo Scientific CellInsight CX7 High Content Analysis Platform (0, 10, 20 μg/mL for GC cells or 0, 2, 4 μg/mL for GES cells; Thermo Fisher Scientific, Cambridge, Massachusetts, USA). Proliferation curves were plotted and analyzed using HCS Studio Software (Thermo Fisher Scientific).

Colony formation assays

Transfected cells were seeded in six-well plates (1000 cells/well). After 14–18 days of incubation to establish stable clones, cells were fixed with 70% ethanol and stained with crystal violet solution. Colonies containing greater than 50 cells were counted. The experiment was conducted with three independent triplicates.

Cell cycle and apoptosis assays

For cell cycle analysis, target cells were selected with antibiotics (penicillin–streptomycin solution) for 48 h after transfection as indicated, fixed in 75% ethanol, and stained with propidium iodide supplemented with RNase A (Roche, Mannheim, Germany) for 30 min at 22 °C. The Annexin V-FITC Apoptosis Detection Kit (Cell Signaling Technology, Beverly, MA, USA) was used for apoptosis assays. Cells (1×10^4) were stained according to the manufacturer's protocol and sorted using a fluorescence-activated cell sorting sorter (BD Biosciences, La Jolla, CA, USA). Data were analyzed using ModFit software (BD Biosciences).

In vivo tumorigenicity

BGC823 cells (5×10^5 cells in 0.2 mL of PBS) transfected with pCMV-DDIT4 or empty pCMV were injected subcutaneously into the dorsal flank of 5-week-old female Balb/c nude mice (five mice per group). Tumor diameter was measured every 3 days for 30 days. Tumor volume (mm^3) was calculated based on the longest and

shortest diameters as follows: volume = (shortest diameter)^2 × (longest diameter) × 0.5. Thirty days after injection, all mice were killed, and the tumor xenografts were isolated for further analysis. All experimental animals were supplied by the Experimental Animal Center of the Fourth Military Medical University. All protocols for animal studies were approved by the Fourth Military Medical University Animal Care Committee.

Cell counting kit-8 (CCK8) assay

For cell counting kit 8 assays, cells were seeded into 96-well plates at a density of 1000 cells in 100 μL of complete culture medium per well. At the indicated time points, the medium was replaced with a kit solution (TransDetect cell counting kit, Transgene, Beijing, China) and complete culture medium at a ratio of 1:9, and the samples were incubated for 2 h at 37 °C. The absorbance of each sample was analyzed at 450 nm using a microtiter plate reader (Tecan, Switzerland). The assay was repeated in triplicate.

Phospho-specific protein microarray analysis

Phospho-array detection was performed in cooperation with Wayen Biotechnology (Shanghai, China). At 48 h post-transfection, all treated cells were collected for protein extraction. Protein samples of 50 mg each were tagged with biotin reagent and hybridized on a Phosphorylation ProArray (Full Moon BioSystems, USA) using an Antibody Array Kit (FullMoon BioSystems, USA) for the detection of 248 site-specific cancer signaling phospho-antibody profiles. Finally, fluorescence intensity was scanned by GenePix 4000B (Axon Instruments, Houston, USA) using GenePix Pro 6.0. The raw data were manipulated using Grubbs' method. The phosphorylation ratio was calculated as follows: phosphorylation ratio ¼ phospho value/unphospho value.

Statistical analyses

SPSS software (version 19.0, SPSS Inc., Chicago, IL, USA) was used for statistical analyses. Continuous data are presented as the mean ± standard deviation (SD), and Student's unpaired *t*-test was utilized for comparisons between two groups. Frequencies of categorical variables were compared using the χ^2 test. A *P* value of less than 0.05 was considered significant.

Results

DDIT4 was upregulated in GC tissues

To determine the expression pattern of DDIT4 in GC, we measured DDIT4 expression in 20 pairs of GC and adjacent normal tissue specimens using real-time PCR and western blotting. DDIT4 expression was upregulated in 13 of 20 GC tissues compared with matched adjacent normal tissues (Fig. 1a). Similar to *DDIT4* mRNA levels, DDIT4 protein levels were increased in GC samples compared with their normal counterparts (Fig. 1b). Furthermore, we performed IHC using a GC tissue microarray containing 90 pairs of primary GC tissues and paired adjacent normal tissues. The IHC analysis revealed clear elevation of DDIT4 levels in GC tissues compared with the corresponding normal tissues, and DDIT4 expression was primarily located in the cytoplasm (Fig. 1c, d). Univariate survival analysis demonstrated that tumor size ($P = 0.013$), invasion depth ($P = 0.015$), lymphatic metastasis ($P = 0.018$), distant metastasis ($P < 0.001$), AJCC stage ($P < 0.001$), and pathological grade ($P < 0.001$) exhibit statistically significant associations with GC patient survival (Table 1). Taken together, DDIT4 expression was increased in GC tissues.

Increased DDIT4 in GC cells promotes proliferation and colony formation

To validate the expression pattern of DDIT4, we detected DDIT4 protein and mRNA levels in four GC cell lines (MKN45, AGS, SGC7901, and BGC823) and an immortalized gastric epithelial cell line, GES. Similar to the GC tissues, DDIT4 levels were significantly increased at both the protein and mRNA level in GC cells compared with GES cells (Fig. 2a, b). Moreover, immunofluorescence revealed that DDIT4 was mainly localized to the cytoplasm (Fig. 2c). To analyze biological function, we silenced *DDIT4* in SGC7901 and BGC823 cells with a lentiviral vector and upregulated *DDIT4* levels in GES cells using a *DDIT4*-overexpressing lentiviral vector. After cell transfection and antibiotic screening for 6 weeks, the lentiviral transfection efficiency was confirmed by real-time PCR and western blotting. Among three shDDIT4 vectors, shDDIT4-2 was the most effective at silencing *DDIT4* in SGC7901 and BGC823 cells (Fig. 2d, e). In contrast, transfection of the *DDIT4*-overexpressing lentiviral vector significantly upregulated DDIT4 levels in GES cells (Fig. 2f). Therefore, shDDIT4-2 and the *DDIT4*-overexpressing lentiviral vector were employed in the subsequent experiments.

Given that DDIT4 has been implicated in oncogene- and stress-induced DNA damage [4], we hypothesized that DDIT4 upregulation might be involved in the initiation and development of GC. To test this hypothesis, we conducted high-content screening assays and colony formation assays to determine whether DDIT4 regulates GC cell proliferation. The high-content screening assays revealed that cell proliferation was significantly inhibited by *DDIT4* silencing in SGC7901 cells compared with the lentiviral control (Fig. 3a). Given that chemotherapeutics cause cytotoxic effects and DNA damage, we assessed whether DDIT4 was involved in the response of GC cells to these agents.

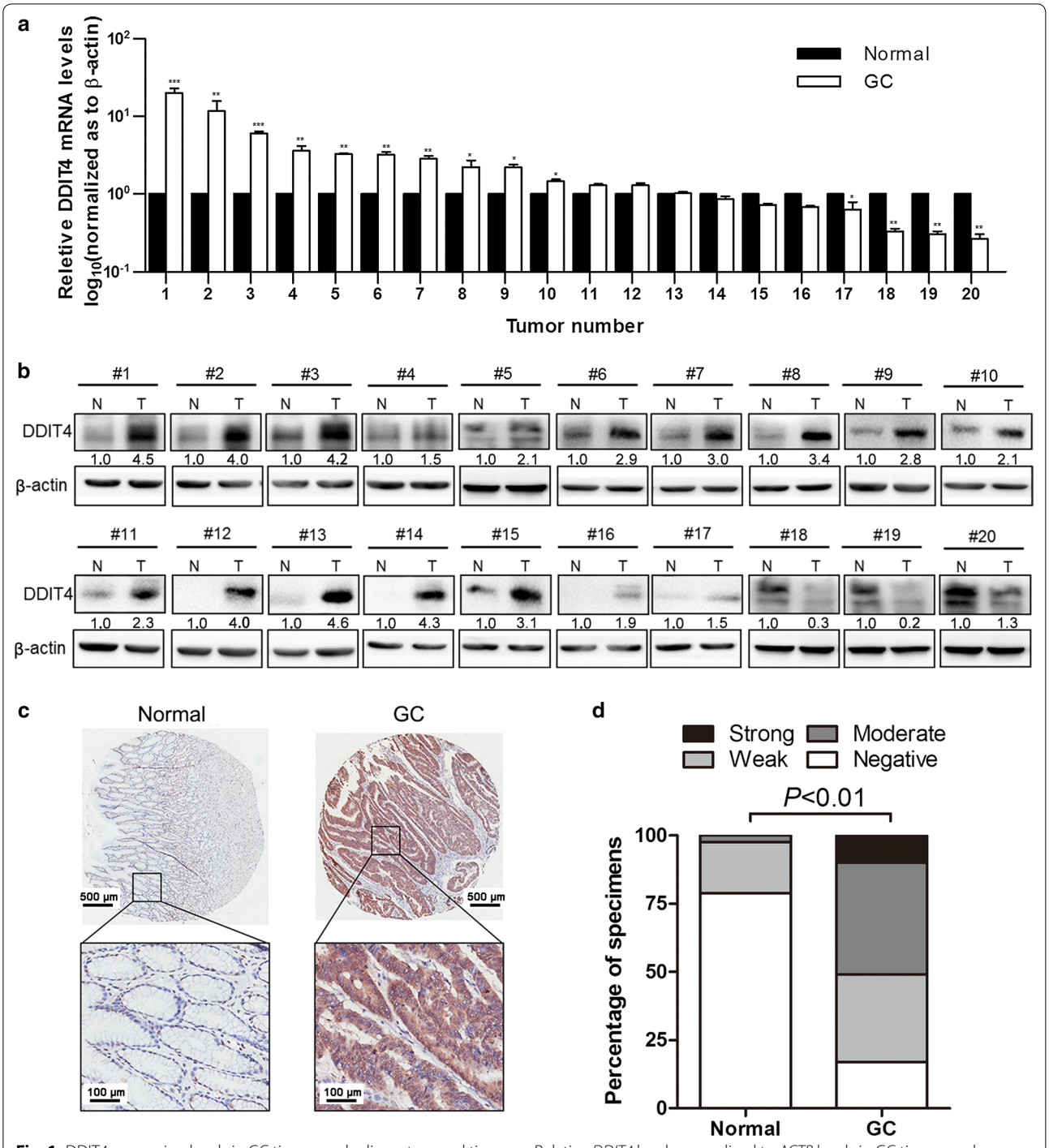

Fig. 1 DDIT4 expression levels in GC tissues and adjacent normal tissues. **a** Relative *DDIT4* levels normalized to *ACTB* levels in GC tissues and adjacent normal tissues were detected by real-time polymerase chain reaction (PCR). **b** DDIT4 expression in GC tissues and paired normal tissues was determined by western blotting. **c**, **d** Immunohistochemistry revealed DDIT4 upregulation in GC tissues compared with normal tissues. *DDIT4* DNA damage-inducible transcript 4, *GC* gastric cancer, *N* normal tissue, *T* tumor tissue. ***$P < 0.001$, **$P < 0.01$, *$P < 0.05$

Thus, we monitored SGC7901 cell proliferation after treatment with 5-FU (10 or 20 μg/mL) and found that *DDIT4* downregulation suppressed proliferation in the presence of 5-FU (Fig. 3b, c). Consistently, colony formation assays revealed that *DDIT4* downregulation inhibited SGC7901 colony formation with or without 5-FU (Fig. 3d). Similar

Table 1 Univariate and multivariate survival analysis of 90 GC patients

Variable	Univariate log rank survival analysis			Multivariate Cox survival analysis		
	RR	95% CI	*P* value	RR	95% CI	*P* value
Age (years)						
< 60	1.000					
≥ 60	1.085	0.832–1.413	0.547			
Gender						
Male	1.000					
Female	1.091	0.797–1.494	0.588			
Tumor size (cm)						
< 5	1.000					
≥ 5	1.182	1.036–1.349	0.013	1.387	0.827–2.325	0.215
Invasion depth						
T1/2	1.000					
T3/4	1.610	1.098–2.360	0.015	1.496	0.696–3.216	0.302
Lymphatic metastasis						
N0	1.000					
N1–3	1.369	1.056–1.774	0.018	1.093	0.456–2.621	0.842
Distant metastasis						
M0	1.000					
M1	1.468	1.268–1.299	< 0.001	4.364	1.830–10.409	0.001
AJCC stage						
I/II	1.000					
III/IV	1.500	1.214–1.853	< 0.001	1.755	0.768–4.011	0.183
Pathological grade						
I/II	1.000					
III/IV	1.912	1.125–3.250	0.017	2.077	0.863–4.996	0.103
DDIT4 expression						
Low	1.000					
High	3.583	2.345–4.271	0.146			

RR risk ratio, *95% CI* 95% confidence interval, *AJCC* American Joint Committee on Cancer

to SGC7901 cells, *DDIT4* downregulation in BGC823 cells reduced cell proliferation (Fig. 3e–g) and increased sensitivity to 5-FU (Fig. 3h). In contrast, ectopic expression of *DDIT4* promoted GES cell proliferation and colony formation (Fig. 3i, l) and attenuated the sensitivity of GES cells to 5-FU (Fig. 3j–l). In addition, we performed Transwell assays to determine whether DDIT4 regulates GC cell migration and invasion, but no significant difference was observed in cells transfected with shDDIT4 lentivirus compared with the control group (Additional file 1: Figure S1). Taken together, these observations indicated that *DDIT4* acts as an oncogene that promotes GC cell proliferation and reduces chemosensitivity.

Downregulation of *DDIT4* increases 5-FU-induced apoptosis but decreases 5-FU-induced S phase arrest in GC cells

Beneath the complexity and idiopathy of cancer lies a limited number of critical events that propel the tumor cell and its progeny into uncontrolled expansion and invasion [13]. Two such events are deregulation of apoptosis and the cell cycle, which together with the obligatory compensatory dysregulation of proliferation provide a minimal "platform" necessary to support further neoplastic progression [13]. Thus, we performed flow cytometry to determine whether DDIT4 modulates apoptosis and the cell cycle, which contribute to gastric carcinogenesis. *DDIT4* downregulation promoted apoptosis of SGC7901 cells treated with 0, 10 or 20 μg/mL 5-FU compared with the negative controls (Fig. 3m). In addition, *DDIT4* silencing in SGC7901 cells attenuated gastric cancer cell S phase arrest (Fig. 3n). Similarly, in BGC823 cells, *DDIT4* downregulation significantly increased GC cell apoptosis and reduced S phase arrest compared with the control (Fig. 3m, n). In contrast, *DDIT4* overexpression in GES cells significantly reduced apoptosis in the absence and presence of 5-FU (10 or 20 μg/mL) (Fig. 3m). Moreover, as demonstrated by cell cycle analysis, ectopic

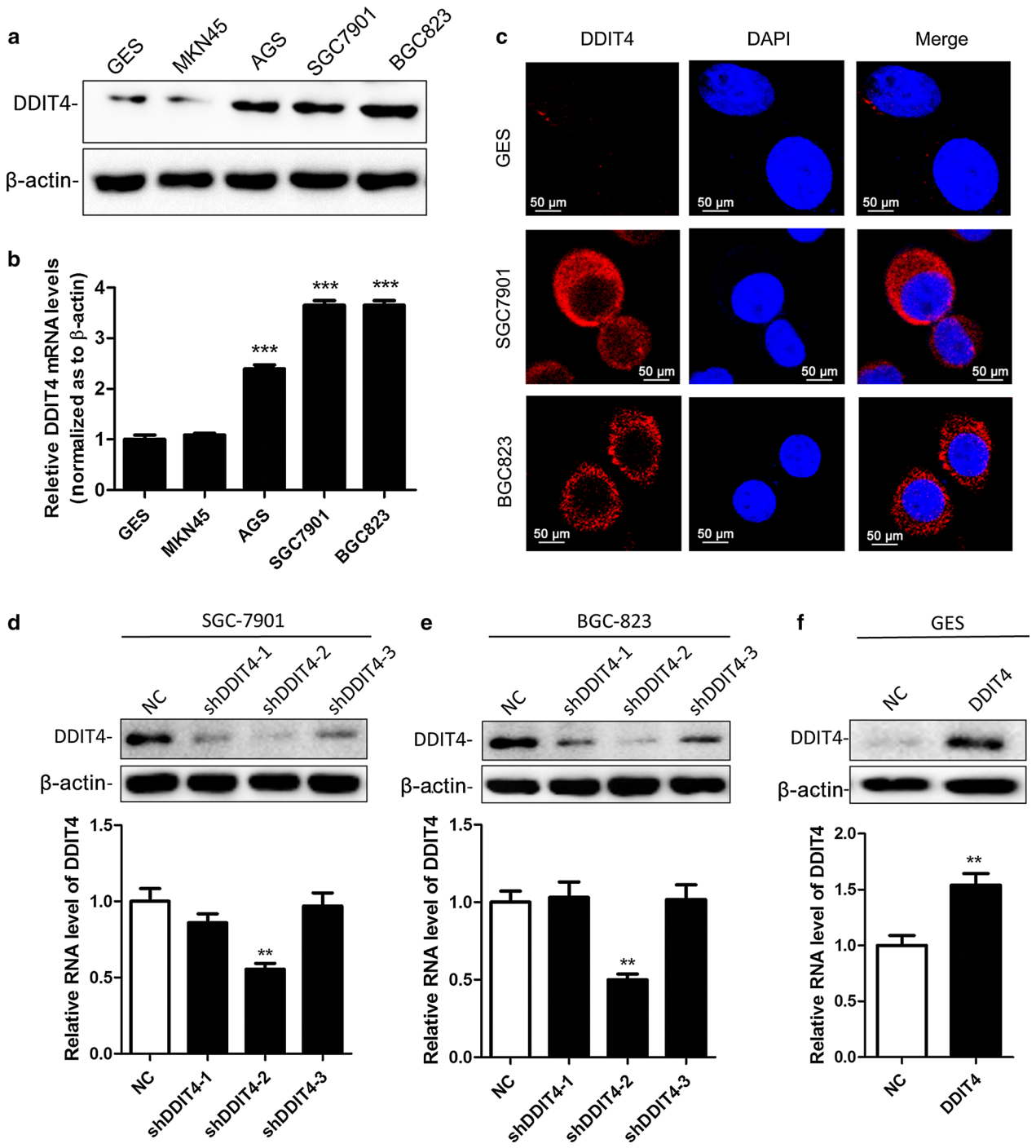

Fig. 2 DDIT4 expression in GC cell lines. **a**, **b** DDIT4 protein and mRNA expression in the normal gastric cell line GES and in the GC cell lines MKN45, AGS, SGC7901, and BGC823. **c** The expression and subcellular localization of DDIT4 in GES, SGC7901, and BGC823 cells were examined by immunofluorescence. **d**, **e** Western blot and qRT-PCR analysis of DDIT4 expression in *DDIT4*-depleted SGC7901 and BGC823 cells. **f** Western blot and qRT-PCR analysis of DDIT4 expression in *DDIT4*-overexpressing GES cells. ***$P < 0.001$, **$P < 0.01$, *$P < 0.05$

expression of *DDIT4* in GES cells drove the cell cycle into S phase and G_2/M phase and reduced the population of cells in G_1 phase compared with the control (Fig. 3n). Taken together, these findings indicated that DDIT4 is associated with 5-FU-induced apoptosis and cell cycle progression in GC cells in a dose-dependent manner.

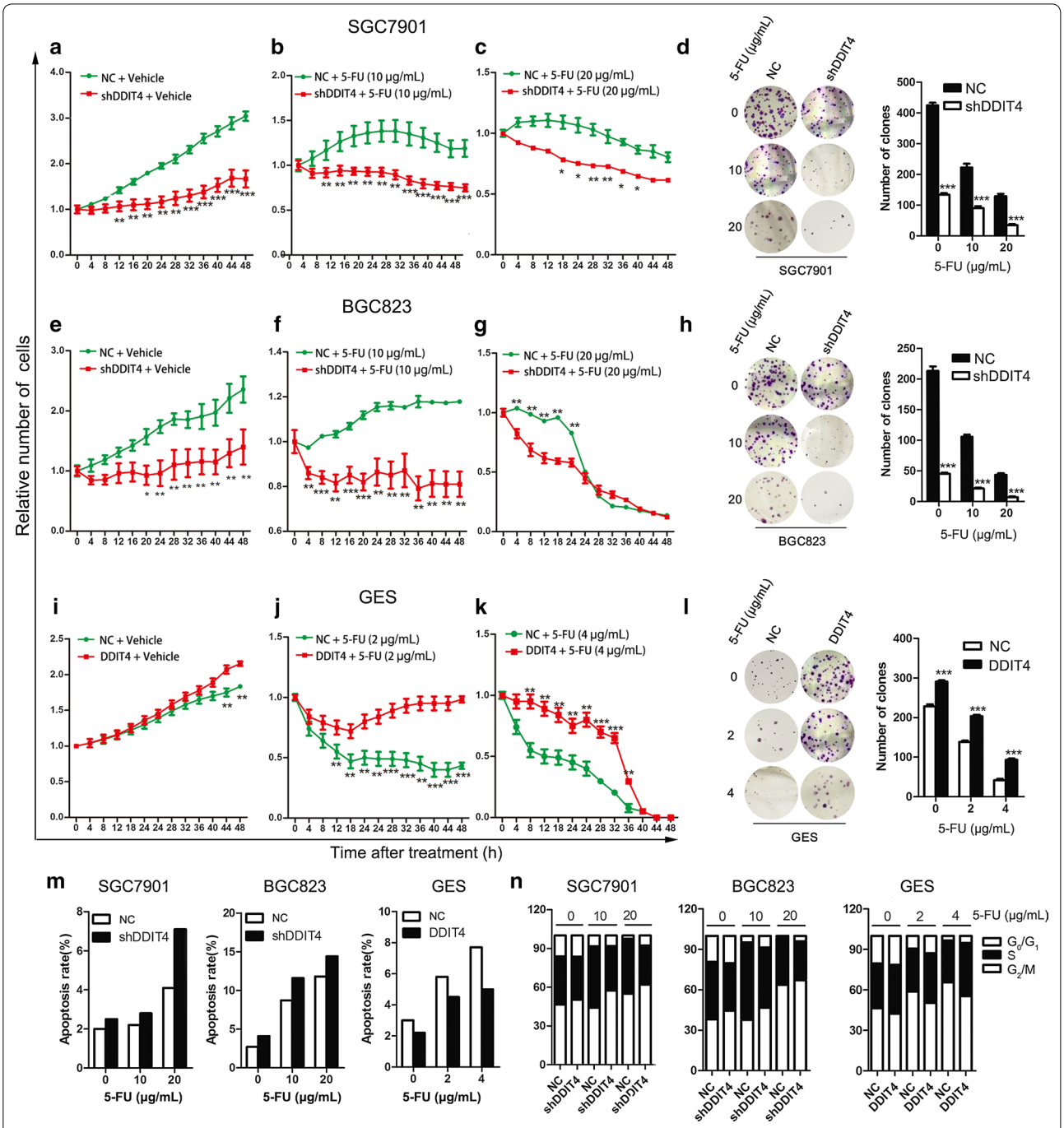

Fig. 3 Effect of *DDIT4* silencing and overexpression on GC cell proliferation, apoptosis and cell cycle progression in vitro. **a**–**c** SGC7901 cell proliferation rate in response to 0, 10, and 20 μg/mL 5-FU was determined by high-content proliferation assays at various time points. **d** Representative images of SGC7901 cell colony formation after treatment with 0, 10, or 20 μg/mL 5-FU. The number of colonies was calculated, and the results are depicted in the bar chart. **e**–**g** BGC823 cell proliferation rate. **h** BGC823 cell colony formation assay. **i**–**k** GES cell proliferation rate. **l** GES cell colony formation assay. **m** Apoptosis in SGC7901, BGC823, and GES cells in response to 0, 10, or 20 μg/mL 5-FU as determined by flow cytometry. **n** Cell cycle distribution of SGC7901, BGC823, and GES cells treated with 0, 10, or 20 μg/mL 5-FU. ***$P < 0.001$, **$P < 0.01$, *$P < 0.05$

DDIT4 silencing inhibits GC cell tumorigenesis in vivo

To investigate the effect of DDIT4 on GC tumorigenic behavior in vivo, we conducted tumorigenicity assays in nude mice by subcutaneously injecting BGC823 cells stably expressing shDDIT4 or scrambled control shRNA into the dorsal flank of several mice. *DDIT4* depletion

resulted in a significant reduction in tumor growth (Fig. 4a). *DDIT4*-knockdown tumors grew significantly slower (Fig. 4b) and weighed significantly less on average (Fig. 4c, d) compared with control tumors. Furthermore, we used western blotting and IHC to detect DDIT4 expression in xenografts and validated the lower DDIT4 levels in *DDIT4*-knockdown tumors compared with control tumors (Fig. 4e, f). Finally, we observed a reduced Ki67 (proliferation marker)-positivity rate in tumor tissues in the *DDIT4*-knockdown group compared with the control group (Fig. 4f). Taken together, these observations indicated that DDIT4 promotes GC growth in vivo and might function as an oncogene in gastric carcinogenesis.

DDIT4 downregulation inhibits GC cell proliferation through the MAPK and p53 pathways

To understand the molecular mechanism underlying GC growth regulation by DDIT4, we utilized phospho-array assays that detect 131 phosphorylation sites in 12 critical cancer signaling molecules (Additional file 2: Table S1). Given that DDIT4 acts as a negative regulator of mTOR, we first examined the activity of the phosphatidylinositol-4,5-bisphosphate 3-kinase (PI3K)/AKTkt/mTOR pathway in GC cells upon *DDIT4* downregulation. Phospho-array assays revealed that the PI3K/AKT/mTOR pathway did not exhibit significant changes in *DDIT4*-knockdown cells (data not shown). Western blotting assays confirmed this observation (Fig. 5a), indicating that DDIT4 might activate other signaling pathways in GC cells. To uncover the molecular mechanism underlying GC growth regulation by DDIT4, we assessed MAPK and p53 signaling pathways in *DDIT4*-downregulated GC cells. In contrast to the PI3K/AKT/mTOR pathway, obvious alterations in the MAPK and p53 signaling pathways were observed (Fig. 5b). Anti-apoptotic BCL-2 levels were reduced, whereas pro-apoptotic BAD and proliferation-suppressive $p21^{Cip1}$ levels were increased in *DDIT4*-downregulated cells (Fig. 5b). To further examine the effect of blocking the MAPK and p53 signaling pathways on gastric cancer cell proliferation following *DDIT4* knockdown, we performed rescue experiments by blocking the MAPK and p53 signaling pathways using a MAPK/ERK inhibitor (PD98059) and a p53 inhibitor (A15201) in *DDIT4*-knockdown cells. MAPK and p53 inhibition abolished the BCL-2 suppression and $p21^{Cip1}$ elevation that was induced by *DDIT4* downregulation (Fig. 5c). Consistent with western blot assays, the CCK8 assays indicated that MAPK and p53 inhibition restored GC cell proliferation, which was suppressed by *DDIT4* knockdown (Fig. 5d). Taken together, these findings indicated that the MAPK and p53 signaling pathways might play a critical role in DDIT4-mediated GC cell proliferation.

Discussion

Our study suggests that DDIT4 is an important regulator that is markedly upregulated in GC tissues and cells, and that knockdown of *DDIT4* suppresses the proliferation and tumorigenicity of GC cells both in vitro and in vivo. In addition, DDIT4 is attributed to chemotherapy-induced apoptosis and S phase arrest in GC cells. Mechanically, the proliferation-suppressive and chemosensitive effect of DDIT4 downregulation might be associated with activation of the p53 and MAPK signaling pathways.

GC currently poses a tremendous health burden on communities worldwide and is thought to result from a combined attack of environmental factors and genetic alterations [14, 15]. Among these factors, oncogene activation triggers replication stress and DNA damage, thereby increasing genome instability [16]. Additionally, the transient and long-term lack of nutrients, oxygen, and growth factors causes GC cells to be subject to frequent metabolic stress [17]. Thus, most GC cells display oncogene- or adverse environment-induced DNA damage [18]. DDIT4, a DNA damage-inducible transcript, is transcriptionally upregulated in multiple settings of DNA damage [4]. Notably, recent studies highlighted the important roles of DDIT4 in various types of human cancer [6, 19, 20]. In breast cancer, DDIT4 acts as a tumor-suppressor to regulate miR-495-mediated oncogenesis and hypoxia resistance [19]. Friedman et al. reported that DDIT4 enhances C/EBPbeta mediated autophagosome-lysosome fusion and desensitized PC cells to bortezomib [6]. In contrast, a positive correlation between DDIT4 and p-AKT was identified in ovarian cancer (OC), and DDIT4 expression in OC tissues was significantly increased in patients with serous adenocarcinoma and late FIGO stage [11], indicating that DDIT4 might be a tumor promotor in OC. These above findings demonstrated context-dependent regulation of DDIT4 in tumorigenesis and progression. However, whether and how DDIT4 plays critical roles in GC, which is characterized by frequent DNA damage, remains largely unknown. In the present study, we detected DDIT4 expression in GC tissues and cell lines, and found that DDIT4 was significantly upregulated in GC tissues and cell lines. In subsequent loss- and gain-of-function analyses, we observed that overexpression of *DDIT4* promoted GES cell proliferation, whereas knockdown of *DDIT4* suppressed GC cell proliferation both in vitro and in vivo. Therefore, our results demonstrated that DDIT4 is a proliferation-promoting and oncogenic protein in GC cells. Moreover, several lines of evidence demonstrate that DDIT4

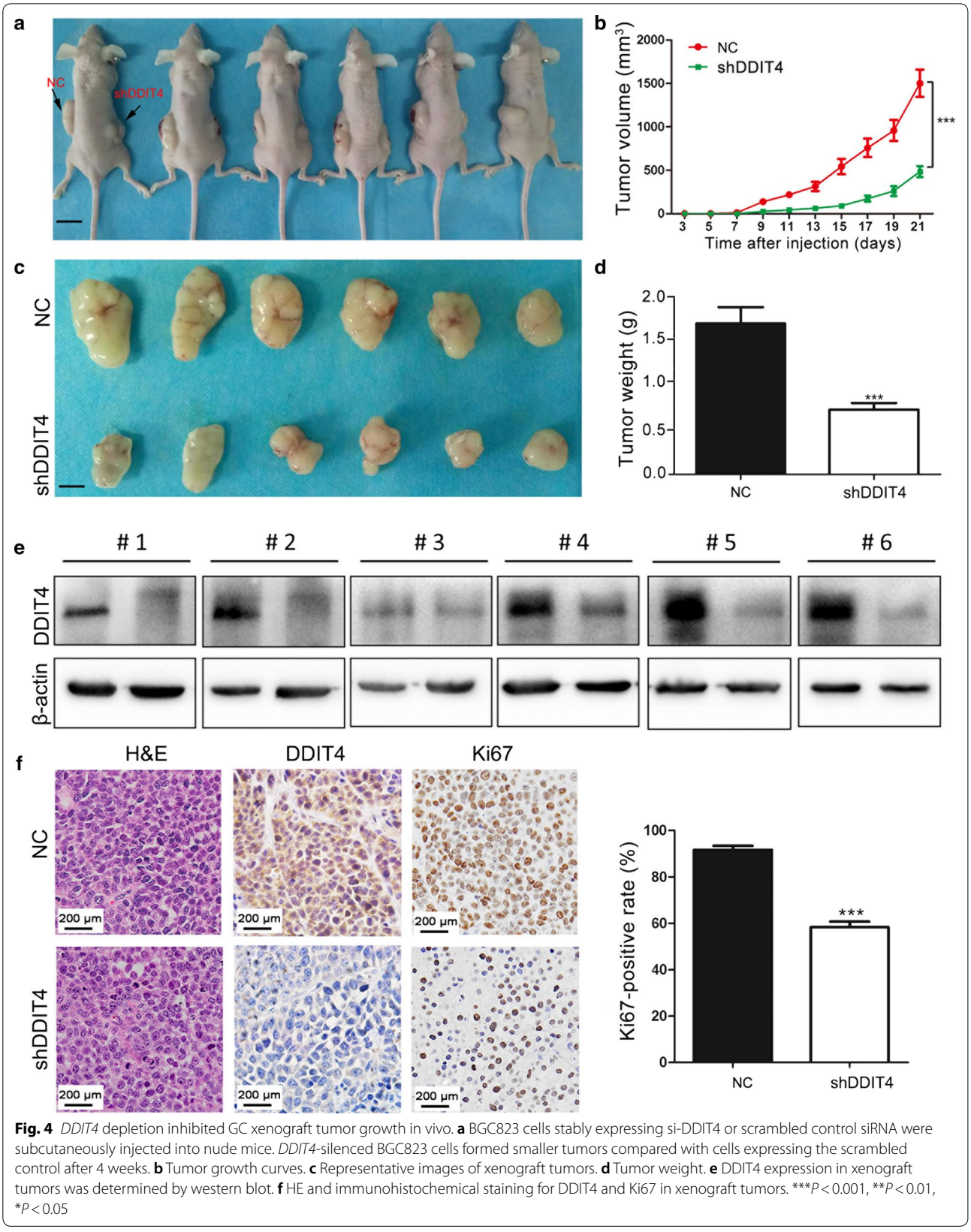

Fig. 4 *DDIT4* depletion inhibited GC xenograft tumor growth in vivo. **a** BGC823 cells stably expressing si-DDIT4 or scrambled control siRNA were subcutaneously injected into nude mice. *DDIT4*-silenced BGC823 cells formed smaller tumors compared with cells expressing the scrambled control after 4 weeks. **b** Tumor growth curves. **c** Representative images of xenograft tumors. **d** Tumor weight. **e** DDIT4 expression in xenograft tumors was determined by western blot. **f** HE and immunohistochemical staining for DDIT4 and Ki67 in xenograft tumors. ***$P < 0.001$, **$P < 0.01$, *$P < 0.05$

(See figure on next page.)

Fig. 5 Downregulation of *DDIT4* activates the mitogen-activated protein kinase (MAPK) and p53 pathways in GC cells. **a** The total and phosphorylated levels of AKT, mTOR and 4EBP1 in *DDIT4*-silenced and *DDIT4*-overexpressing cells were examined by western blot. **b** The total and phosphorylated levels of MEK1, P42/44-MAPK, BCL-1, BAD, p53, and $p21^{Cip1}$ in *DDIT4*-silenced and *DDIT4*-overexpressing cells were examined by western blot. **c**, **d** SGC7901 and BGC823 cells were infected shDDIT4 lentivirus and then were treated with inhibitors specific to p53 (A15201) or MAPK (PD98059). **c** The protein expression levels of phosphorylated and total ERK, BCL-2, p53 and $p21^{Cip1}$ were analyzed by western blot. **d** Cell proliferation was analyzed by CCK8 assay

is involved in anti-tumor chemotherapeutic treatment. For example, baicalein upregulates DDIT4 and causes mTORC1 and growth inhibition in platinum-resistant cancer cells [7]. Melatonin enhances arsenic trioxide-induced cell death via sustained upregulation of DDIT4 expression in breast cancer cells [21]. DDIT4 expression is an independent prognostic factor for triple-negative breast cancer resistant to neoadjuvant chemotherapy [12]. Here, we investigated the role of DDIT4 in response to increasing concentrations of 5-FU. We found that DDIT4 did not alter apoptosis and the cell cycle of GC cells in the absence of 5-FU but reduced apoptotic rate and S phase arrest in GES cells. In contrast, downregulation of *DDIT4* in GC cells increased cell apoptosis and S phase arrest. Collectively, our findings indicated that DDIT4 might contribute to GC development and chemosensitivity, suggesting that inhibiting DDIT4-mediated apoptosis and cell cycle arrest can lead to a greater apoptotic response and retard the cell cycle, thereby potentiating the efficacy of the chemotherapeutic agents against cancer.

Pinto et al. [12] demonstrated with an analysis in KM-Plotter that DDIT4 expression over the median is a protective factor for time to first progression (HR = 0.62; 95% CI 0.5–0.75, $P = 1.7 \times 10^{-6}$). However, analysis of the data downloaded from The Cancer Genome Atlas (TCGA) for gastric adenocarcinoma did not reveal differences in survival when comparing two groups with low and high DDIT4 expression (*P*-value in the log rank test of 0.999) [12]. In our study, we found that DDIT4 expression was increased in GC and that it functioned as an oncogene. In addition, univariate survival analysis revealed that DDIT4 did not exhibit statistically significant associations with GC patient survival, which is consistent with TCGA analysis for gastric adenocarcinoma. The inconsistencies of the evaluation of DDIT4 implied that the prognostic value of DDIT4 requires further investigation.

Reversible protein phosphorylation is one of the most important biological mechanisms for signal transduction, which is tightly regulated by protein kinases and phosphatases to maintain the balance of the protein's phosphorylation status and control its biological functions [22]. Accumulating evidence indicates that perturbation of this balance contributes to the origin and pathogenesis of several human diseases. In cigarette smoke-induced pulmonary injury and emphysema, DDIT4 is necessary and sufficient for nuclear factor-kappaB (NF-kappaB) activation, and promoted alveolar inflammation, oxidative stress and apoptosis in alveolar septal cells [23]. DDIT4 promotes protein phosphatase 2A (PP2A)-dependent de-phosphorylation of AKT on Thr (308) but not on Ser (473) for phosphorylation of TSC2 [24]. Moreover, DDIT4 displays critical roles in hypoxia-inducible factor-1 (HIF-1) and p53 pathway crosstalk [4, 25]. However, the specific oncogenic pathway regulated by DDIT4 under different conditions remains unclear. In our study, we explored the mechanistic basis for DDIT4-mediated regulation of GC cells using phospho-antibody microarray-based proteomic analysis and found that the proliferation-suppressive and chemosensitive effect of *DDIT4* downregulation might be associated with activation of the MAPK signaling pathway, resulting in subsequent phosphorylation of BCL-2 (p-Ser70), which inhibits cell proliferation and induces apoptosis. Consistent with previous studies, we demonstrated that the MAPK pathway is frequently activated in human cancers, leading to malignant phenotypes such as autonomous cellular proliferation [26]. In addition to the MAPK signaling pathway, extensive studies have demonstrated that the p53 tumor suppressor protein preserves genome integrity by regulating growth arrest and apoptosis in response to DNA damage [27–29]. This notion is further supported by our data demonstrating that DDIT4 regulated the activation of multiple pro-apoptotic and growth-suppressive proteins, including p53. The p53 protein displayed a dual change in its phosphorylation state in *DDIT4*-knockdown cells compared with negative controls, as follows: (1) downregulation of phosphorylation at Ser6, which induces apoptosis; and (2) upregulation of phosphorylation at Ser315, leading to phosphorylation of $p21^{Cis1}$ (p-Thr145), which rescues cells from apoptosis. Thus, in our study, we identified multiple pro-apoptotic and growth-suppressive proteins of which the phosphorylation and activation levels were regulated by DDIT4 in GC cells.

Conclusions

In summary, our results demonstrated that DDIT4 promoted the tumorigenicity of gastric cancer cells by facilitating proliferation and colony formation and alleviating

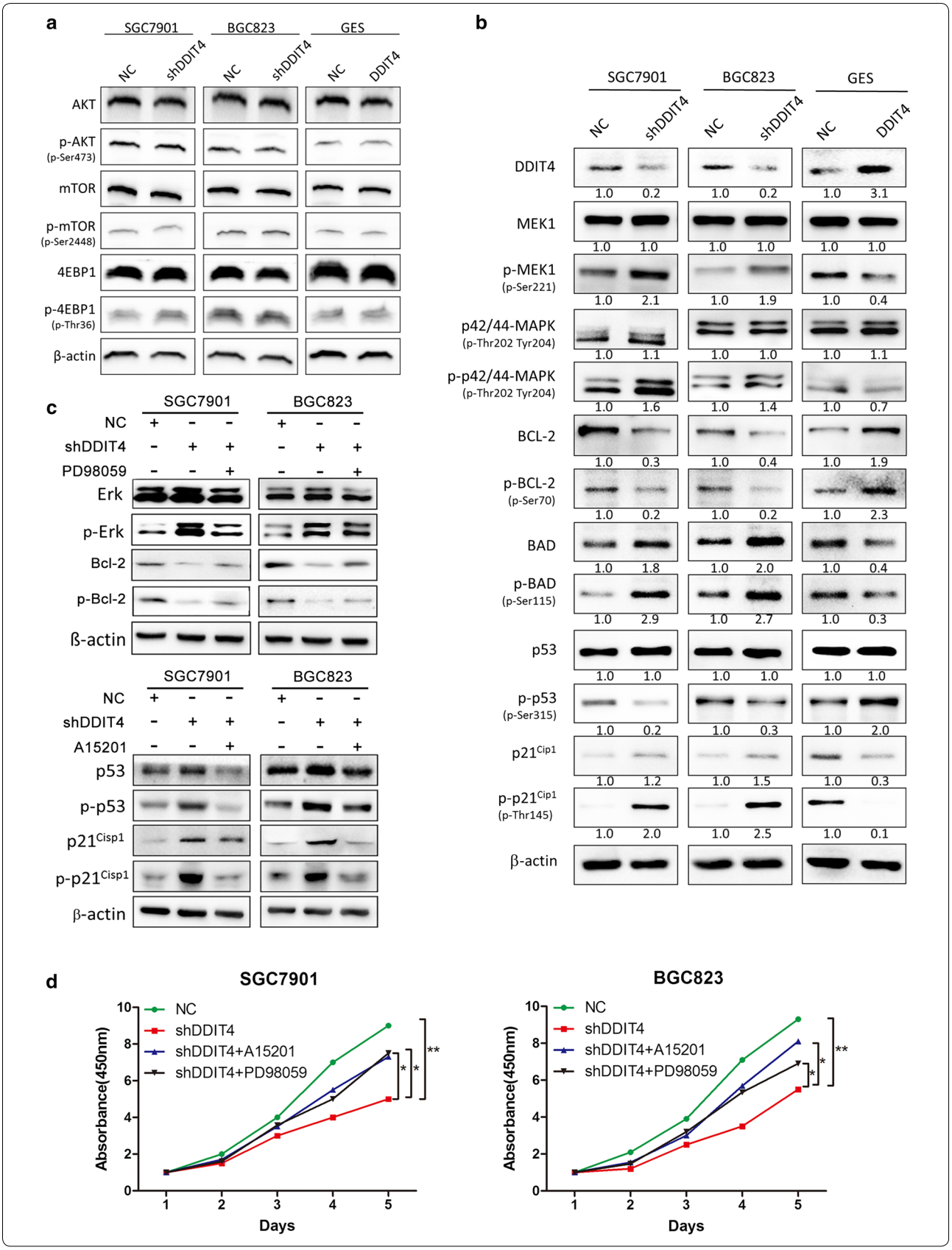
a
SGC7901
BGC823
GES
NC
shDDIT4
DDIT4
AKT
p-AKT (p-Ser473)
mTOR
p-mTOR (p-Ser2448)
4EBP1
p-4EBP1 (p-Thr36)
β-actin
b
DDIT4
MEK1
p-MEK1 (p-Ser221)
p42/44-MAPK (p-Thr202 Tyr204)
p-p42/44-MAPK (p-Thr202 Tyr204)
BCL-2
p-BCL-2 (p-Ser70)
BAD
p-BAD (p-Ser115)
p53
p-p53 (p-Ser315)
p21Cip1
p-p21Cip1 (p-Thr145)
β-actin
c
NC
shDDIT4
PD98059
Erk
p-Erk
Bcl-2
p-Bcl-2
ß-actin
A15201
p53
p-p53
p21Cisp1
p-p21Cisp1
β-actin
d
SGC7901
BGC823
NC
shDDIT4
shDDIT4+A15201
shDDIT4+PD98059
Absorbance(450nm)
Days

5-FU-induced apoptosis through the p53 and MAPK pathways. The mouse model experiment further demonstrated that *DDIT4* downregulation significantly inhibited tumor growth in vivo. Taken together, our results suggest that DDIT4 may function as an oncogene in gastric cancer, providing a promising therapeutic strategy for GC treatment.

Additional files

Additional file 1: Figure S1. The effect of DDIT4 downregulation on GC cell migration and invasion.

Additional file 2: Table S1. The effect of DDIT4-knockdown on phosphorylation of signal protein.

Abbreviations

DDIT4: DNA-damage-inducible transcript 4; GC: gastric cancer; MAPK: mitogen-activated protein kinase; PC: prostate cancer; OC: ovarian cancer; NF-kappaB: nuclear factor-kappaB; PP2A: protein phosphatase 2A.

Authors' contributions

XZ, YL, YN and DF conceived and directed the projects. FD, XZ and YL designed experiments. FD, LS and YT performed experiments, FD, TL, CL, MJ, XW, and YM conducted data analysis and interpreted the results. FD and XZ wrote and edited the manuscript. All authors read and approved the final manuscript.

Acknowledgements

We acknowledge Lei Geng, Fenli Zhou, Jianhua Dou and Guangbo Tang for their generous help to the present study.

Competing interests

The authors declare that they have no competing interests.

Availability of data and materials

Not applicable.

Consent for publication

Not applicable.

Ethics approval and consent to participate

The present study was approved by the Medical Ethics Committee of Xijing Hospital. All protocols involving animals in the present study were approved by the laboratory animal ethics committee of Fourth Military Medical University. All the animals experimental procedures were performed in accordance with the Guide for the Care and Use of Laboratory Animals (NIH publications Nos. 80-23, revised 1996) and the institutional ethical guidelines for animal experiments.

Funding

The present study was supported by the National Natural Science Foundation of China (Nos. 81430072, 81421003, 81602641, 81572929).

Received: 16 July 2017 Accepted: 15 June 2018
Published online: 05 July 2018

References

1. Sun W, Yan L. Gastric cancer: current and evolving treatment landscape. Chin J Cancer. 2016;35(1):83.
2. Crew KD, Neugut AI. Epidemiology of gastric cancer. World J Gastroenterol. 2006;12(3):354–62.
3. Bass AJ, Thorsson V, Shmulevich I, Reynolds SM, Miller M, Bernard B, et al. Comprehensive molecular characterization of gastric adenocarcinoma. Nature. 2014;513(7517):202–9.
4. Ellisen LW, Ramsayer KD, Johannessen CM, Yang A, Beppu H, Minda K, et al. REDD1, a developmentally regulated transcriptional target of p63 and p53, links p63 to regulation of reactive oxygen species. Mol Cell. 2002;10(5):995–1005.
5. DeYoung MP, Horak P, Sofer A, Sgroi D, Ellisen LW. Hypoxia regulates TSC1/2-mTOR signaling and tumor suppression through REDD1-mediated 14-3-3 shuttling. Genes Dev. 2008;22(2):239–51.
6. Barakat DJ, Mendonca J, Barberi T, Zhang J, Kachhap SK, Paz-Priel I, et al. C/EBPbeta regulates sensitivity to bortezomib in prostate cancer cells by inducing REDD1 and autophagosome-lysosome fusion. Cancer Lett. 2016;375(1):152–61.
7. Wang Y, Han E, Xing Q, Yan J, Arrington A, Wang C, et al. Baicalein upregulates DDIT4 expression which mediates mTOR inhibition and growth inhibition in cancer cells. Cancer Lett. 2015;358(2):170–9.
8. Gordon MA, D'Amato NC, Gu H, Babbs B, Wulfkuhle J, Petricoin EF, et al. Synergy between androgen receptor antagonism and inhibition of mTOR and HER2 in breast cancer. Mol Cancer Ther. 2017;16:1389–400.
9. Rehan M. An anti-cancer drug candidate OSI-027 and its analog as inhibitors of mTOR: computational insights into the inhibitory mechanisms. J Cell Biochem. 2017;118:4558–67.
10. Molitoris JK, McColl KS, Swerdlow S, Matsuyama M, Lam M, Finkel TH, et al. Glucocorticoid elevation of dexamethasone-induced gene 2 (Dig2/RTP801/REDD1) protein mediates autophagy in lymphocytes. J Biol Chem. 2011;286(34):30181–9.
11. Jia W, Chang B, Sun L, Zhu H, Pang L, Tao L, et al. REDD1 and p-AKT overexpression may predict poor prognosis in ovarian cancer. Int J Clin Exp Pathol. 2014;7(9):5940–9.
12. Pinto JA, Rolfo C, Raez LE, Prado A, Araujo JM, Bravo L, et al. In silico evaluation of DNA damage inducible transcript 4 gene (DDIT4) as prognostic biomarker in several malignancies. Sci Rep. 2017;7(1):1526.
13. Evan GI, Vousden KH. Proliferation, cell cycle and apoptosis in cancer. Nature. 2001;411(6835):342–8.
14. Kalisperati P, Spanou E, Pateras IS, Korkolopoulou P, Varvarigou A, Karavokyros I, et al. Inflammation, DNA damage, *Helicobacter pylori* and gastric tumorigenesis. Front Genet. 2017;8:20.
15. Coussens LM, Werb Z. Inflammation and cancer. Nature. 2002;420(6917):860–7.
16. Negrini S, Gorgoulis VG, Halazonetis TD. Genomic instability—an evolving hallmark of cancer. Nat Rev Mol Cell Biol. 2010;11(3):220–8.
17. Luo J, Solimini NL, Elledge SJ. Principles of cancer therapy: oncogene and non-oncogene addiction. Cell. 2009;136(5):823–37.
18. Zhou X, Liu W, Hu X, Dorrance A, Garzon R, Houghton PJ, et al. Regulation of CHK1 by mTOR contributes to the evasion of DNA damage barrier of cancer cells. Sci Rep. 2017;7(1):1535.
19. Hwang-Verslues WW, Chang PH, Wei PC, Yang CY, Huang CK, Kuo WH, et al. miR-495 is upregulated by E12/E47 in breast cancer stem cells, and promotes oncogenesis and hypoxia resistance via downregulation of E-cadherin and REDD1. Oncogene. 2011;30(21):2463–74.
20. Jin HO, Seo SK, Woo SH, Kim YS, Hong SE, Yi JY, et al. Redd1 inhibits the invasiveness of non-small cell lung cancer cells. Biochem Biophys Res Commun. 2011;407(3):507–11.
21. Yun SM, Woo SH, Oh ST, Hong SE, Choe TB, Ye SK, et al. Melatonin enhances arsenic trioxide-induced cell death via sustained upregulation of Redd1 expression in breast cancer cells. Mol Cell Endocrinol. 2016;422:64–73.
22. Iakoucheva LM, Radivojac P, Brown CJ, O'Connor TR, Sikes JG, Obradovic Z, et al. The importance of intrinsic disorder for protein phosphorylation. Nucleic Acids Res. 2004;32(3):1037–49.
23. Yoshida T, Mett I, Bhunia AK, Bowman J, Perez M, Zhang L, et al. Rtp801, a suppressor of mTOR signaling, is an essential mediator of cigarette smoke-induced pulmonary injury and emphysema. Nat Med. 2010;16(7):767–73.
24. Dennis MD, Coleman CS, Berg A, Jefferson LS, Kimball SR. REDD1 enhances protein phosphatase 2A-mediated dephosphorylation of Akt to repress mTORC1 signaling. Sci Signal. 2014;7(335):a68.
25. Horak P, Crawford AR, Vadysirisack DD, Nash ZM, DeYoung MP, Sgroi D, et al. Negative feedback control of HIF-1 through REDD1-regulated ROS suppresses tumorigenesis. Proc Natl Acad Sci USA. 2010;107(10):4675–80.

26. Wagner EF, Nebreda AR. Signal integration by JNK and p38 MAPK pathways in cancer development. Nat Rev Cancer. 2009;9(8):537–49.
27. Deng C, Zhang P, Harper JW, Elledge SJ, Leder P. Mice lacking p21CIP1/WAF1 undergo normal development, but are defective in G1 checkpoint control. Cell. 1995;82(4):675–84.
28. Tibbetts RS, Brumbaugh KM, Williams JM, Sarkaria JN, Cliby WA, Shieh SY, et al. A role for ATR in the DNA damage-induced phosphorylation of p53. Genes Dev. 1999;13(2):152–7.
29. Miyashita T, Reed JC. Tumor suppressor p53 is a direct transcriptional activator of the human bax gene. Cell. 1995;80(2):293–9.

Article

SOURCE DATA | TRANSPARENT PROCESS | OPEN ACCESS

EMBO Molecular Medicine

Combined targeting of G protein-coupled receptor and EGF receptor signaling overcomes resistance to PI3K pathway inhibitors in PTEN-null triple negative breast cancer

Davide Zecchin[1], Christopher Moore[1], Fanourios Michailidis[1], Stuart Horswell[2], Sareena Rana[1,3], Michael Howell[4] & Julian Downward[1,3,*]

Abstract

Triple-negative breast cancer (TNBC) has poorer prognosis compared to other types of breast cancers due to the lack of effective therapies and markers for patient stratification. Loss of PTEN tumor suppressor gene expression is a frequent event in TNBC, resulting in over-activation of the PI 3-kinase (PI3K) pathway and sensitivity to its inhibition. However, PI3K pathway inhibitors show limited efficacy as monotherapies on these tumors. We report a whole-genome screen to identify targets whose inhibition enhanced the effects of different PI3K pathway inhibitors on PTEN-null TNBC. This identified a signaling network that relies on both the G protein-coupled receptor for thrombin (PAR1/F2R) and downstream G protein βγ subunits and also epidermal growth factor receptor (EGFR) for the activation of the PI3K isoform p110β and AKT. Compensation mechanisms involving these two branches of the pathway could bypass PI3K blockade, but combination targeting of both EGFR and PI3Kβ suppressed ribosomal protein S6 phosphorylation and exerted anti-tumor activity both *in vitro* and *in vivo*, suggesting a new potential therapeutic strategy for PTEN-null TNBC.

Keywords G protein; p110β; PTEN; resistance; triple-negative breast cancer
Subject Categories Cancer; Pharmacology & Drug Discovery; Signal Transduction
DOI 10.15252/emmm.202011987 | Received 6 January 2020 | Revised 9 June 2020 | Accepted 16 June 2020 | Published online 16 July 2020
EMBO Mol Med (2020) 12: e11987

Introduction

Triple-negative breast cancer (TNBC) is defined by the lack of expression of the actionable markers estrogen receptor (ER), progesterone receptor (PR), and human epidermal growth factor receptor 2 (HER2). It accounts for about 15% of all breast cancer. There are no targeted therapies currently available in the clinic for the treatment of TNBC besides chemotherapy (Chacon & Costanzo, 2010; Bianchini *et al*, 2016). Despite being chemosensitive, TNBC is characterized by a short time to progression and by the poorest prognosis among the other subtypes of breast cancers (Liedtke *et al*, 2008). The aggressiveness and heterogeneity of this disease, together with the current paucity of therapeutic options, suggests a need for new molecular markers for patient stratification and new targeting approaches for the treatment of TNBC.

PTEN deficiency occurs in up to 35% of TNBC (Cancer Genome Atlas Network, 2012), representing one of the most commonly altered tumor suppressor genes in this subtype of cancer. PTEN is a lipid phosphatase that dephosphorylates PtdIns $(3,4,5)P_3$ to form PtdIns$(4,5)P_2$ and counteracts the enzymatic activity of PI3K (Maehama & Dixon, 1998). Loss of PTEN results in accumulation of PtdIns$(3,4,5)P_3$ at the inner surface of the plasma membrane and over-activation of AKT (Stambolic *et al*, 1998; Haddadi *et al*, 2018). Consistently with its effect at the signaling level, PTEN-deficient TNBCs show up-regulation of markers of activation of PI3K pathway, such as phospho-AKT (both Thr308 and Ser473), phospho-mTOR, phospho-$p70^{S6K}$, phospho-S6, and phospho-4EBP1 (Stemke-Hale *et al*, 2008; Cancer Genome Atlas Network, 2012). Pre-clinical evidence also showed that PTEN-null tumors, including breast cancers, are sensitive to the inhibition of PI3K pathway and in particular to the targeting of specific nodes of the signaling route, such as the β isoform of PI3K (Jia *et al*, 2008; Wee *et al*, 2008; Hancox *et al*, 2015) and AKT (Chen *et al*, 2006; Vasudevan *et al*, 2009; Sangai *et al*, 2012).

Drugs targeting multiple components of the PI3K pathway, including PI3Kβ and AKT inhibitors, are in clinical trials (reviewed in (Janku *et al*, 2018)) and may represent a rational therapeutic

1 Oncogene Biology, Francis Crick Institute, London, UK
2 Computational Biology, Francis Crick Institute, London, UK
3 Lung Cancer Group, Institute of Cancer Research, London, UK
4 High Throughput Screening Laboratories, Francis Crick Institute, London, UK
*Corresponding author. Tel: +44 20 3796 1838; E-mail: julian.downward@crick.ac.uk

opportunity to treat the subgroup of TNBCs characterized by PTEN deficiency (Delaloge & DeForceville, 2017). The success obtained employing PI3K isoform-specific inhibitors in the treatment of relapsed chronic lymphocytic leukemia (CLL) (Furman *et al*, 2014), relapsed indolent lymphoma (Gopal *et al*, 2014), and PIK3CA-mutant breast cancers (Juric *et al*, 2018a,b) demonstrated the clinical potential of inhibiting specific nodes of PI3K signaling in patients selected based on cancer type and biomarkers. However, apart from those specific contexts, PI3K pathway inhibitors generally delivered only modest effects in the clinical setting (Janku *et al*, 2018), and no clear evidence of benefits for PTEN-deficient tumor patients has been reported so far (Kim *et al*, 2017; Martin *et al*, 2017). While pre-clinical data indicate the requirement for PI3K pathway activity for the survival and proliferation of PTEN-null TNBC cells, clinical evidence suggests the need to inhibit additional targets to enhance the effect of PI3K pathway inhibitors, widen their therapeutic window, reduce their toxicity, and produce a sustained anti-tumor effect.

We set out to interrogate the whole genome to identify additional targets whose inhibition might synergize with inhibitors of the PI3K pathway. We focused on drugs affecting different nodes of the PI3K pathway, with particular attention to PI3Kβ isoform, pan-PI3K and AKT inhibitors. Our investigation revealed a previously unappreciated complexity of compensation mechanisms that impairs the response to PI3K pathway inhibitors in PTEN-deficient TNBC. This knowledge has paved the way to the rational design of possible combinatorial targeting strategies for the effective treatment of this type of cancer.

Results

A whole-genome shRNA screen identified EGFR inhibition as enhancer of the response to PI3K pathway inhibitors in triple-negative breast cancer cells

A number of pre-clinical models showed that PTEN-deficient cancer cells are sensitive to inhibition of PI3K pathway, and this was particularly clear when p110β or AKT were selectively targeted (Chen *et al*, 2006; Jia *et al*, 2008; Wee *et al*, 2008; Vasudevan *et al*, 2009). However, in most of the cases, PI3K pathway inhibitors only partially impaired the proliferation of PTEN-null cancer cells (Fig EV1A). In order to identify genes whose silencing could enhance the effect of PI3K and AKT inhibitors, we performed a whole-genome short hairpin (sh) RNA interference screen in combination with drugs targeting the PI3K pathway, including an isoform-specific p110β/δ inhibitor (AZD8186), a pan-PI3K class I inhibitor (GDC0941), and an AKT inhibitor (MK2206). AZD8186 inhibits with high affinity both p110β and p110δ isoforms (IC50 = 4 nM for p110β and 12 nM for p110δ). However, PTEN-null triple-negative human breast cancer (TNBC) cells, the main focus of our study, do not express appreciable levels of p110δ, as shown by comparing expression levels of the genes encoding p110 isoforms in these cells and in B-cell acute lymphoblastic leukemia lines (Fig EV1B, https://portals.broadinstitute.org/ccle), that express all p110 isoforms (Thorpe *et al*, 2015). It is therefore likely that the effects observed following treatment by AZD8186 in PTEN-null TNBC cell lines are due to targeting of p110β, rather than p110δ.

Figure 1. A short-hairpin screening identified hits whose inhibition enhanced the effect of PI3K pathway inhibitors on PTEN-deficient triple-negative breast cancers.

A Schematic representation of the shRNA screening aimed to identify genes whose knock-down enhanced the anti-proliferative effects of AZD8186 (PI3Kβi), GDC0941 (pan-PI3Ki), or MK2206 (AKTi) on the PTEN-null cell line MDA-MB-468. The shRNAs directed against the transcripts of three genes are shown in three different colors. shRNAs against gene 1 are depleted in the vehicle-treated condition compared to time 0, and they most likely target an essential gene. shRNAs against the transcripts of gene 2 are unchanged in all conditions, while shRNAs silencing gene 3 are selectively depleted in the AZD8186-selected cells compared to vehicle and their abundance is not affected by the 2-week long culture with vehicle. Gene 3 is a good candidate for inhibition in combination with AZD8186.

B Dot-plot showing the fold change (log_2) in number of reads between vehicle- and AZD8186-treated conditions vs the *P*-value of the difference between the two treatment conditions for each shRNA. 9 out of 18 shRNAs targeting EGFR showed a *P*-value < 0.2 and are highlighted in the plot. The plot was generated considering the results from biological triplicate of the experiment.

C, D MDA-MB-468 was infected with the indicated shRNAs targeting EGFR and selected by puromycin. EGFR mRNA was then measured by RT–qPCR (C), and cell viability was measured after 4 days of treatment with serial dilutions of AZD8186 (D). Average ± SD of triplicates and representative of three independent experiments.

E, F MDA-MB-468 was treated with serial dilutions of gefitinib (E) or lapatinib (F) in the presence of vehicle, AZD8186 (0.25 μM), GDC0941 (0.25 μM), or MK2206 (0.45 μM), as indicated. Cell viability was measured after 4 days and normalized within each of the PI3K pathway inhibitor-treated condition to the viability in the absence of gefitinib or lapatinib. Average ± SD of triplicates and representative of two independent experiments.

G Viability of six PTEN-null vs five PTEN-WT TNBC cell lines—not carrying other known mutations in PIK3CA, PIK3CB, or PIK3R1 genes—treated with PI3Kβi (AZD8186 90 nM), EGFRi (gefitinib 3 μM) alone, or in combination for 6 days. Mean of 3 independent experiments ± SD. Statistical significance of two-tailed unpaired student *t*-test in PTEN-null PI3Kbi vs PI3Kbi + EGFRi $^{**}P = 0.0059$, PTEN-null EGFRi vs PI3Kbi + EGFRi $^{**}P = 0.0047$, PTEN-null PI3Kbi + EGFRi vs PTEN-WT PI3Kbi + EGFRi $^{*}P = 0.0459$, PTEN-WT PI3Kbi vs PI3Kbi + EGFRi $^{*}P = 0.0108$, PTEN-WT EGFRi vs PI3Kbi + EGFRi n.s. $P = 0.1926$. PTEN-null cell lines used in the experiments were as follows: MDA-MB-468, HCC70, HCC1937, HCC38, HCC1395, and BT-549; PTEN-WT cell lines were as follows: MDA-MB-157, MDA-MB-231, HCC1187, HCC1428, and HCC1806.

H Synergy score for combinations of serial dilutions of PI3Kβi (AZD8186) plus EGFRi (gefitinib) tested on six PTEN-null and five PTEN-WT TNBC cell lines for 6 days in three independent experiments. The score was obtained analyzing the viability data through the software Chalice Analyser. Mean of the synergy scores ± SD. Statistical significance of Mann–Whitney two-tailed test $^{*}P = 0.0303$.

I Patient samples from METABRIC dataset classified as TNBCs were assigned to the groups "PTEN-low" when falling in the lower quartile for PTEN expression, "PTEN-mut" when harboring a non-synonymous mutation on PTEN gene, "PTEN-WT" in all other cases. Comparison of the expression of EGFR between the PTEN low or mut and the PTEN-WT groups. Data presented in a box and whisker plot with the central band indicating the median, the upper, and lower extremes of the box or hinge being the third and first quartiles, respectively, and the whiskers extending to the most extreme data values. Mean ± SD. *P*-value calculated by unpaired *t* test.

Source data are available online for this figure.

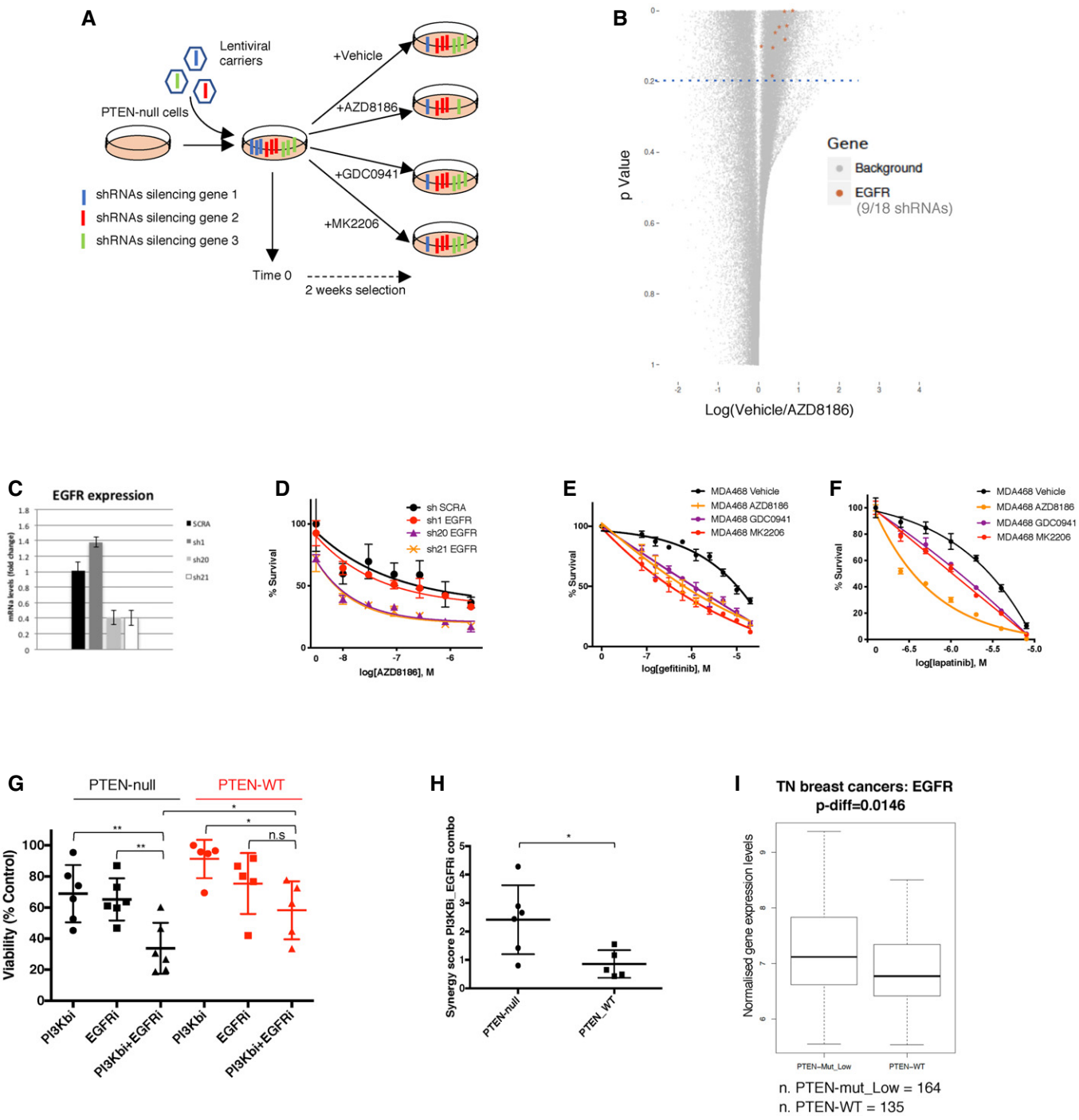

Figure 1.

As a cellular model, we employed the PTEN-deficient TNBC cell line MDA-MB-468. Also, EGFR is genetically amplified and overexpressed in this cell line, recapitulating molecular features of a significant fraction of TNBCs (Reis-Filho *et al*, 2006; Reis-Filho & Tutt, 2008; Gumuskaya *et al*, 2010; Shao *et al*, 2011; Martin *et al*, 2012; Park *et al*, 2014; Nakai *et al*, 2016). MDA-MB-468 exhibited average sensitivity to PI3K pathway inhibitors compared to other cell lines with similar genetic alterations and origin (Fig EV1A). The cancer cells were infected with a library of lentiviral vectors expressing shRNAs targeting most of the genes encoded by the human genome (around 16,000 genes) in combination with either vehicle, AZD8186, GDC0941, or MK2206 treatments (Fig 1A). AZD8186 was employed at a concentration that selectively targeted p110β over p110α (Schwartz *et al*, 2015). Similar to AZD8186, also GDC0941, and MK2206 were used at concentrations close to the IC_{30} for MDA-MB-468 cells (Fig EV1C), in order to allow the

silencing of specific genes to show synergistic effects in combination with the drugs.

After 14 days of drug selection, the genomic DNA of cells in different treatment conditions was extracted and sequenced to evaluate the relative abundance of the different shRNA species within the cellular populations. We initially filtered genes for which at least two shRNAs were selectively depleted in the treated compared to untreated condition (see Materials and Methods) and these genes were then ranked based on the effect (lowest treatment/control reads ratio) of their second-best performing shRNA (Table EV1). We identified nine shRNAs targeting EGFR that were consistently depleted in the AZD8186-treated condition compared to the vehicle control (Fig 1B), and the EGFR gene ranked within the top 1% candidates in all treatment conditions (Table EV1). We validated our findings by infecting MDA-MB-468 with three shRNAs targeting EGFR and previously included in the shRNA screening. Only two shRNAs were able to effectively silence the expression of EGFR (Fig 1C), and those two shRNAs were the ones showing a combination effect with AZD8186 treatment in impairing the proliferation of MDA-MB-468 (Fig 1D).

Next, we validated the cooperation between PI3K pathway and EGFR inhibition by the use of EGFR-targeted drugs. We observed increased activity in MDA-MB-468 for different EGFR inhibitors, including small molecules gefitinib, lapatinib, erlotinib, and the monoclonal antibody cetuximab, in the presence of AZD8186, but also in the presence of other inhibitors of PI3K pathway such as GDC0941 or MK2206 compared to vehicle control (Figs 1E and F and EV1D). It is noticeable that both genetic and pharmacological suppression of EGFR in MDA-MB-468 exerted only marginal anti-proliferative effect on its own. This is in line with the lack of response to EGFR inhibitors observed in clinical trials in triple-negative breast cancers (von Minckwitz *et al*, 2005; Dickler *et al*, 2008; Carey *et al*, 2012; Yardley *et al*, 2016). We also extended our findings using a panel of TNBC cell lines, comparing the effect of drug combinations on PTEN-deficient and PTEN-WT cell lines. All cell lines employed in these experiments did not harbor any known mutation in PIK3CA, PIK3CB, PIK3R1, or KRAS that may confound or modify the response to those drugs (COSMIC database). The combination of gefitinib and AZD8186, MK2206, or GDC0941 cooperatively reduced the cell viability in the panel of PTEN-null cells, while their effect on PTEN-WT models was considerably more limited (Figs 1G and, EV1E and F). Consistently, a higher synergistic score for the drug combination including AZD8186 and gefitinib was calculated in PTEN-deficient cell lines compared to WT (Fig 1H), showing that this combinatorial regimen is especially effective in a PTEN-null genetic background for triple-negative breast cancers. We also tested the combination of BYL719 (a p110α isoform-selective inhibitor) and gefitinib on three PTEN-null and three PTEN WT TNBC cell lines. In contrast to the combination with AZD8186, BYL719 combined with gefitinib did not produce any genotype-selective anti-proliferative effect on the PTEN-deficient cell lines, confirming that AZD8186 exerted its function by inhibiting p110β rather than p110α (Fig EV1G).

In order to test the relevance of our findings in patient samples, we asked whether EGFR was differentially expressed depending on PTEN status in the triple-negative breast cancer samples of the METABRIC database. We found that samples showing low expression and/or non-synonymous mutation of PTEN had statistically significant higher expression of EGFR compared to samples expressing higher level of WT PTEN (Fig 1I).

Through the analysis of the shRNA screening data, we also identified multiple shRNAs targeting the casein kinase 2 (CK2) components CSNK2B and CSNK2A2 as being depleted in the AZD8186-treated condition compared to vehicle (Fig EV1H). Those genes encode the regulatory (β) and one of the catalytic (α′) subunits of CK2 holoenzyme, respectively. The knock-down of CSNK2B by three of the shRNAs included in the screening showed a correlation between the degree of transcript down-regulation (Fig EV1I) and the enhancement of AZD8186 activity (Fig EV1J) in MDA-MB-468 cells, validating the results of the screening. We further confirmed those data by the use of CX-4945, a CK2 targeted kinase inhibitor (Fig EV1K). We observed that CX-4945 cooperatively reduced cell viability when combined with AZD8186, GDC0941, or MK2206 in a panel of PTEN-deficient TNBC cell lines, while the same effect was not found in PTEN-WT TNBC cells (Fig EV1L–N). Altogether, these data showed that EGFR or CK2 inhibition can potentiate the activity of PI3K pathway inhibitors selectively on those TNBCs lacking functional PTEN.

Combinatorial targeting of PI3Kβ isoform and EGFR exerts anti-tumor effects on PTEN-null TNBC *in vivo*

We reasoned that simultaneous and specific inhibition of PI3Kβ isoform and EGFR may lead to a sustained synergistic anti-tumor effect also *in vivo* with a well-tolerated toxicity profile. This approach might be more tolerable than targeting both p110α and p110β using pan-PI3K inhibitors or inhibiting the downstream master regulator AKT. We evaluated the *in vivo* efficacy and the toxicity of the combination of AZD8186 and erlotinib on mice injected orthotopically in the mammary fat pads with the human cancer cells MDA-MB-468 or HCC70. These two cell lines both express high levels of EGFR, and they show different degree of sensitivity to AZD8186, GDC0941, and MK2206 *in vitro* (Fig EV1A). We observed in all cases no effect or only partial tumor growth inhibition for the single drug treatments. This was the case also for mice transplanted with HCC70, although those cells had previously shown higher sensitivity *in vitro* to AZD8186-mediated inhibition. The combination prevented tumor growth in MDA-MB-468 xenografts (Figs 2A and EV2A) and induced regression in HCC70 tumors (Fig 2B and C). The body weight of treated mice did not significantly change during single or combined treatments (Fig 2D), and no other signs of toxicity were detected, suggesting that the drug combination can be well tolerated *in vivo*.

Next, we asked whether the combined inhibition of PI3Kβ and EGFR may prove effective also in an immunocompetent context. We took advantage of a *Wap-cre:Pten*$^{fl/fl}$*:Tp53*$^{fl/fl}$ mouse model in which the expression of *Cre* by the *Wap* promoter drives the conditional inactivation of *Pten* and *Tp53* floxed alleles in the alveolar epithelial cells of the mammary glands of late pregnant and lactating female mice (Wagner *et al*, 1997). This, in turn, has been reported to induce the formation of triple-negative-like breast tumors with hyper-activated AKT signal and with an average latency of 9.8 months (Liu *et al*, 2014). We recreated the same genetic make-up in pure C57BL6/J background, in order to isolate tumors and derive cell lines that could be re-transplanted in the fourth mammary gland fat pad of immune-competent, syngeneic recipients. This strategy

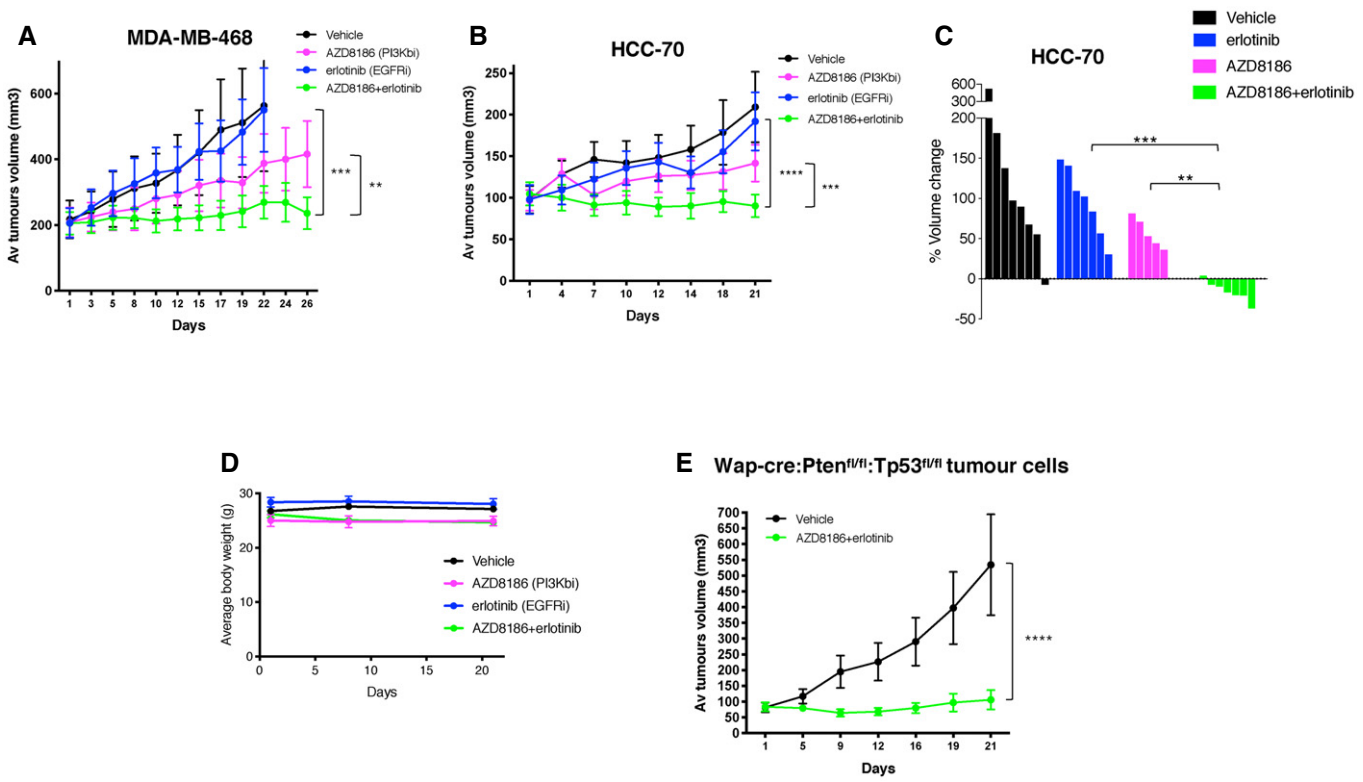

Figure 2. Anti-tumor effects of combinatorial inhibition of PI3Kβ and EGFR on triple-negative breast cancers *in vivo*.

A Tumor volume of MDA-MB-468 mammary fat-pad xenografts treated with vehicle, AZD8186 (50 mg/kg, og twice/day), erlotinib (50 mg/kg IP once/day) alone, or in combination (5–6 mice per group, mean ± SEM). Statistical significance of two-way ANOVA statistical test $^{**}P = 0.0028$ and $^{***}P < 0.0001$.

B Tumor volume of HCC-70 mammary fat-pad xenografts treated with vehicle, AZD8186 (150 mg/kg, og once/day), erlotinib (50 mg/kg IP once/day) alone, or in combination (6–7 mice per group, mean ± SEM). Growth curves were compared using two-way ANOVA statistical test. Statistical significance of two-way ANOVA statistical test $^{***}P = 0.0006$ and $^{****}P < 0.0001$.

C Waterfall representation of changes in the volume of individual HCC-70 tumors during the treatment. Statistical comparison between different treatment groups by Mann–Whitney test $^{**}P = 0.0023$ and $^{***}P = 0.0006$.

D Change in the body weight of mice harboring HCC70 xenograft tumors (6–7 mice per group, mean ± SEM) during 21 days of treatment.

E A cell line derived from a mammary tumor spontaneously developed in a Wap-cre:Pten$^{fl/fl}$:Tp53$^{fl/fl}$ mouse was cloned and injected in the mammary fat pad of syngeneic C57BL6/J recipient mice. Tumors grew in 12 out of 35 transplanted mice, and only these tumors were selected for the treatments described in the figure. When tumors reached an average volume of 100 mm^3, they were treated with vehicle or a combination of AZD8186 (150 mg/kg, og once/day) and erlotinib (50 mg/kg IP once/day). Tumors were then measured during the treatment (six mice per group, mean ± SEM). Statistical significance of two-way ANOVA statistical test $^{****}P < 0.0001$.

Source data are available online for this figure.

allowed the generation of large cohorts of immune-competent mice harboring well-localized and synchronized transplanted tumors that could be challenged with different drug treatments.

We derived cell lines from a PTEN- and TP53-negative, EGFR-positive primary mammary tumor that developed in a *Wap-cre:Pten$^{fl/fl}$:Tp53$^{fl/fl}$* mouse and that was histologically classified as a carcinosarcoma resembling a spindle-cell, triple-negative type of tumor that can be found in the human breast (Fig EV2B). These cells showed a combinatorial response *in vitro* to treatment with AZD8186 and gefitinib (Fig EV2C), validating previous data obtained in human cancer cell lines. One of those clones was transplanted in the mammary fat pad of C57BL6/J female mice, and we observed engraftment of the injected cells in more than 95% of the cases. All mice were treated with vehicle, AZD8186, erlotinib, or a combination of the two drugs soon after engraftment of the cells (Fig EV2D). However, 2/3 of transplanted mice underwent spontaneous tumor regression in the vehicle group. Single drug treatments were not effective in preventing the escape of a fraction of the treated tumors, while all tumors treated with combined AZD8186 and erlotinib showed clear regression.

We then selected out from a cohort of transplanted mice those tumors that were able to escape spontaneous regression,and we observed that the combined treatment with AZD8186 and erlotinib completely prevented the further aggressive growth of those isografts (Fig 2E). These results show that the combined inhibition of PI3Kβ and EGFR exerts anti-tumor effect on aggressive PTEN and TP53-null triple-negative-like breast tumor growth also in immune-competent models. Confirmation of anti-tumor activity and lack of toxicity for the drug combination in both immune-suppressed and immune-competent recipients also makes unlikely that AZD8186 (p110β/δ inhibitor) exerts its effects by targeting p110δ in the immune cell compartment.

Decreased S6 phosphorylation is a marker of response to combinatorial treatments in PTEN-null triple-negative breast cancers

To define the mechanisms responsible for the cooperative impact on viability of the combinatorial regimens, we investigated which changes were induced by single and combined drug treatments at the biochemical level. Since PTEN deficiency is known to increase PI3K pathway activity and the drug combinations included an inhibitor of PI3K pathway, we initially focused on changes affecting this signaling route. We found that, as expected, the treatment with PI3Kβ inhibitor AZD8186 partially decreased the

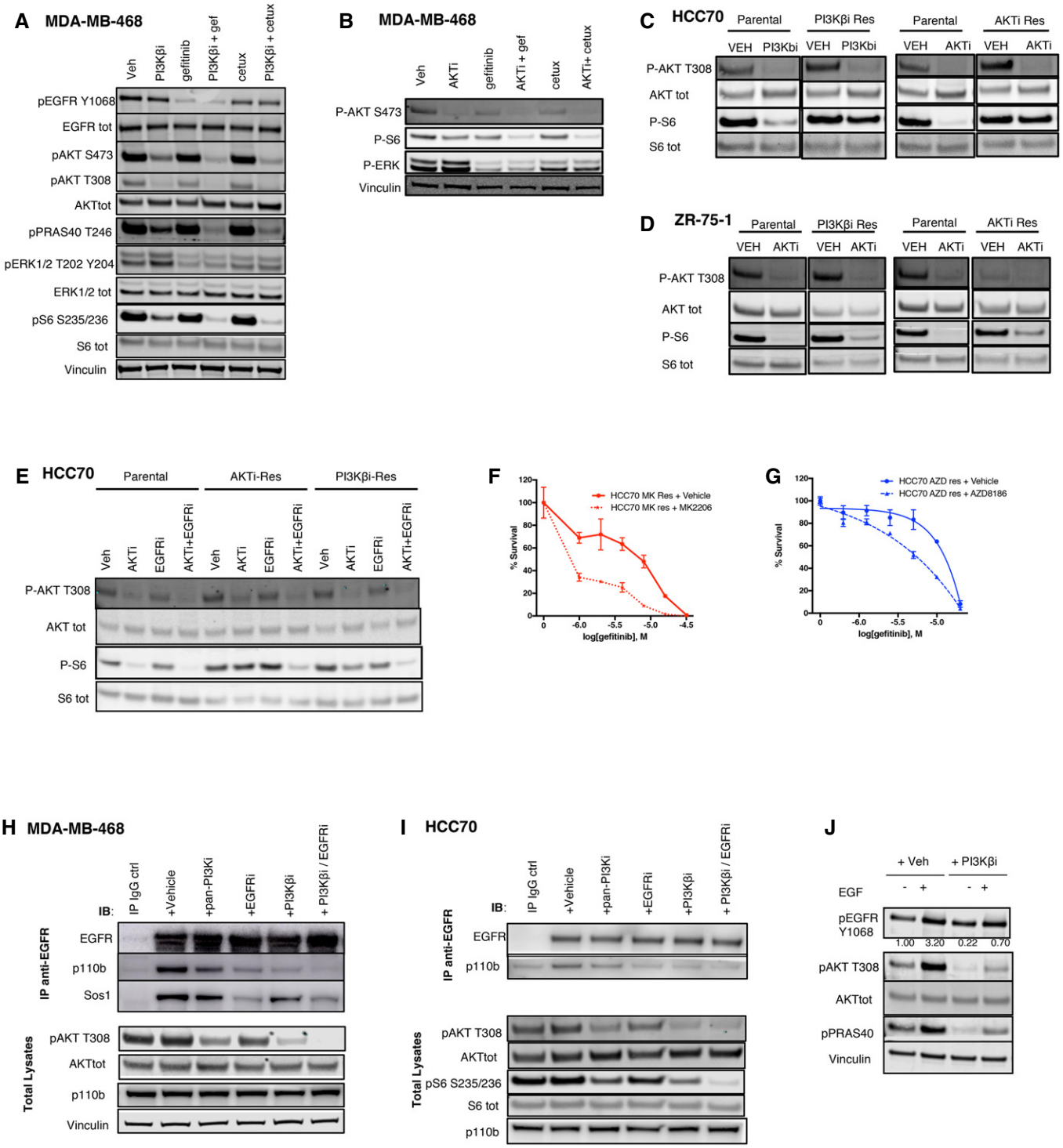

Figure 3.

Figure 3. Biochemical effects of EGFR and PI3K pathway combined inhibition.

A MDA-MB-468 cells were treated for 24 h with vehicle, PI3Kβi (AZD8186 250 nM), EGFRi (gefitinib 3 μM), or cetuximab (100 μg/ml), alone or in combination. The cell lysates were probed with the indicated antibodies.

B MDA-MB-468 cells were treated for 24 h with vehicle, AKTi (MK2206 450 nM), gefitinib (3 μM), or cetuximab (100 μg/ml), alone or in the indicated combinations. The cell lysates were probed with the indicated antibodies.

C, D HCC70 (C) and ZR-75-1 (D) parental cells or PI3Kβi-Res (derivative cells with acquired resistance to AZD8186), or AKTi-Res (acquired resistance models to MK2206) were treated with vehicle, PI3Kβi (AZD8186 250 nM), or AKTi (MK2206 1 μM) for 24 h. The whole cell lysates were then probed with the indicated antibodies. Spliced images of parental and resistant paired samples were taken from the same original blot, and blots showing P-S6 and S6 tot in (D) have been cut and reassembled for figure purposes.

E HCC70 parental, PI3Kβi-Res, or AKTi-Res cells were treated with vehicle, AKTi (MK2206 250 nM), or gefitinib (3 μM), alone or in the indicated combinations. The cell lysates were probed with the indicated antibodies.

F HCC70 MK res (acquired resistance models to MK2206) were treated with serial dilutions of gefitinib, alone, or in combination with MK2206 (810 nM), as indicated, and viability measured after 4 days of treatment. Average ± SD of triplicates and representative of two independent experiments.

G HCC70 AZD res (acquired resistance models to AZD8186) were treated with serial dilutions of gefitinib, alone, or in combination with AZD8186 (270 nM), as indicated, and viability measured after 4 days. Average ± SD of triplicates and representative of two independent experiments.

H, I p110β co-immunoprecipitates with EGFR in MDA-MB-468 (H) and in HCC70 (I). Cells were pre-treated with different inhibitors, including vehicle, pan-PI3Ki GDC0941 (1 μM for MDA-MB-468 or 0.5 μM for HCC70), EGFRi (gefitinib 3 μM), PI3Kβi (AZD8186 250 nM), or a combination of EGFRi and PI3Kβi. Cell lysates were incubated with IgG control or anti-EGFR antibody, and the immuno-complexes or the total lysates were immune-blotted with the indicated antibodies.

J EGF-induced increase in phospho-AKT is dependent on p110β kinase activity. MDA-MB-468 were starved in 0% FBS and pre-treated with vehicle or PI3Kβi (AZD8186 250 nM) for 1 h. Cell lysates were probed with the indicated antibodies. Phospho-AKT and pan-AKT bands were quantified by the use of ImageLite software: The ratio of phospho-AKT to pan-AKT normalized to the control (left hand lane) is shown.

Source data are available online for this figure.

phosphorylation of the downstream proteins AKT, PRAS40, and S6. Inhibition of EGFR reduced the levels of phospho-ERK independently of AZD8186, but only when combined with the PI3Kβ inhibitor it resulted in a more effective suppression of all the markers of PI3K pathway activation (Fig 3A). The same combination activity was observed when EGFR inhibitors were combined with the AKT inhibitor MK2206, especially at the level of the downstream marker phospho-S6 (Fig 3B). Similar biochemical effects following drug treatments were observed also in *Wap-cre:Pten$^{fl/fl}$:Tp53$^{fl/fl}$* mouse cell lines (Fig EV3A).

In order to determine whether the same changes described in cells only partially sensitive to inhibition of PI3K pathway were taking place also in models of acquired resistance, we derived drug-resistant variants from breast cancer cell lines that normally exhibit high sensitivity to PI3K inhibition *in vitro*, such as HCC70 and ZR-751. All acquired-resistant models were more resistant to PI3K pathway inhibition compared to the parental cells (Fig EV3B) and showed a less pronounced reduction in phospho-S6 following treatment with those drugs (Fig 3C and D). When EGFR inhibitors were combined with PI3K pathway inhibitors in acquired-resistant cells, we detected a stronger suppression of phospho-S6 (Fig 3E) and of cell viability (Fig 3F and G). These results suggest that some of the mechanisms that impaired the response to PI3K pathway inhibitors could be common between cell models with very different sensitivities to these drugs, including models of acquired resistance. However, in all cases the inhibition of S6 phosphorylation represented a good marker of response to treatments targeting PI3K pathway.

We also asked whether a synergistic suppression of phospho-S6 may underlie the impact on cell viability described for PI3K pathway and CK2 combined inhibition (Fig EV1I–N). We found that the simultaneous targeting of PI3Kβ and CK2, similarly to inhibition of PI3K pathway and EGFR, led to a stronger suppression of phospho-S6 (Fig EV3C). Altogether, these results enforced the notion that inhibition of phospho-S6 is a marker of response to combinatorial therapies including PI3K pathway inhibitors in PTEN-deficient triple-negative breast cancer cells.

p110β signals downstream of EGFR in PTEN-deficient triple-negative breast cancer cells

We next investigated which effectors mediated signaling downstream of EGFR in PTEN-null cells and how the interaction with those molecules was affected by drug treatments. We found that p110β, a key activator of the AKT pathway in PTEN-deficient tumor cells, co-immunoprecipitated with endogenous EGFR in two different TNBC cell lines (Figs EV3D and 3H–I). Sos1 and p110α were used as positive controls of the co-immunoprecipitation experiment, being known interactors of EGFR. The co-immunoprecipitation of EGFR and p110β was disrupted to different extents by pre-treatment with EGFR or PI3K inhibitors, while the combination between PI3Kβ and EGFR inhibitors was the most effective in impairing the interaction. This effect was mirrored by a stronger inhibition of AKT phosphorylation downstream, confirming our previous observations (Fig 3H and I). We asked whether the p110β-EGFR interaction was functional in the signaling triggered by EGFR. We observed that AZD8186 pre-treatment was able to impair both the basal and the EGF-induced phosphorylation of AKT (Fig 3J). These data demonstrate that EGFR can interact with p110β and that the activation of AKT induced by EGFR stimulation is, at least in part, dependent on p110β kinase activity in these cells. Also, effective drug-mediated inhibition of this interaction correlated with a stronger reduction in phospho-AKT and of downstream pathway activation.

We also investigated whether the synergistic reduction in PI3K pathway activity by combined PI3Kβ and EGFR inhibition was due to EGFR inhibitor's ability to suppress phospho-ERK. However, when we combined the treatment of PI3K pathway inhibitors with MEK inhibition, we did not detect any synergistic reduction in phospho-S6 (Fig EV3E), showing that the profound inhibition of phospho-S6 was more likely due to a stronger suppression of the upstream AKT activity.

Targeting G protein β and γ subunits sensitizes to EGFR and pan-PI3K inhibitors

With the aim of identifying and validating other modifiers of the response to PI3K pathway inhibitors, we carried out a CRISPR-Cas9-

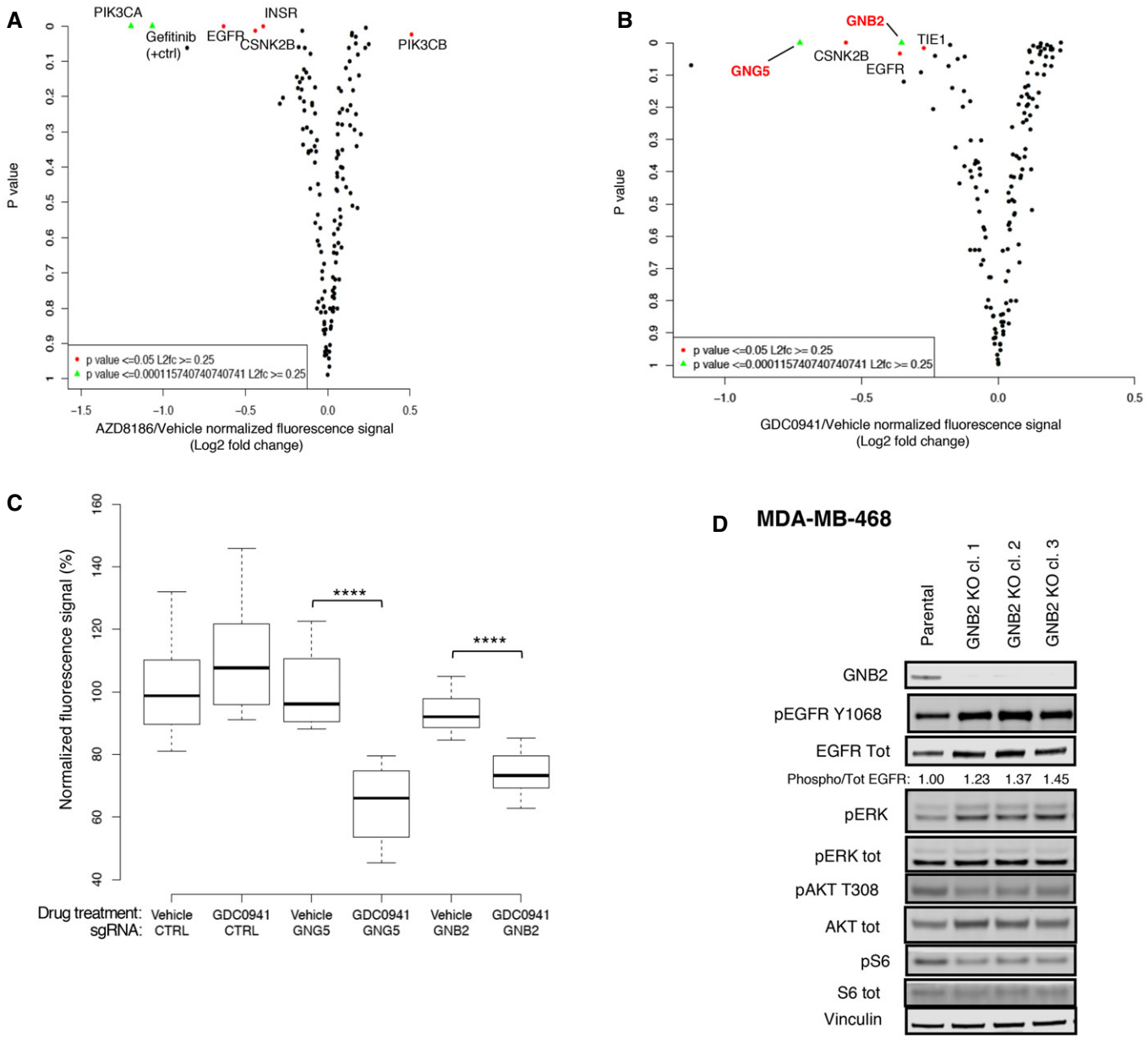

Figure 4. A CRISPR-Cas9 screening identified GNB2 as a target to potentiate the inhibition mediated by pan-PI3K inhibitor.

A, B Results of CRISPR-Cas9 screening in combination with AZD8186 100 nM (A) or GDC0941 400 nM (B). The dot-plots show for each gene knocked-out by sgRNAs the fold change (log_2) between treated conditions (AZD8186 or GDC0941, respectively) and vehicle in the fluorescence signal (anti-phosphoS6 immunofluorescence) vs the *P*-value of the difference calculated by two-sided *t*-test. The plots represent means of biological triplicates. Genes for which it was calculated a $P < 0.0001$ and Log_2 (fold change) > 0.25 are reported and highlighted in green; genes having a $0.0001 < P < 0.05$ and a Log_2 (fold change) > 0.25 are reported and shown in red. Gefitinib combined with AZD8186 represents the positive control of the experiment (A).

C Box and whisker plot showing the fold change in fluorescence signal between vehicle and GDC0941-treated conditions for MDA-MB-468 cells transduced with non-target control, GNB2, or GNG5 sgRNAs ($N = 2$ or 3). Data presented in a box and whisker plot with the central band indicating the median, the upper, and lower extremes of the box or hinge being the third and first quartiles, respectively, and the whiskers extending to the most extreme data values within 1.5 times the inter-quartile range. Statistical significance of unpaired *t*-test ****$P < 0.0001$.

D Biochemical analysis of GNB2 KO cells. Cell lysates of MDA-MB-468 parental cells and three MDA-MB-468 GNB2 KO clones were probed with the indicated antibodies. Quantification of the bands was performed by ImageLite software.

Source data are available online for this figure.

mediated targeted screen of the top candidates from the genome wide shRNA screen, testing whether the knockout of these genes sensitized MDA-MB-468 to the inhibitory activity of AZD8186, GDC0941, or MK2206. We also added to the list of candidate genes those encoding proteins that were found to be regulated by AZD8186 treatment in MDA-MB-468 using a reverse-phase protein

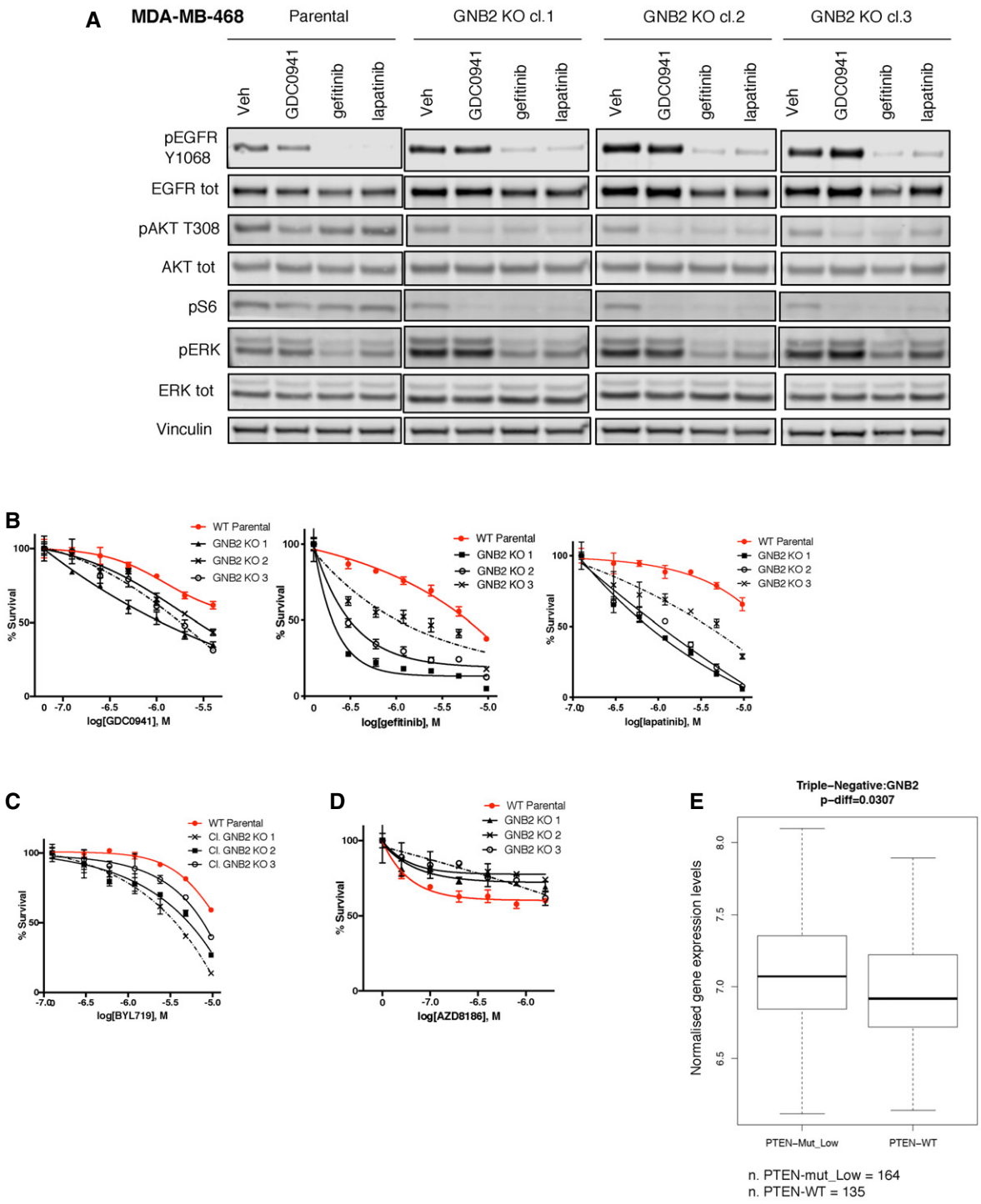

Figure 5. GNB2 KO modifies the sensitivity to different inhibitors of EGFR-PI3K pathway.

A MDA-MB-468 parental cells and three MDA-MB-468 GNB2 KO clones were treated with vehicle, GDC0941 1 μM, gefitinib 3 μM, or lapatinib 1 μM for 24 h. The cell lysates were probed with the indicated antibodies.

B–D Viability assays of MDA-MB-468 parental cells and three MDA-MB-468 GNB2 KO clones treated with serial dilutions of the indicated drugs for 6 days. Mean ± SD of triplicates and representative of two or three independent experiments.

E Patient samples from METABRIC dataset classified as TNBCs (N = 299) were assigned to the groups "PTEN-low" when falling in the lower quartile for PTEN expression, "PTEN-mut" when harboring a non-synonymous mutation on PTEN gene, "PTEN-WT" in all other cases. Comparison of the expression of GNB2 between the PTEN low or mut and the PTEN-WT groups. Box and whisker plot (Median/IQR/1.5*IQR Whiskers). P-value calculated by unpaired t-test.

Source data are available online for this figure.

array (RPPA, Fig EV4A). We hypothesized, indeed, that some of these proteins may have a functional role in defining the response to PI3K pathway inhibitors. The list included overall 141 genes, of which 31 were from the RPPA data and 110 from the shRNA screen (Materials and Methods and Table EV2).

In order to perform the CRISPR-Cas9 screen, we derived and characterized a single-cell clone from an MDA-MB-468 population harboring a doxycycline-inducible expression vector for Cas9 (Fig EV4B–D). Given the importance of phospho-S6 inhibition as a marker of response to combinatorial drug regimens, we used the measurement of phospho-S6 by immuno-fluorescence as a readout of the screen. The screening was performed in an arrayed format, and each gene was efficiently targeted by a combination of 4–5 different sgRNAs (Fig EV4E–H). Plotting of the raw phospho-S6 signal from individual experiments showed overall consistent values among replicates in different treatment conditions (Fig EV4I), confirming the quality of the screening data.

The CRISPR-Cas9 screen in combination with AZD8186 confirmed our previous results, showing enhanced suppression of phospho-S6 by the combined treatment with AZD8186 and the KO of EGFR or CSNK2B (Fig 4A). Also, the KO of PIK3CA (encoding PI3K p110α) potentiated the effect of the PI3Kβ inhibitor. This confirmed data from previous literature that showed how simultaneous inhibition of both p110α and p110β exerted synergistic effect on PTEN-null cancer cells (Schwartz *et al*, 2015). On the other hand, knockout of PIK3CB, encoding PI3K p110β, the target of AZD8186, abolished the effect of the drug on phospho-S6 and provided a further validation to our approach.

Interestingly, two genes encoding for G protein β and γ subunits, GNB2 and GNG5, respectively, ranked among the top cooperative partners of GDC0941 when they were knocked-out (Fig 4B and C). In order to investigate the mechanistic basis of this interplay, we isolated GNB2 KO clones by immunofluorescence-based detection of GNB2 protein levels (Fig EV4K) and we compared signaling in the KO cells with parental MDA-MB-468 cells (Fig 4D). We found that the KO clones had an increased phosphorylation and expression of EGFR compared to the WT counterpart and they showed also an increased ratio between phosphorylated and total EGFR, suggesting a compensatory increase in EGFR activity. This finding was supported by the increased basal phosphorylation of the downstream effector ERK1/2. Also, we observed that markers of PI3K pathway activity such as phospho-AKT or phospho-S6 were decreased by the KO of GNB2, showing that this protein had an impact on the basal activation of this pathway. We then treated WT and GNB2 KO cells with GDC0941, and we observed a stronger and prolonged suppression of phospho-AKT and phospho-S6 in the KO clones compared to WT cells (Figs EV5A and 5A), validating the results of the CRISPR-Cas9 screening. Downregulation of the basal PI3K signaling and increased sensitivity to the GDC0941-mediated suppression of phospho-S6 was also observed in an independent TNBC cell line following the KO of GNB2 (Fig EV5B).

Interestingly, the increased activity of EGFR in cells lacking GNB2 was mirrored by a stronger suppression of PI3K signaling following EGFR inhibition by gefitinib or lapatinib (Fig 5A). As expected, also in viability assays GNB2 KO clones showed increased sensitivity to both GDC0941 and EGFR or HER family inhibitors, demonstrating a shift in the addiction to EGFR-PI3K axis following the disruption of G protein signaling (Fig 5B).

We asked then which PI3K isoform signals downstream EGFR to guarantee the survival of the cells in the absence of GNB2. We found that the KO of GNB2 increased the dependence of the cells on p110α compared to the WT counterpart, as demonstrated by treatment of WT and GNB2 KO cells with the p110α-specific inhibitor BYL719 (Fig 5C). GNB2 loss, on the other hand, partially relieved the dependence of PTEN-null cells on p110β (Fig 5D), and this shift was supported at the biochemical level by the differential impact of PI3K isoform-specific inhibitors on the phosphorylation of AKT and S6 downstream EGFR in WT or GNB2-deficient cells (Fig EV5C).

As both PI3K isoforms were partially involved in supporting the survival and the activation of PI3K pathway downstream EGFR in the absence of GNB2, these results explained the increased sensitivity of GNB2 KO cells to pan-PI3K inhibitors. The basal down-regulation of PI3K pathway activity and the shift in dependence following GNB2 inactivation from p110β to EGFR and to other downstream non-p110β effectors, such as p110α, are in line with the accepted notion that βγ subunits of G proteins are responsible for the activation of PI3Kβ (Kurosu *et al*, 1997) and suggested that this arm of the pathway can operate in parallel with EGFR to support the activation of AKT.

Altogether, these data suggested that both the βγ subunits of G proteins and EGFR can signal to AKT through PI3Kβ and that those two arms of the pathway can compensate each other when PI3K inhibitors are employed to treat PTEN-deficient TNBC cells.

We investigated the relevance of these findings in patients by analyzing the expression of GNB2 in TNBC samples divided according to their PTEN status in the METABRIC dataset. Consistent with the importance of G protein signaling in the PTEN-null context, we found statistically significant higher expression of GNB2 in samples characterized by low expression or non-synonymous mutation of PTEN compared to the PTEN-WT subgroup (Fig 5E).

PAR1 signals to AKT through the βγ subunits of G proteins

Since we identified G protein βγ subunits as important activators of the PI3K pathway in PTEN-null cells, we asked which G protein-coupled receptors (GPCRs) can activate G protein signaling in these cells. Assuming that the inhibition of any GPCR acting upstream of the βγ subunits of G proteins in these cells should reproduce the phenotype described after knocking out the downstream effector GNB2, we tested a library of compounds targeting GPCRs for their ability to suppress phospho-S6 in combination with GDC0941 or lapatinib. From the drug screening, we identified as a top candidate vorapaxar, a thrombin-receptor PAR1 inhibitor used as anti-thrombotic agent (Figs 6A and EV5D). Biochemical analysis confirmed the increased phosphorylation of EGFR induced by PAR1 inhibition and a stronger suppression of phospho-AKT and phospho-S6 when vorapaxar was combined with GDC0941 or lapatinib (Fig 6B), phenocopying the phenomenon previously observed in the same cells as a consequence of GNB2 inactivation.

To formally prove that PAR1 could activate AKT through the β subunit of G proteins in these PTEN-null cells, we tested the induction of phospho-AKT after treatment with control or PAR1-agonist peptides in WT and GNB2 KO cells (Fig 6C). While in the WT MDA-MB-468 cells, the agonist was able to increase the phosphorylation

of AKT and ERK compared to control, no activation of these downstream nodes was detected in GNB2 KO cells, demonstrating that GNB2 was necessary for the PAR1 stimulating signal to be transduced. Also, we confirmed the on-target effect of vorapaxar, since the co-treatment with the drug abrogated the increase in phospho-AKT induced by the agonist peptide in WT cells. We then

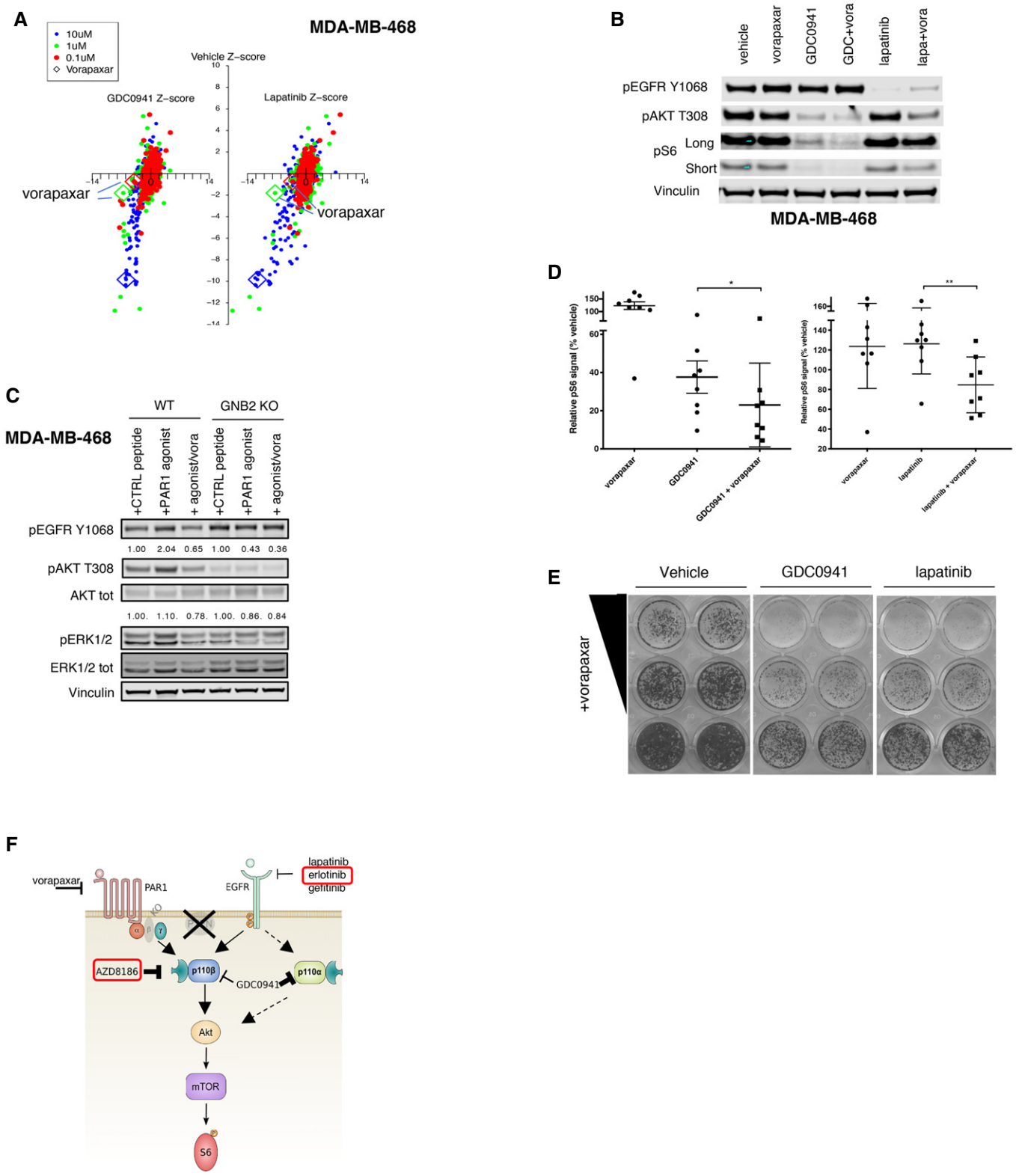

Figure 6.

Figure 6. PAR1 signals through GNB2 to sustain the activation of PI3K pathway in the presence of PI3K or HER inhibitors.

A Schematic of the results from the drug screening with compounds targeting GPCR signaling. MDA-MB-468 cells were treated with the compounds of the GPCR-targeted library at three different concentrations (0.1, 1, or 10 μM) in combination with vehicle, GDC0941 450 nM, or lapatinib 1 μM. The pS6 signal was measured by IF after 24 h of treatment and normalized to DAPI. Z scores of the normalized fluorescence values for each drug measured in the presence of vehicle, GDC0941, or lapatinib are reported on the *y*-axis or on the left or right *x*-axis of the dot-plot, respectively. Readings acquired following treatment with the three different concentrations of the GPCR-targeted drugs are reported in three different colors. Dots corresponding to vorapaxar treatments at the three different concentrations are highlighted in the plot. The values reported are mean of a biological triplicate of the experiment.

B MDA-MB-468 was treated for 24 h with vehicle, vorapaxar (10 μM), GDC0941 (1 μM), or lapatinib (1 μM) alone or in the indicated combinations. The cell lysates were probed with the indicated antibodies.

C MDA-MB-468 parental cells or GNB2 KO clones were starved and treated with scramble or PAR1 activating peptide for 5 min, alone or in combination with vorapaxar. The cell lysates were probed with the indicated antibodies. Phospho-AKT, pan-AKT, phospho-ERK1/2, and pan-ERK1/2 bands were quantified by the use of ImageLite software: The ratio of phospho-AKT to pan-AKT and phospho-ERK1/2 to pan-ERK1/2 normalized to the control peptide-treated conditions for WT and GNB2 KO cells (first and fourth lanes, respectively) is shown.

D p-S6/loading control signal from Western blot experiments in which a panel of six TNBC PTEN-null cell lines and HCC70 cells that acquired resistance to AZD8186 or MK2206 were treated with vehicle, vorapaxar (10 μM), GDC0941 (1 μM), or lapatinib (1 μM) alone or in the indicated combinations. The values were normalized to vehicle treatment for all cell lines. Mean of 2 independent experiments ± SD. *P*-values calculated by two-tailed paired student *t*-test $*P = 0.0235$ and $**P = 0.002$. Cell lines used in the experiments were as follows: MDA-MB-468, HCC70, HCC1937, HCC38, HCC1395, BT-549, HCC70 AZD8186-resistant, and HCC70 MK2206-resistant.

E Long-term proliferation assay of MDA-MB-468 cells treated with vorapaxar (5 or 2.5 μM), GDC0941 (1 μM), or lapatinib (1 μM), alone or in the indicated combinations. Cells were treated for 2 weeks and stained by crystal violet. One representative experiment of three is shown.

F Schematic of the network controlling the phosphorylation of AKT and S6 in PTEN-null TNBC cells. EGFR and PAR1-βγ subunits of G protein signal in parallel to p110β and AKT. The two arms of the pathways are inter-connected by feedback compensation mechanisms that act when any of the two signals is perturbed. Combined targeting of both the signaling arms results in a sustained inhibition of the downstream pathway. Erlotinib (EGFR inhibitor) and AZD8186 (p110β inhibitor) are highlighted in the figure as these drugs proved effective in *in vivo* experiments.

Source data are available online for this figure.

extended our findings employing a panel of PTEN-null TNBC cell lines, and we found that the combinatorial treatment of vorapaxar and GDC0941 or lapatinib led to an improved inhibition of the levels of phospho-S6 in multiple cell models (Fig 6D). We also observed a cooperative inhibition in cell viability by the simultaneous treatment of vorapaxar and pan-PI3K or HER inhibitor (Fig 6E).

These data reveal a new element in the signaling cascade that operates in PTEN-null TNBCs and suggest that the GPCR-PAR1 signals upstream of G protein βγ subunits to sustain the activation of AKT.

The results above describe a signaling network in PTEN-deficient TNBC that underlies the sustained activation of the PI3K pathway and relies on two signaling branches. The first upstream activator branch is EGFR family receptor tyrosine kinases, while the second is GPCRs, among which we identified the thrombin receptor PAR1, that in turn activate G proteins, including their βγ subunits. Both axes feed into the activation of PI3Kβ isoform and can compensate each other also through the engagement of different effectors, such as PI3Kα, to overcome the blockade of PI3K pathway and support the phosphorylation of the signaling node AKT and of the downstream marker S6 (Fig 6F).

Discussion

PTEN deficiency is one of the most common alterations found in human cancers and in triple-negative breast cancers. Given the frequency of the disease in the population (Cancer Research UK statistics 2015 https://www.cancerresearchuk.org/health-professional/cancer-statistics/statistics-by-cancer-type/breast-cancer) and the frequency of PTEN alterations in this type of tumor (Cancer Genome Atlas Network, 2012), we can estimate that up to 15,000 patients may be diagnosed every year in the United States and 22,000 per year in the European Union with a PTEN-deficient triple-negative invasive breast cancer.

PTEN loss results in increased activation of PI3K (Stambolic *et al*, 1998; Haddadi *et al*, 2018) and addiction to PI3K pathway activity (Chen *et al*, 2006; Jia *et al*, 2008; Wee *et al*, 2008; Vasudevan *et al*, 2009; Sangai *et al*, 2012; Hancox *et al*, 2015) in the affected cells. Also, RAS mutations, that are known to confer resistance to a number of therapies (Konieczkowski *et al*, 2018) and to modify the profile of dependencies to PI3K isoform-specific inhibitors (Schmit *et al*, 2014), rarely occur in these tumors. The known biochemical properties of PTEN-deficient cells, both from preclinical models and analysis of the genetic make-up of these tumors from patients, make PI3K pathway inhibition one of the most appealing approaches for the targeting of triple-negative PTEN-null breast cancers.

However, no clear evidence of benefit for PTEN-null cancer patients treated with PI3K inhibitors in clinics has been reported to date (Kim *et al*, 2017; Martin *et al*, 2017) and, despite the urgent need of a targeted treatment for this subset of poor prognosis patients, the molecular bases for the lack of efficacy of those therapies are still poorly understood.

We describe here a signaling network that relies on EGFR and GPCR activity, converges on the activation of PI3Kβ and operates prevalently in PTEN-null breast tumor cells. Inhibition of the GPCR-PI3Kβ axis leads to a rebound in the activity of EGFR and other non-PI3Kβ downstream effectors, such as PI3Kα, to sustain the activation of the pathway. These findings are in line with previous reports showing that the use of combined pan-PI3K class I and EGFR inhibitors produced synergistic responses in basal-like breast cancers (She *et al*, 2016) and that inhibition of PI3Kβ relieves a feedback activation of PI3Kα (Schwartz *et al*, 2015), and they add another piece of information to the complex network that allows PTEN-null breast cancer cells to survive PI3K pathway inhibition. We have translated a deeper knowledge of the signaling into new potential therapeutic strategies, suggesting that PI3Kβ is a good target for inhibition combined with EGFR inhibitor in this tumor type.

EGFR is amplified or overexpressed in a high percentage of triple-negative breast cancers and more frequently than in other

types of breast cancers (Reis-Filho & Tutt, 2008) (Reis-Filho *et al*, 2006; Reis-Filho & Tutt, 2008; Gumuskaya *et al*, 2010; Shao *et al*, 2011; Martin *et al*, 2012; Park *et al*, 2014; Nakai *et al*, 2016). This further emphasizes the importance of this receptor in the biology of these tumors. Given the frequency of its aberrations, EGFR represents an appealing target for inhibition in this type of cancer. However, anti-EGFR therapies tested in clinical trials as monotherapy on triple-negative breast cancers failed to produce beneficial results (von Minckwitz *et al*, 2005; Dickler *et al*, 2008; Carey *et al*, 2012; Yardley *et al*, 2016). The high prevalence of alterations targeting components of pathways downstream EGFR, such as PTEN, and compensatory feedback signals like the one we report here, may provide a molecular framework to explain such failures.

We have shown that the use of anti-PI3Kβ and anti-EGFR therapies shows an enhanced combination effect in PTEN-null cells. The application of this therapeutic strategy may result in a higher selectivity against the PTEN-deficient tumor cells relative to PTEN wild-type cells and, therefore, in a wider therapeutic window of the treatments compared to the more complete inhibition of different points on the PI3K pathway by a pan-PI3K, AKT, or mTOR inhibitor. This new combinatorial therapy includes drugs that are approved for use in cancer treatment, like anti-EGFR therapies, or that are currently in clinical trials, like PI3Kβ inhibitors, making these findings easier to translate in the clinical practice. Indeed, toxic effects associated with on-target inhibition of PI3Kα, such as hyperglycemia (Bendell *et al*, 2012), and the related compensatory release of insulin by the pancreas, that in turn can promote resistance to PI3K inhibition by reactivation of insulin signaling in cancer cells (Hopkins *et al*, 2018), may be limited by the specific targeting of the β isoform of PI3K. Hyperglycemia has not been reported to be among the adverse effects of AZD8186 treatment (Lillian *et al*, 2016).

In the current study, we used AZD8186 as a PI3Kβ inhibitor. AZD8186 was reported to have higher activity on p110β (IC50 = 4 nM) and p110δ (IC50 = 12 nM), compared to p110α (IC50 = 35 nM) or p110γ (IC50 = 675 nM). We showed that AZD8186 exerted its anti-tumor function *in vitro* due to PI3Kβ inhibition, since PTEN-null TNBC cells do not express appreciable levels of p110δ and the specific inhibition of p110α in combination with EGFR did not produce the same effects. These results confirmed previous evidence showing AZD8186 to selectively target the β over the α isoform of PI3K in breast cancer cells (Schwartz *et al*, 2015). We cannot formally rule out the possibility that AZD8186 may have some function *in vivo* related to inhibition of p110δ, especially in immune cells, that are known to express high levels of this protein. However, the likelihood that the response observed *in vivo* may be due to interference with the immune-compartment by AZD8186 is low, since results have been confirmed in different models and in both immune-competent and immune-deficient recipients.

We report here that GPCRs, and in particular PAR1, are responsible for the activation of PI3Kβ and for the sustained activity of PI3K pathway also in the presence of EGFR inhibitors. PAR1 is one of the four members of the protease-activated receptors (PARs) GPCR family and is activated by thrombin and by a variety of other tumor-associated proteases, including plasmin and MMP-1 (Boire *et al*, 2005). Indeed, PAR1 expression has been positively correlated with carcinoma cell invasiveness (Even-Ram *et al*, 1998) and its altered trafficking and persistent signaling was shown to promote breast cancer invasion (Booden *et al*, 2004).

PAR1 and EGFR pathways have been previously functionally linked. PAR1 was reported to transactivate EGFR not only in vascular smooth muscle cells (Kanda *et al*, 2001) and in cardiac fibroblasts (Sabri *et al*, 2002), but also in colorectal (Darmoul *et al*, 2004) and in breast cancers (Arora *et al*, 2008) through a variety of different mechanisms, showing that the two pathways can reciprocally influence their activities. Also, a role for PI3Kβ in mediating the synergistic production of PIP_3 and activation of AKT in response to both GPCR and RTK inputs has been shown (Kurosu *et al*, 1997; Murga *et al*, 2000; Ciraolo *et al*, 2008; Hauser *et al*, 2017) and this provides a molecular framework to our observation that EGFR and PAR1 can simultaneously signal through PI3Kβ in triple-negative breast cancers. Our data describe how those two branches of the pathway can compensate each other following PI3K inhibition and place this GPCR-RTK signaling network at the centre of a mechanism of drug resistance. The stronger suppression of basal PI3K pathway activity induced by GNB2 inactivation compared to PAR1 inhibition suggests the possibility that other GPCRs in addition to PAR1 may contribute to the signaling to PI3Kβ in these cells. Among other GPCRs that might be involved in this pathway, GPER1 could be a possible candidate, as it was previously shown to mediate signaling from 17beta-estradiol to βγ subunits of G protein and transactivation of EGFR in ER-negative breast cancers (Filardo *et al*, 2000).

However, our data demonstrate a role of PAR1 in mediating resistance to PI3K and EGFR inhibitors and suggest that GPCRs may represent important drivers of drug resistance also in other contexts. Since GPCR drug discovery has been an area of intense activity (Hauser *et al*, 2017), we envision that these findings may have significant potential for translation.

In addition to implicating GPCR signaling, our study also highlighted an unexpected role of CK2 inhibition in potentiating the activity of PI3K pathway inhibitors in PTEN-null TNBC cells. Previous work showed that PTEN deletion affects levels of CK2 through transcriptional STAT3-mediated upregulation (Kalathur *et al*, 2015), suggesting that this protein may have an important role in PTEN-null tumor cells. CK2 is in turn known to phosphorylate AKT in Ser129 and to contribute to its activation (Di Maira *et al*, 2005), providing a molecular framework to its role in limiting response to PI3K pathway inhibitors. It has also been reported that suppression of PI3K-AKT-mTOR pathway was enhanced by combined targeting of EGFR and CK2 in lung cancer models relying on EGFR activity (Bliesath *et al*, 2012). CK2 could thus expand the array of potential drug targets for the design of combinatorial treatments in PTEN-null TNBCs beyond EGFR and PI3Kβ.

Materials and Methods

Cell lines

MDA-MB-468, BT-549, U-251, A172, U-87-MG, BT-20, MDA-MB-231, and MDA-MB-361 were maintained in DMEM supplemented with 10% FBS. MCF7 were maintained in DMEM supplemented with 10% FBS and Insulin Human Solution 1:1,000 (I9278 Sigma Aldrich). T47D were maintained in RPMI with 10% FBS and Insulin Human Solution 1:1,000. Cell lines derived from mouse primary mammary gland tumors were established in medium consisting of DMEM/F12 Glutamax (Thermofisher), 10% FBS

heat-inactivated, 1:1,000 dilution of Insulin solution, and EGF 20 μg/ml, and they were cultivated on collagen solution-coated plates. After 10 passages, cells were adapted to grow in DMEM 10% FBS and on normal tissue culture plates. HCC70 and ZR-75-1 acquired resistance models were maintained in RPMI supplemented with 10% FBS and AZD8186 250 nM or MK2206 1 μM. The rest of the cell lines were cultured in RPMI with 10% FBS. Cell lines were tested for mycoplasma and were authenticated by short-tandem repeat (STR) DNA profiling by the Francis Crick Institute Cell Services facility.

Compounds and reagents

AZD8186 was obtained from a collaboration with AstraZeneca. Gefitinib, erlotinib, lapatinib, GDC0941, MK2206, and vorapaxar were purchased from Selleckchem. CX-4945 was obtained from MedChemExpress. Cetuximab was a kind gift from Charles Swanton.

The library of compound targeting GPCR signaling was purchased from MedChemExpress (HY-L006).

Antibodies for immunoblots purchased from Cell Signaling Technology were as follows: anti-phospho-EGFR Y1068 (Cat# 3777, dilution 1:1,000), EGFR (Cat# 4267, dilution 1:1,000), phospho-AKT T308 (Cat# 13038, dilution 1:1,000), S473 (Cat# 9271, dilution 1:1,000) and S129(Cat#13461, dilution 1:1,000), AKT (Cat# 2920, dilution 1:1,000), phospho-ERK T202/Y204 (Cat# 9101, dilution 1:1,000), ERK (Cat# 9107, dilution 1:2,000), phospho-S6 S235/236 (Cat# 2211, dilution 1:4,000), S6 (Cat# 2317, dilution 1:500), phospho-PRAS40 T246 (Cat# 2640, dilution 1:1,000), PTEN (Cat#9559, dilution 1:1,000), p110α (Cat# 4249, dilution 1:400), and p110β (Cat# 3011, dilution 1:1,000). Anti-vinculin was from Sigma-Aldrich (Cat# V4505, dilution 1:5,000). Anti-GNB2 (ab81272, dilution 1:1,000) was from Abcam and anti-Sos1 from Santa Cruz Biotechnology (sc-17793, dilution 1:1,000). Anti-EGFR1 (from Francis Crick Institute Cell Service) was used in the Immuno-precipitation experiments (5 μg antibody/1 mg protein).

pLenti_BSD_sgRNA plasmid was a generous gift of Paola Scaffidi, and it was generated through replacement of GFP cassette with BSD cassette into the pLenti-sgRNA-Lib from Wei lab (Addgene Plasmid #53121). pCW-Cas9 vector generated in David Sabatini's lab was obtained from Addgene (#50661).

In vivo studies

All studies were performed under a UK Home office approved project license and in accordance with institutional welfare guidelines.

Wap-cre:Pten$^{fl/fl}$:Tp53$^{fl/fl}$ mouse model was generated crossing the Trp53$^{tm1Brn/tm1Brn}$ (NCI Mouse Repository) and the Pten$^{tm1Hwu/tm1Hwu}$ lines, previously back-crossed in C57BL/6 background, with the Wap-cre strain generated in C57BL/6 background by the NCI Mouse Repository.

Female mice were allowed to breed and wean their pups in order to activate the expression of Cre transgene. After that, mice were monitored for mammary tumor growth. Tumors were measured using caliper, and volume was estimated using the formula width^2 × length × 0.5. Before the tumors reached the size-limit imposed by the project license, mice were culled and the mammary tumor extracted.

For human cell line *in vivo* studies, 5 million cells were re-suspended in PBS mixed 1:1 with growth-factor-reduced Matrigel and injected into the fat pad of the left, fourth mammary gland of 6- to 8-week-old female NU(NCr)-Foxn1^{nu} (Charles River). Tumor volumes were determined using the formula width^2 × length × 0.5. When tumors reached a volume of 100 or 250 mm^3, mice were randomly assigned to treatment with vehicle or drugs.

For spontaneous tumor-derived cell lines, 5–10 millions of cells were re-suspended in 1:1 PBS: growth-factor-reduced Matrigel and injected into the fat pad of the left, fourth mammary gland of 6- to 8-week-old female C57BL/6 mice.

For *in vivo* drug treatments, AZD8186 was formulated in 0.5% (hydroxypropyl) methyl-cellulose/0.2% Tween-80 and administered by oral gavage (5 μl/g) every day. Erlotinib was prepared in 0.3% (hydroxypropyl) methyl-cellulose and administered intra-peritoneum every day at 5 μl/g.

shRNA screening

Whole-genome shRNA was performed using the MISSION LentiPlex Pooled shRNA library from Sigma (SHPH01). The library contains 80717 shRNA constructs from the TRC collection targeting around 16,000 genes and is divided into 10 different pools, which were infected and sequenced separately.

MDA-MB-468 cells were infected in triplicate with the ready-to-use lentivirus in the presence of 8 μg/ml polybrene at a multiplicity of infection MOI = 0.8 and at an initial representation of 800 cells for each shRNA. Forty-eight hours after the infection, cells were selected in 2 μg/ml puromycin for 48 h, followed by 24-h growth with fresh media. Then, cells were divided into five different aliquots. One aliquot was frozen to measure the initial shRNA representation (time = 0). The other four aliquots were seeded in 15-cm dishes, and the day after cells were treated with either DMSO, 250 nM AZD8186, 250 nM GDC0941, or 450 nM MK2206. Drugs were replaced every 3 days of treatment and cells passaged after 6 days treatment keeping a representation of 400. After another cycle of 6 days of treatment, cells were trypsinized, counted to measure the efficiency of the treatment, and frozen. Also the genomic DNA extraction and the PCR detailed below were done in order to keep a 400 representation of each shRNA.

Genomic DNA was isolated from all the samples using Wizard genomic DNA purification kit (Promega). shRNA inserts were retrieved from the genomic DNA by PCR amplification using the following conditions: (i) 98°C, 30 s; (ii) 98°C, 10 s; (iii) 60°C, 20 s; (iv) 72°C, 1 min; (v) to step 2, 16, or 11 cycles (for PCR1 or PCR2, respectively); 72°C, 5 min. Indexes and adaptors for deep sequencing (Illumina) were incorporated in the PCR primers. For PCR1, gDNA was amplified using Illuseq_x_PLKO1_f ACACTC TTTCCCTACACGACGCTCTTCCGATCTxxxxxx CTTGTGGAAAGGA CGAAACACCGG (where x indicates different barcodes) and P7_pLKO1_r CAAGCAGAAGACGGCATACGAGATTTCTTTCCCCTG CACTGTACCC primers. 2.5 μl of PCR1 product was used as templates for PCR2 reaction, together with P5_IlluSeq AATGATA CGGCGACCACCGAGATCTACACTCTTTCCCTACACGACGCTCTTCC GATCT and P7 CAAGCAGAAGACGGCATACGAGAT primers. Final PCR product was purified using MiniElute PCR Cleanup (Qiagen) and quantified using Bioanalyzer. Finally, shRNA representation for each sample was measured by next-generation sequencing

(Illumina). The shRNA sequences were extracted from the sequencing reads and aligned to TRC library. Due to the customized vector structure, samples pooled into the same sequencing lane could not be demultiplexed with the standard Illumina pipeline. As such, in-house software was used to recognize the first six nucleotides of each read as the barcode, and nucleotides 31–53 as the shRNA sequence. Each sample was then collapsed to "tags", so that each unique sequence was represented in the file only once, along with a count of the total number of times it was detected. These tag files were then mapped to the TRC library sequences using bwa 0.5.9 (Li & Durbin, 2009) with –n 4, -k 4, -l 90 (i.e., seed length > read lengths and maximum mismatches = 4). Counts of the number of times each sequence within the targeted pools was detected (taking into account the count associated with each tag) were then summarized with off-target reads discarded. shRNAs not represented by at least 50 reads in each sample were removed at this stage. Counts were then normalized to the maximum total number of aligned reads across all samples for that pool. Comparisons were performed by considering the mean fold change across triplicates, with *P*-value calculated by a paired *t*-test on these log values. The following criteria were applied to filter genes. At least one shRNA associated with a mean ratio of absolute counts between drug treatment and vehicle ≤ 0.65 with a *t*-test *P*-value between triplicates ≤ 0.15; at least one shRNA associated with a mean ratio of absolute counts between drug treatment and vehicle ≤ 0.75 with a *t*-test *P*-value between triplicates ≤ 0.15; and mean ratio of absolute counts between vehicle and time $0 > 0.5$. Filtered genes were then ranked based on the lowest mean ratio of absolute counts between drug treatment and vehicle for the shRNA associated with the second lowest ratio for each gene (Table EV1).

CRISPR-Cas9 library generation

Ninety-six candidates were selected among the 163 genes for which at least two different shRNAs showed mean ratio of absolute counts treatment/vehicle ≤ 0.5 in the shRNA screening (Table EV1).

In addition, we included genes codifying for epitopes that were down- or up-regulated by AZD8186 treatment in the RPPA analysis by a Log_2 Fold change ≥ 0.25 and with a *P*-value ≤ 0.05 at any time point.

Based on biological interest, we also included some genes at the edge of inclusion criteria (reported in Table EV2 not in bold), PIK3CA (as a positive control based on previous publications) and we excluded AKT, S6, NDRG1, and PRAS40.

Four or five not-overlapping sgRNA sequences were selected for each of those genes from the list reported in Wang *et al* (2015) and synthesized (Sigma-Aldrich) with forward strand 5′ overhang -ACCG and reverse strand 5′ overhang –AAAC. Forward and reverse strands of the oligos were annealed and ligated by Golden Gate Assembly into the pLenti_BSD_sgRNA plasmid, as previously described (Zhou *et al*, 2014), with minor modifications. Briefly, the annealing was performed incubating forward and reverse primers at 10 μM each (final concentration) in PNK 1× buffer at 95°C for 5 min, and then, the temperature was ramped to 25°C at 0.1°C per second. Two microliter of the annealed primer solution diluted 1:200 was used in the Golden Gate assembly reaction together with BsmBI (five units), pLenti_BSD_sgRNA (50 ng), T7 DNA ligase (1,500 units), T4 ligase buffer with ATP (diluted to 1×) up to 10 μl final volume for each reaction. The following conditions were used as follows: 25 cycles of 45°C for 2 min and 20°C for 2 min, then 60°C for 10 min, and 80°C for 10 min.

Ligated vectors were transformed by heat-shock in Stbl3 competent E. Coli bacteria (one vector in each well of 96-multi-well plates). Bacteria were grown overnight in 96-deep-well plates, and after growth, bacteria transformed by sgRNA vectors targeting the same gene were pooled together before plasmid extraction (Qiagen QIAprep Spin Miniprep Columns). Lentiviral particles were produced in arrayed format by transfecting HEK293T cells in 12-well tissue culture plates with 67.6 ng pCMV-VSVG, 203 ng pCMV-8.2 (Addgene), and 270 ng pLenti_sgRNA vector mixture for each gene in separated wells (Lipofectamine, Invitrogen). Forty-eight hours after transfection, virus particles in the supernatant were harvested and stored at −80°C in 96 well plates.

CRISPR-Cas9 KO screening

An MDA-MB-468 clone expressing a DOX-inducible form of Cas9 was derived by transduction of the parental cells with pCW-Cas9 lentivirus. Infected cells were selected by hygromycin B (ThermoFisher Scientific, final concentration 200 μg/ml) and single-cell cloned in 96-well tissue culture plates.

MDA-MB-468 iCas9-cloned cells were seeded at 10,000 cells/well in 24-well plates and infected in array format with the pLenti_BSD_sgRNA library in the presence of polybrene 8 μg/ml (200 μl viral supernatant/well). Cells were selected with blasticidin S for 5 days (ThermoFisher Scientific, final concentration 5 μg/ml). After selection, cell numbers were extrapolated by counting cells in three wells and by comparing their Cell Titer Blue Viability assay (Promega) readings with the readings of all other samples. Cells were seeded at 50,000 cells/well in 12-well plates and treated with 1 μg/ml doxycycline for 4 days. After that, cells were counted as previously described and passaged in equal numbers in wells of similar size before being treated for 4 days by doxycycline. Cells were counted again and seeded at a density of 4,000/wells in 96-well black plates before being treated with vehicle, AZD8186 100 nM, GDC0941 400 nM, or MK2206 450 nM in technical quadruplicate. After 30 h of treatment, cells were fixed in 96-well black plates by 4% formaldehyde (15 min of incubation), washed three times in PBS, blocked 1 h in 1× PBS/5% normal serum (Cell Signaling Technology)/0.3% Triton X-100 (Sigma-Aldrich), and incubated overnight in antibody dilution solution (1× PBS/1% BSA/0.3% Triton™ X-100) containing anti-phospho S6 S240/244 antibody (Cell Signaling Technology Cat#5364) diluted 1:1,200. Plates were then washed three times in PBS and incubated for 1 h in antibody dilution solution containing Anti-rabbit IgG Alexa Fluor-488 Conjugate (Cell Signaling Technology #4412) diluted 1:1,000 and DAPI 0.2 μg/ml. Plates were washed three times in PBS, and images were acquired and signal quantified using CX7 LZR high content microscope (ThermoFisher Scientific). The fluorescent signal from each well was normalized to DAPI.

All washing steps of 96-well plates were performed by 96-well head Biomek FX liquid handling robot (Beckman).

The screening experiment previously described was performed in triplicate.

For analysis, per-sample data were scaled to the maximum sum across samples (analogous to normalizing count data to the maximum yield across samples), $\log_2$ transformed and *P*-values are associated with a two-sided *t*-test. Differences were considered significant if the *P*-value remained < 0.05 after Bonferroni correction.

GNB2 knockout

MDA-MB-468 iCas9 cells were transduced with four sgRNAs targeting GNB2 from the pLenti_BSD_sgRNA library, selected by Blasticidin S, and treated with doxycycline as previously described. Cells were then cloned in 96-well plates, and clones were screened for the lack of GNB2 protein by immunofluorescence in black 96-well plates with the same procedure described in the CRISPR Cas9 KO screening and using anti-GNB2 primary antibody (ab81272).

GPCR-centered drug screening

Drug screening was performed in triplicate using three different concentrations (0.1, 1, and 10 μM) for each of the 716 drugs included in the library MedChemExpress (HY-L006). Echo550 acoustic dispenser (Labcyte) within an Access robotic workstation with GX robotic arm was employed to add compounds at the right concentrations to 384-well plates previously seeded with 900 cells/well. After 24-h treatment, cells were fixed, washed, and stained by anti-phospho S6 S240/244 antibody (Cell Signaling Technology Cat#5364) and DAPI as previously described. Images were acquired and quantified as previously described. The fluorescent signal in each well was normalized to DAPI and expressed as *z*-score in each plate.

Reverse-phase protein array

MDA-MB-468 cells were seeded at 350,000 cells/well in six-well plate. After cells were attached, they were treated with vehicle or AZD8186 250 nM for 2 or 28 h. Cell lysates were obtained by the recommended lysis buffer (https://www.mdanderson.org/research/research-resources/core-facilities/functional-proteomics-rppa-core.html), and cell lysates were submitted to MD Anderson Cancer Center RPPA Core Facility. Linear normalized data were analyzed by predicting the mean expression level using a linear model for each time point, with drug status, target and their interaction term as predictors. *P*-values associated with the test for a non-zero coefficient of the interaction term were calculated, and the results were plotted as the mean target-specific drug effect against the *P*-value.

Proliferation assays

Cells were seeded in 96-well plates, and drugs were added on the following day. For 6-day viability assays, drugs were replaced after 3 days of treatment. Cell viability was determined by Cell Titer Blue Viability Assay (Promega).

For long-term assays, cells were seeded into 24-well plates and treated with drugs for 14 days. Drugs were replaced every 3 or 4 days. Cells were fixed and stained with a solution containing 2% ethanol and 0.2% crystal violet. In both assays, starting cell density was optimized to produce an 80–90% confluent monolayer in vehicle-treated cells at the conclusion of the experiment.

The paper explained

Problem
PI3k pathway inhibitors (PI3Kpi) represent a rational choice for the treatment of triple-negative breast cancers (TNBC) that, as a consequence of loss of PTEN tumor suppressor function, show aberrant PI3K pathway activation. Indeed, pre-clinical models of these tumors showed sensitivity to PI3Kpi and especially to inhibition of PI3Kβ. However, clinical efficacy of these drugs has been so far modest, setting the need for more efficient combinatorial approaches.

Results
Through a combination of unbiased screenings and hypothesis-driven approaches, we identified a molecular network that impairs response to PI3Kpi in PTEN-null TNBCs. Both the G protein-coupled receptor PAR1, through engagement of the βγ subunit of G protein, and EGFR were discovered to signal to PI3Kβ in these tumors. The two branches of this pathway can compensate each other and promote the sustained activation of AKT to override PI3Kpi-mediated blockade. Simultaneous inhibition of PI3Kβ and EGFR efficiently blunted the activation of the pathway and produced anti-tumor activity both *in vitro* and *in vivo* in different PTEN-null TNBC models.

Impact
This study unveiled signaling nodes that are fundamental for the survival of PTEN-null TNBCs in the presence of PI3K pathway inhibitors. It also highlighted the combinatorial targeting of PI3Kβ and EGFR as a potential therapeutic strategy to meet the clinical need of treating PTEN-null TNBCs.

Western blot

Protein cell lysates were extracted by boiled Laemmli buffer (2.5% SDS, 125 mM Tris–HCl, PH 6.8), and the lysates were sonicated. The protein concentration of the supernatant was determined by the micro-BCA protein assay (Pierce). Equal amounts of whole cell lysate per lane were boiled in LDS buffer and reducing agent, according to the manufacturer instructions, and separated by electrophoresis in 4–12% gradient NuPAGE Novex Bis-Tris gels (Life Technologies) under reducing conditions, and subsequently transferred to polyvinylidene difluoride membranes (Millipore Immobilon-P). Bound primary antibodies were incubated with horseradish peroxidase-conjugated secondary antibodies and detected using chemiluminescence (Luminata HRP substrate, Millipore). Alternatively, membranes were incubated with secondary conjugates compatible with infrared detection at 700 and 800 nm, and membranes were scanned using the Odyssey Infrared Imaging System (Odyssey, LICOR). Western blot quantification was done using ImageStudioLite software.

Immunoprecipitation

Protein cell lysates were extracted by NP-40 lysis buffer (100 mM TrisCl, pH8.3, 100 mM NaCl, 0.5% Nonidet P-40—Roche) supplemented with tablets of protease and phosphatase inhibitor cocktails (Roche). Cell lysates were cleared by centrifugation at 4°C for

10 min, and the supernatants were collected and quantified by micro-BCA protein assay (Pierce). One milligram of protein lysates was pre-cleared by 50 µl of protein G-Sepharose beads (GE Healthcare 17-0618-01) slurry/sample rotating 30 min at 4°C. Pre-cleared lysates were centrifuged, and the supernatant was incubated rotating overnight with EGFR1 antibody (see compounds and reagents section). The immune-precipitates were then incubated 2 h at 4°C with 50 µl of Agarose-Ig beads, washed five times with washing buffer (50 mM TrisCl, pH8.3, 150 mM NaCl, 0.05% Nonidet P-40 supplemented with protease and phosphatase inhibitor tablets) and re-suspended in LDS buffer and reducing agent. The immune-complexes were the separated by electrophoresis and transferred on polyvinylidene difluoride membranes as previously described and probed with the indicated antibodies.

Quantitative RT–PCR

RNA was isolated (Qiagen), and reverse transcription was conducted (Applied Biosystems) using standard methods. Quantitative real-time PCR was conducted using gene-specific primers (QuantiTect Primer Assays, Qiagen) for EGFR and CSNK2B with Fast SYBR Green Master Mix (Applied Biosystems).

Data availability

Data from shRNA screen are deposited in GEO GSE148785 (https://www.ncbi.nlm.nih.gov/geo/query/acc.cgi?acc=GSE148785).
Source data from the CRISPR-Cas9 KO screen are reported in Table EV3. Data from the GPCR-centered drug screen are reported in Table EV4.

Expanded View for this article is available online.

Acknowledgements
We thank Miriam Molina and David Hancock for helpful discussions and critical reading of the manuscript, Romain Baer for graphical representations of the signaling pathway and the science technology platforms at the Francis Crick Institute including Biological Resources, Advanced Sequencing Facility, Computational Biology, Genomics Equipment Park, Experimental Histopathology and Cell Services. This work was supported by funding to JD from the Francis Crick Institute, which receives its core funding from Cancer Research UK (FC001070), the UK Medical Research Council (FC001070), and the Wellcome Trust (FC001070), from the European Research Council Advanced Grant RASIMMUNE and from a Wellcome Trust Senior Investigator Award 103799/Z/14/Z. DZ was recipient of a post-doctoral fellowship from the Fondazione Umberto Veronesi—Young Investigator Programme 2013.

Author contributions
DZ and JD designed the study, interpreted the results, and wrote the manuscript. DZ and FM performed the biochemical experiments, CM assisted with *in vivo* studies, SH performed bioinformatics analyses, SR assisted with viability experiments, MH provided expertise and carried out screening experiments. All authors contributed to manuscript revision and review.

Conflict of interest
The authors report no conflicts of interest related to this work.

References

Arora P, Cuevas BD, Russo A, Johnson GL, Trejo J (2008) Persistent transactivation of EGFR and ErbB2/HER2 by protease-activated receptor-1 promotes breast carcinoma cell invasion. *Oncogene* 27: 4434 – 4445

Bendell JC, Rodon J, Burris HA, de Jonge M, Verweij J, Birle D, Demanse D, De Buck SS, Ru QC, Peters M *et al* (2012) Phase I, dose-escalation study of BKM120, an oral pan-Class I PI3K inhibitor, in patients with advanced solid tumors. *J Clin Oncol* 30: 282 – 290

Bianchini G, Balko JM, Mayer IA, Sanders ME, Gianni L (2016) Triple-negative breast cancer: challenges and opportunities of a heterogeneous disease. *Nat Rev Clin Oncol* 13: 674 – 690

Bliesath J, Huser N, Omori M, Bunag D, Proffitt C, Streiner N, Ho C, Siddiqui-Jain A, O'Brien SE, Lim JK *et al* (2012) Combined inhibition of EGFR and CK2 augments the attenuation of PI3K-Akt-mTOR signaling and the killing of cancer cells. *Cancer Lett* 322: 113 – 118

Boire A, Covic L, Agarwal A, Jacques S, Sherifi S, Kuliopulos A (2005) PAR1 is a matrix metalloprotease-1 receptor that promotes invasion and tumorigenesis of breast cancer cells. *Cell* 120: 303 – 313

Booden MA, Eckert LB, Der CJ, Trejo J (2004) Persistent signaling by dysregulated thrombin receptor trafficking promotes breast carcinoma cell invasion. *Mol Cell Biol* 24: 1990 – 1999

Cancer Genome Atlas Network (2012) Comprehensive molecular portraits of human breast tumours. *Nature* 490: 61 – 70

Carey LA, Rugo HS, Marcom PK, Mayer EL, Esteva FJ, Ma CX, Liu MC, Storniolo AM, Rimawi MF, Forero-Torres A *et al* (2012) TBCRC 001: randomized phase II study of cetuximab in combination with carboplatin in stage IV triple-negative breast cancer. *J Clin Oncol* 30: 2615 – 2623

Chacon RD, Costanzo MV (2010) Triple-negative breast cancer. *Breast Cancer Res* 12(Suppl 2): S3

Chen ML, Xu PZ, Peng XD, Chen WS, Guzman G, Yang X, Di Cristofano A, Pandolfi PP, Hay N (2006) The deficiency of Akt1 is sufficient to suppress tumor development in Pten+/- mice. *Genes Dev* 20: 1569 – 1574

Ciraolo E, Iezzi M, Marone R, Marengo S, Curcio C, Costa C, Azzolino O, Gonella C, Rubinetto C, Wu H *et al* (2008) Phosphoinositide 3-kinase p110beta activity: key role in metabolism and mammary gland cancer but not development. *Sci Signal* 1: ra3

Darmoul D, Gratio V, Devaud H, Peiretti F, Laburthe M (2004) Activation of proteinase-activated receptor 1 promotes human colon cancer cell proliferation through epidermal growth factor receptor transactivation. *Mol Cancer Res* 2: 514 – 522

Delaloge S, DeForceville L (2017) Targeting PI3K/AKT pathway in triple-negative breast cancer. *Lancet Oncol* 18: 1293 – 1294

Di Maira G, Salvi M, Arrigoni G, Marin O, Sarno S, Brustolon F, Pinna LA, Ruzzene M (2005) Protein kinase CK2 phosphorylates and upregulates Akt/PKB. *Cell Death Differ* 12: 668 – 677

Dickler MN, Rugo HS, Eberle CA, Brogi E, Caravelli JF, Panageas KS, Boyd J, Yeh B, Lake DE, Dang CT *et al* (2008) A phase II trial of erlotinib in combination with bevacizumab in patients with metastatic breast cancer. *Clin Cancer Res* 14: 7878 – 7883

Even-Ram S, Uziely B, Cohen P, Grisaru-Granovsky S, Maoz M, Ginzburg Y, Reich R, Vlodavsky I, Bar-Shavit R (1998) Thrombin receptor overexpression in malignant and physiological invasion processes. *Nat Med* 4: 909 – 914

Filardo EJ, Quinn JA, Bland KI, Frackelton AR Jr (2000) Estrogen-induced activation of Erk-1 and Erk-2 requires the G protein-coupled receptor homolog, GPR30, and occurs via trans-activation of the epidermal growth factor receptor through release of HB-EGF. *Mol Endocrinol* 14: 1649 – 1660

Furman RR, Sharman JP, Coutre SE, Cheson BD, Pagel JM, Hillmen P, Barrientos JC, Zelenetz AD, Kipps TJ, Flinn I *et al* (2014) Idelalisib and rituximab in relapsed chronic lymphocytic leukemia. *N Engl J Med* 370: 997 – 1007

Gopal AK, Kahl BS, de Vos S, Wagner-Johnston ND, Schuster SJ, Jurczak WJ, Flinn IW, Flowers CR, Martin P, Viardot A *et al* (2014) PI3Kdelta inhibition by idelalisib in patients with relapsed indolent lymphoma. *N Engl J Med* 370: 1008 – 1018

Gumuskaya B, Alper M, Hucumenoglu S, Altundag K, Uner A, Guler G (2010) EGFR expression and gene copy number in triple-negative breast carcinoma. *Cancer Genet Cytogenet* 203: 222 – 229

Haddadi N, Lin Y, Travis G, Simpson AM, Nassif NT, McGowan EM (2018) PTEN/PTENP1: 'Regulating the regulator of RTK-dependent PI3K/Akt signalling', new targets for cancer therapy. *Mol Cancer* 17: 37

Hancox U, Cosulich S, Hanson L, Trigwell C, Lenaghan C, Ellston R, Dry H, Crafter C, Barlaam B, Fitzek M *et al* (2015) Inhibition of PI3Kbeta signaling with AZD8186 inhibits growth of PTEN-deficient breast and prostate tumors alone and in combination with docetaxel. *Mol Cancer Ther* 14: 48 – 58

Hauser AS, Attwood MM, Rask-Andersen M, Schioth HB, Gloriam DE (2017) Trends in GPCR drug discovery: new agents, targets and indications. *Nat Rev Drug Discov* 16: 829 – 842

Hopkins BD, Pauli C, Du X, Wang DG, Li X, Wu D, Amadiume SC, Goncalves MD, Hodakoski C, Lundquist MR *et al* (2018) Suppression of insulin feedback enhances the efficacy of PI3K inhibitors. *Nature* 560: 499 – 503

Janku F, Yap TA, Meric-Bernstam F (2018) Targeting the PI3K pathway in cancer: are we making headway? *Nat Rev Clin Oncol* 15: 273 – 291

Jia S, Liu Z, Zhang S, Liu P, Zhang L, Lee SH, Zhang J, Signoretti S, Loda M, Roberts TM *et al* (2008) Essential roles of PI(3)K-p110beta in cell growth, metabolism and tumorigenesis. *Nature* 454: 776 – 779

Juric D, Janku F, Rodon J, Burris HA, Mayer IA, Schuler M, Seggewiss-Bernhardt R, Gil-Martin M, Middleton MR, Baselga J *et al* (2018a) Alpelisib plus fulvestrant in PIK3CA-Altered and PIK3CA-wild-type estrogen receptor-positive advanced breast cancer: a phase 1b clinical trial. *JAMA* Oncol: e184475

Juric D, Rodon J, Tabernero J, Janku F, Burris HA, Schellens JHM, Middleton MR, Berlin J, Schuler M, Gil-Martin M *et al* (2018b) Phosphatidylinositol 3-kinase alpha-selective inhibition with alpelisib (BYL719) in PIK3CA-altered solid tumors: results from the first-in-human study. *J Clin Oncol* 36: 1291 – 1299

Kalathur M, Toso A, Chen J, Revandkar A, Danzer-Baltzer C, Guccini I, Alajati A, Sarti M, Pinton S, Brambilla L *et al* (2015) A chemogenomic screening identifies CK2 as a target for pro-senescence therapy in PTEN-deficient tumours. *Nat Commun* 6: 7227

Kanda Y, Mizuno K, Kuroki Y, Watanabe Y (2001) Thrombin-induced p38 mitogen-activated protein kinase activation is mediated by epidermal growth factor receptor transactivation pathway. *Br J Pharmacol* 132: 1657 – 1664

Kim SB, Dent R, Im SA, Espie M, Blau S, Tan AR, Isakoff SJ, Oliveira M, Saura C, Wongchenko MJ *et al* (2017) Ipatasertib plus paclitaxel versus placebo plus paclitaxel as first-line therapy for metastatic triple-negative breast cancer (LOTUS): a multicentre, randomised, double-blind, placebo-controlled, phase 2 trial. *Lancet Oncol* 18: 1360 – 1372

Konieczkowski DJ, Johannessen CM, Garraway LA (2018) A convergence-based framework for cancer drug resistance. *Cancer Cell* 33: 801 – 815

Kurosu H, Maehama T, Okada T, Yamamoto T, Hoshino S, Fukui Y, Ui M, Hazeki O, Katada T (1997) Heterodimeric phosphoinositide 3-kinase consisting of p85 and p110beta is synergistically activated by the betagamma subunits of G proteins and phosphotyrosyl peptide. *J Biol Chem* 272: 24252 – 24256

Li H, Durbin R (2009) Fast and accurate short read alignment with Burrows-Wheeler transform. *Bioinformatics* 25: 1754 – 1760

Liedtke C, Mazouni C, Hess KR, Andre F, Tordai A, Mejia JA, Symmans WF, Gonzalez-Angulo AM, Hennessy B, Green M *et al* (2008) Response to neoadjuvant therapy and long-term survival in patients with triple-negative breast cancer. *J Clin Oncol* 26: 1275 – 1281

Lillian S, De Bono J, Higano C, Shapiro G, Brugger W, Mitchell P, Colebrook S, Klinowska T, Barry S, Dean EJ *et al* (2016) AZD8186 study 1: phase I study to assess the safety, tolerability, pharmacokinetics (PK), pharmacodynamics (PD) and preliminary anti-tumour activity of AZD8186 in patients with advanced castration-resistant prostate cancer (CRPC), squamous non-small cell lung cancer, triple negative breast cancer and with PTEN-deficient/mutated or PIK3CB mutated/amplified malignancies, as monotherapy and in combination with vistusertib (AZD2014) or abiraterone acetate. *Eur J Cancer* 69: S19

Liu JC, Voisin V, Wang S, Wang DY, Jones RA, Datti A, Uehling D, Al-awar R, Egan SE, Bader GD *et al* (2014) Combined deletion of Pten and p53 in mammary epithelium accelerates triple-negative breast cancer with dependency on eEF2K. *EMBO Mol Med* 6: 1542 – 1560

Maehama T, Dixon JE (1998) The tumor suppressor, PTEN/MMAC1, dephosphorylates the lipid second messenger, phosphatidylinositol 3,4,5-trisphosphate. *J Biol Chem* 273: 13375 – 13378

Martin V, Botta F, Zanellato E, Molinari F, Crippa S, Mazzucchelli L, Frattini M (2012) Molecular characterization of EGFR and EGFR-downstream pathways in triple negative breast carcinomas with basal like features. *Histol Histopathol* 27: 785 – 792

Martin M, Chan A, Dirix L, O'Shaughnessy J, Hegg R, Manikhas A, Shtivelband M, Krivorotko P, Batista Lopez N, Campone M *et al* (2017) A randomized adaptive phase II/III study of buparlisib, a pan-class I PI3K inhibitor, combined with paclitaxel for the treatment of HER2- advanced breast cancer (BELLE-4). *Ann Oncol* 28: 313 – 320

von Minckwitz G, Jonat W, Fasching P, du Bois A, Kleeberg U, Luck HJ, Kettner E, Hilfrich J, Eiermann W, Torode J *et al* (2005) A multicentre phase II study on gefitinib in taxane- and anthracycline-pretreated metastatic breast cancer. *Breast Cancer Res Treat* 89: 165 – 172

Murga C, Fukuhara S, Gutkind JS (2000) A novel role for phosphatidylinositol 3-kinase beta in signaling from G protein-coupled receptors to Akt. *J Biol Chem* 275: 12069 – 12073

Nakai K, Hung MC, Yamaguchi H (2016) A perspective on anti-EGFR therapies targeting triple-negative breast cancer. *Am J Cancer Res* 6: 1609 – 1623

Park HS, Jang MH, Kim EJ, Kim HJ, Lee HJ, Kim YJ, Kim JH, Kang E, Kim SW, Kim IA *et al* (2014) High EGFR gene copy number predicts poor outcome in triple-negative breast cancer. *Mod Pathol* 27: 1212 – 1222

Reis-Filho JS, Pinheiro C, Lambros MB, Milanezi F, Carvalho S, Savage K, Simpson PT, Jones C, Swift S, Mackay A *et al* (2006) EGFR amplification and lack of activating mutations in metaplastic breast carcinomas. *J Pathol* 209: 445 – 453

Reis-Filho JS, Tutt AN (2008) Triple negative tumours: a critical review. *Histopathology* 52: 108 – 118

Sabri A, Short J, Guo J, Steinberg SF (2002) Protease-activated receptor-1-mediated DNA synthesis in cardiac fibroblast is via epidermal growth factor receptor transactivation: distinct PAR-1 signaling pathways in cardiac fibroblasts and cardiomyocytes. *Circ Res* 91: 532 – 539

Sangai T, Akcakanat A, Chen H, Tarco E, Wu Y, Do KA, Miller TW, Arteaga CL, Mills GB, Gonzalez-Angulo AM *et al* (2012) Biomarkers of response to Akt inhibitor MK-2206 in breast cancer. *Clin Cancer Res* 18: 5816 – 5828

Schmit F, Utermark T, Zhang S, Wang Q, Von T, Roberts TM, Zhao JJ (2014) PI3K isoform dependence of PTEN-deficient tumors can be altered by the genetic context. *Proc Natl Acad Sci USA* 111: 6395 – 6400

Schwartz S, Wongvipat J, Trigwell CB, Hancox U, Carver BS, Rodrik-Outmezguine V, Will M, Yellen P, de Stanchina E, Baselga J *et al* (2015) Feedback suppression of PI3Kalpha signaling in PTEN-mutated tumors is relieved by selective inhibition of PI3Kbeta. *Cancer Cell* 27: 109 – 122

Shao MM, Zhang F, Meng G, Wang XX, Xu H, Yu XW, Chen LY, Tse GM (2011) Epidermal growth factor receptor gene amplification and protein over-expression in basal-like carcinoma of the breast. *Histopathology* 59: 264 – 273

She QB, Gruvberger-Saal SK, Maurer M, Chen Y, Jumppanen M, Su T, Dendy M, Lau YK, Memeo L, Horlings HM *et al* (2016) Integrated molecular pathway analysis informs a synergistic combination therapy targeting PTEN/PI3K and EGFR pathways for basal-like breast cancer. *BMC Cancer* 16: 587

Stambolic V, Suzuki A, de la Pompa JL, Brothers GM, Mirtsos C, Sasaki T, Ruland J, Penninger JM, Siderovski DP, Mak TW (1998) Negative regulation of PKB/Akt-dependent cell survival by the tumor suppressor PTEN. *Cell* 95: 29 – 39

Stemke-Hale K, Gonzalez-Angulo AM, Lluch A, Neve RM, Kuo WL, Davies M, Carey M, Hu Z, Guan Y, Sahin A *et al* (2008) An integrative genomic and proteomic analysis of PIK3CA, PTEN, and AKT mutations in breast cancer. *Cancer Res* 68: 6084 – 6091

Thorpe LM, Yuzugullu H, Zhao JJ (2015) PI3K in cancer: divergent roles of isoforms, modes of activation and therapeutic targeting. *Nat Rev Cancer* 15: 7 – 24

Vasudevan KM, Barbie DA, Davies MA, Rabinovsky R, McNear CJ, Kim JJ, Hennessy BT, Tseng H, Pochanard P, Kim SY *et al* (2009) AKT-independent signaling downstream of oncogenic PIK3CA mutations in human cancer. *Cancer Cell* 16: 21 – 32

Wagner KU, Wall RJ, St-Onge L, Gruss P, Wynshaw-Boris A, Garrett L, Li M, Furth PA, Hennighausen L (1997) Cre-mediated gene deletion in the mammary gland. *Nucleic Acids Res* 25: 4323 – 4330

Wang T, Birsoy K, Hughes NW, Krupczak KM, Post Y, Wei JJ, Lander ES, Sabatini DM (2015) Identification and characterization of essential genes in the human genome. *Science* 350: 1096 – 1101

Wee S, Wiederschain D, Maira SM, Loo A, Miller C, deBeaumont R, Stegmeier F, Yao YM, Lengauer C (2008) PTEN-deficient cancers depend on PIK3CB. *Proc Natl Acad Sci USA* 105: 13057 – 13062

Yardley DA, Ward PJ, Daniel BR, Eakle JF, Lamar RE, Lane CM, Hainsworth JD (2016) Panitumumab, gemcitabine, and carboplatin as treatment for women with metastatic triple-negative breast cancer: a sarah cannon research institute phase II trial. *Clin Breast Cancer* 16: 349 – 355.

Zhou Y, Zhu S, Cai C, Yuan P, Li C, Huang Y, Wei W (2014) High-throughput screening of a CRISPR/Cas9 library for functional genomics in human cells. *Nature* 509: 487 – 491

Analysis of cancer spheroids through high-throughput screening assays

Introduction

Cancer cells grown as spheroids resemble human tumors more closely than cells grown in monolayers, with respect to morphology, structural complexity, phenotype, and sensitivity to chemotherapeutics. Being more physiologically relevant model systems, they can be more predictive of drug profiling and cytotoxicity. So, early screens of drugs have become more dependent on 3D cell culture. In recent years, tumor-derived spheroids have been utilized to optimize cancer therapeutics for ovarian and hepatocellular carcinoma [**1**,**2**,**3**]. However, there are some challenges to using spheroids for drug screening: primarily, the number of spheroids per well, and the shape and size of spheroids, need to be uniform in order to reduce variability between replicates. To address this challenge, we compiled tips and tricks on how to generate uniform and reproducible cancer spheroids for high-throughput screening (HTS) assays in an application note titled "**Generation of cancer spheroids—tips and tricks**". Additionally, we have outlined a workflow for robust 3D cancer spheroid generation in Figure 1.

Graphical workflow of 3D cancer spheroid generation

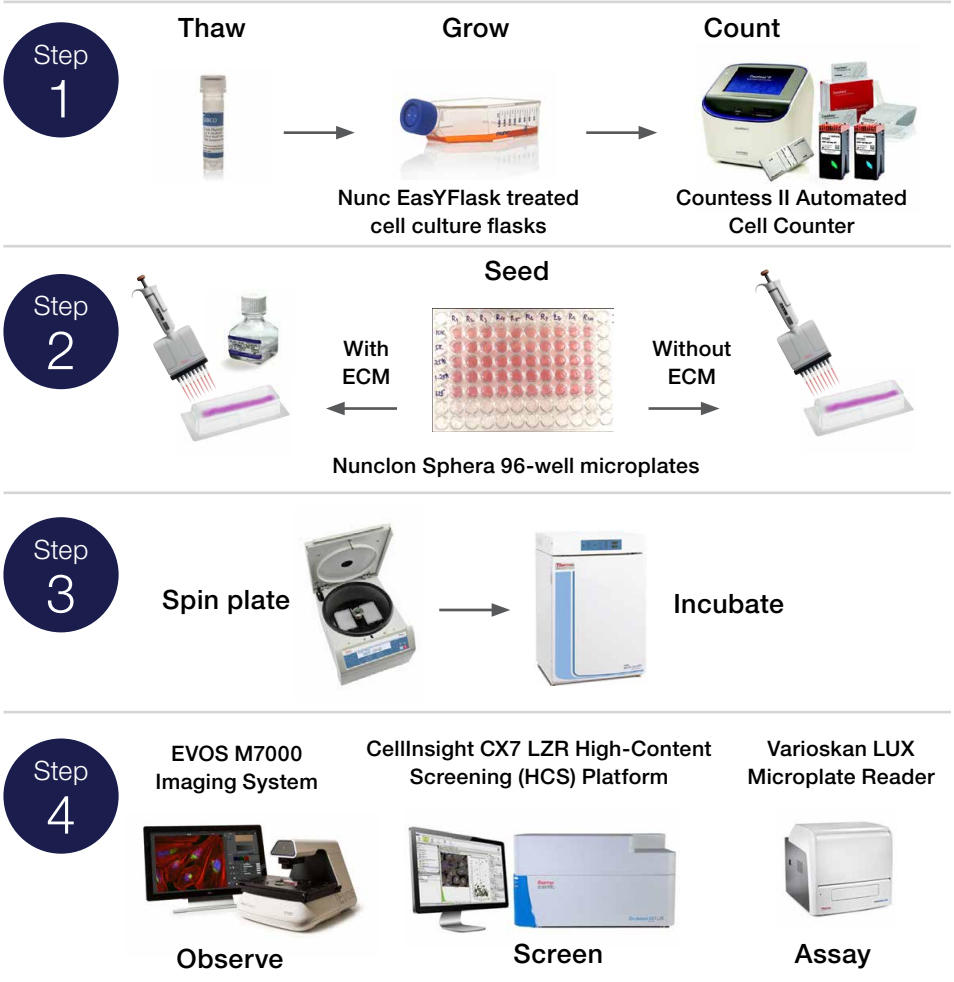

Figure 1. Schematic representation of the process of spheroid generation on Thermo Scientific™ Nunclon™ Sphera™ plates.

Another challenge in working with spheroids is determining penetration of drugs to optimize treatment times. Moreover, the use of spheroids can complicate experimental design and interpretation, but this can be overcome by using the right kinds of reagents, equipment, and protocols. Here we outline different kinds of HTS assays that can be performed on cancer spheroids to assess drug response. We also provide some useful guidelines for handling spheroids and acquiring data to get the most meaningful results. All spheroids were generated on Nunclon Sphera plates using the appropriate Gibco™ cell culture medium.

Assays with plate reader–based readouts

Cell viability and cytotoxicity assays using Invitrogen™ PrestoBlue™ HS Cell Viability Reagent

This straightforward assay utilizes resazurin as a cell health monitor. Upon entering healthy cells, resazurin is reduced in the mitochondria to resorufin, resulting in fluorescence (Ex/Em 560/590 nm). Using this assay, we compared the response of cells in 2D and 3D cultures to doxorubicin, a chemotherapeutic agent. Two different types of cancer cells (HepG2 and PANC-1) were considered. Spheroids and monolayers were treated with doxorubicin either 4 (HepG2) or 7 days (PANC-1) after plating and allowed to incubate for 72 hours. PrestoBlue HS reagent was then added 1:10 (v/v) to the spent medium, and spheroids were incubated at 37°C for 6 hours.

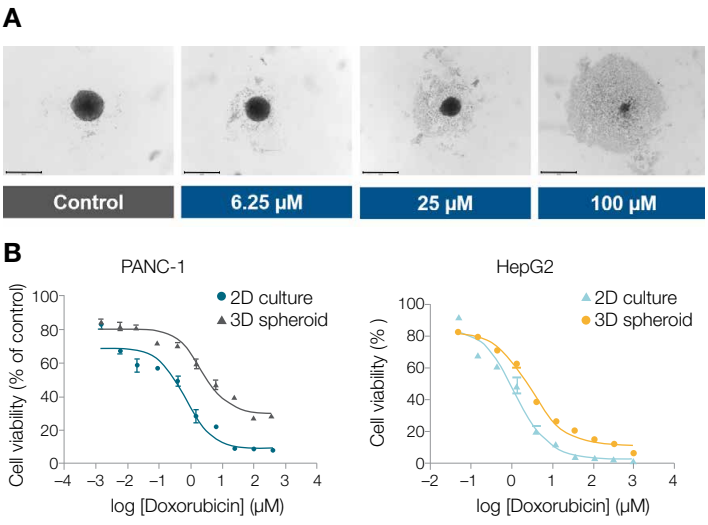

Figure 2. Morphology and effectiveness of doxorubicin treatment on spheroids in 2D and 3D cultures. (A) Morphology of control and doxorubicin-treated PANC-1 spheroids 72 hours posttreatment. Images were captured using the **Thermo Scientific™ EVOS™ M7000 Imaging System** under a 4x objective. Scale bar: 650 µm. **(B)** Dose response curves for doxorubicin-treated PANC-1 (left) and HepG2 (right) spheroids in 2D and 3D cultures.

Following this, high-throughput readouts were obtained using the Thermo Scientific™ Varioskan™ LUX Multimode Microplate Reader. We recommend taking a top read for homogeneity between experimental repeats. Nonlinear regression analysis was performed for variable slope of log (inhibitor) vs. response to calculate the IC_{50} using GraphPad Prism 5.01. As seen with PANC-1 (Figure 2A), doxorubicin treatment caused disintegration of spheroids with increasing dose, indicating cytotoxicity. For both cell lines, the IC_{50} of doxorubicin for 3D culture was at least twice that for the 2D culture (Figure 2B), suggesting increased sensitivity of 2D cultures towards the drug.

Analyzing PSA levels using the Invitrogen™ PSA (Total)/KLK3 Human ELISA Kit

Prostate-specific antigen (PSA) in serum is a known biomarker for prostate cancer diagnosis. The PSA (Total)/KLK3 Human ELISA Kit has been successfully used to detect PSA in cell culture supernatant from 2D culture [**4**]. Using the manufacturer's instructions, we compared PSA secretion in 2D and 3D cell cultures. We chose the LNCaP cell line that expresses the *KLK3* gene (which in turn encodes PSA) endogenously. Medium from PC-3 cells, which do not produce PSA endogenously, was used as a negative control. LNCaP monolayers and spheroids were treated with 2 nM dihydrotestosterone (DHT, which enhances PSA expression) or 80 µM cisplatin (represses PSA expression) 4 days after plating, and incubated for 48 hours. Culture supernatant was collected, diluted 1:20 in diluent buffer, and assayed for secreted PSA using the PSA (Total)/KLK3 Human ELISA Kit and the Varioskan LUX Multimode Plate Reader for colorimetric reading. The colorimetric readings were used to calculate relative PSA levels according to the kit instructions.

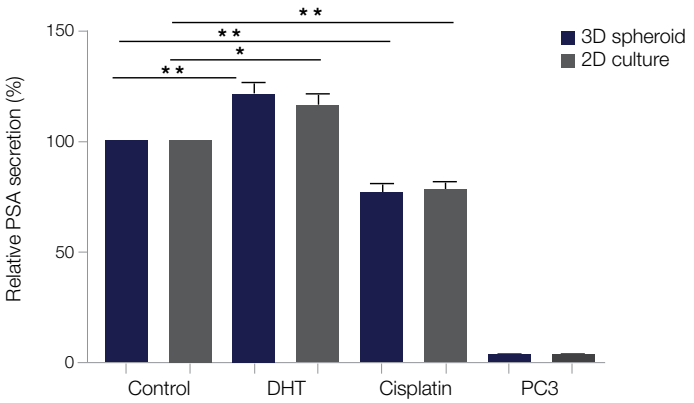

Figure 3. Quantification by ELISA of secretion of PSA following treatment with DHT and cisplatin. Error bars denote standard error of the mean. N = 2. *$P < 0.01$ and **$P < 0.001$ for difference from untreated control by one-way analysis of variance (ANOVA).

DHT treatment resulted in 17% and 21% increases in PSA secretion in 2D and 3D culture, respectively, while treatment with cisplatin reduced endogenous PSA secretion by 22–23% (Figure 3). However, 3D culture did not show any major difference in resting or induced PSA levels from 2D culture. This exemplifies how conditioned medium from spheroids can be used for high-throughput non–cell-based assays. In fact, using appropriate readouts, multiplexing of assays can also be performed.

Assays with image-based readouts

Cell viability/cytotoxicity assay using Invitrogen™ LIVE/DEAD™ kit

The LIVE/DEAD kit is a two-color assay that measures cell viability based on plasma membrane integrity and esterase activity. It discriminates live cells from dead cells by staining live cells with Invitrogen™ calcein AM, which is converted to green-fluorescent calcein by intracellular esterase activity, and dead cells with red-fluorescent ethidium homodimer 1 (EthD-1), indicating loss of plasma membrane integrity. After 1 day in culture, SKOV-3 spheroids were treated with various concentrations of the chemotherapeutic drug paclitaxel for 72 hours, followed by incubation with 1 µM each of calcein AM and EthD-1 at 37°C for 3 hours. Following this, spheroids were washed by exchanging half of the medium with 1X PBS, then imaged. We found that exchanging the medium gently from the sides of the wells works better than centrifuging the plates and helps the spheroids stay at the center of the wells, thus aiding in image acquisition (Figure 4A). Spheroids were autofocused using the DAPI channel (they were incubated with **Invitrogen™ NucBlue™ Live ReadyProbes™ Reagent** along with calcein AM and EthD-1 staining), and the centered, maximum-intensity image projection was used to capture the z-stacks. Images were captured using the **Thermo Scientific™ CellInsight™ CX7 High-Content Screening Platform** and analyzed using the cell viability tool on Thermo Scientific™ HCS Studio Cell Analysis Software 4.0. Calcein fluorescence values in the treated samples were normalized to those of the control samples to calculate percentage of viable cells. Values were plotted against paclitaxel concentration using GraphPad Prism software. Increasing paclitaxel concentration led to concomitant reduction in cell viability (Figure 4B).

Apoptosis assay using Invitrogen™ CellEvent™ Caspase-3/7 Green Detection Reagent

The reagent is a four–amino acid peptide (DEVD) conjugated to a nucleic acid–binding dye. The dye is nonfluorescent unless DEVD is cleaved by active caspase-3/7. Following DEVD cleavage, the dye is able to bind to DNA and give a fluorescence signal, providing a means to detect cells undergoing caspase-3/7–dependent apoptosis. MDA-MB-231 spheroids were formed using collagen I as previously **described**, and on day 4 treated with various concentrations of the caspase-dependent, apoptosis-inducing drug etoposide for 72 hours. Spheroids were then incubated with 2 µM of the CellEvent Caspase-3/7 Green Detection Reagent and 1 drop of Invitrogen™ NucBlue™ reagent per milliliter of PBS at 37°C for 2 hours. If PBS is used at this stage, spheroids do not require additional washing. Images were captured on the CellInsight CX7 High-Content Screening Platform under a 4x objective in confocal mode and analyzed using the spot measurement tool of HCS Studio software 4.1.

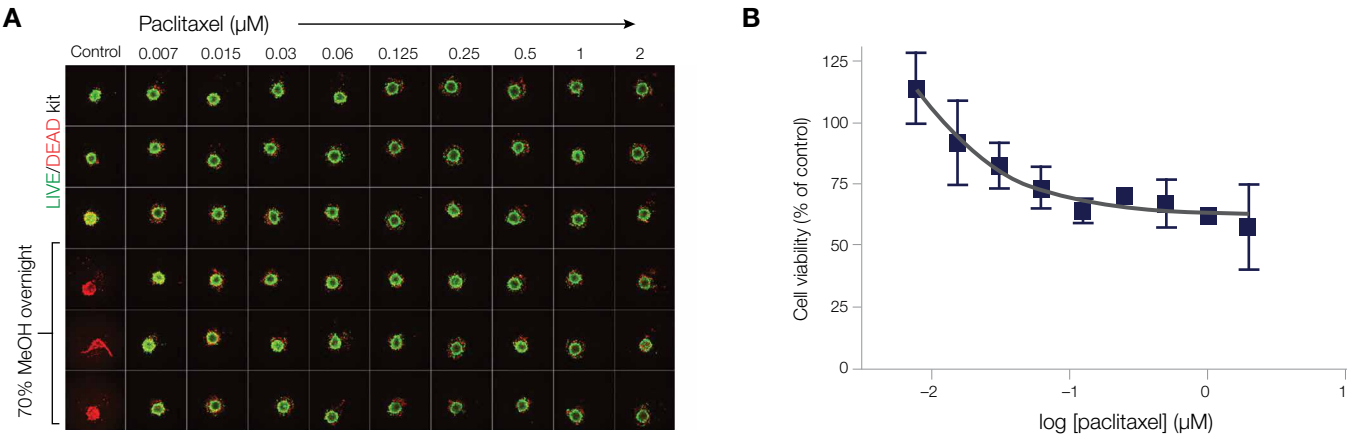

Figure 4. Cell viability assay analysis. (A) Image montage showing LIVE/DEAD staining of SKOV-3 spheroids following treatment with paclitaxel. Images were acquired using the CellInsight CX7 HCS Platform under a 4x objective and in confocal mode. Cells treated with 70% methanol (to kill the cells) in the specified wells served as a negative control for the assay. **(B)** Plot of percent viability of cells with increasing paclitaxel concentrations. The values obtained using HCS Studio software were plotted in GraphPad Prism software and were fit to scale using nonlinear regression. N = 2.

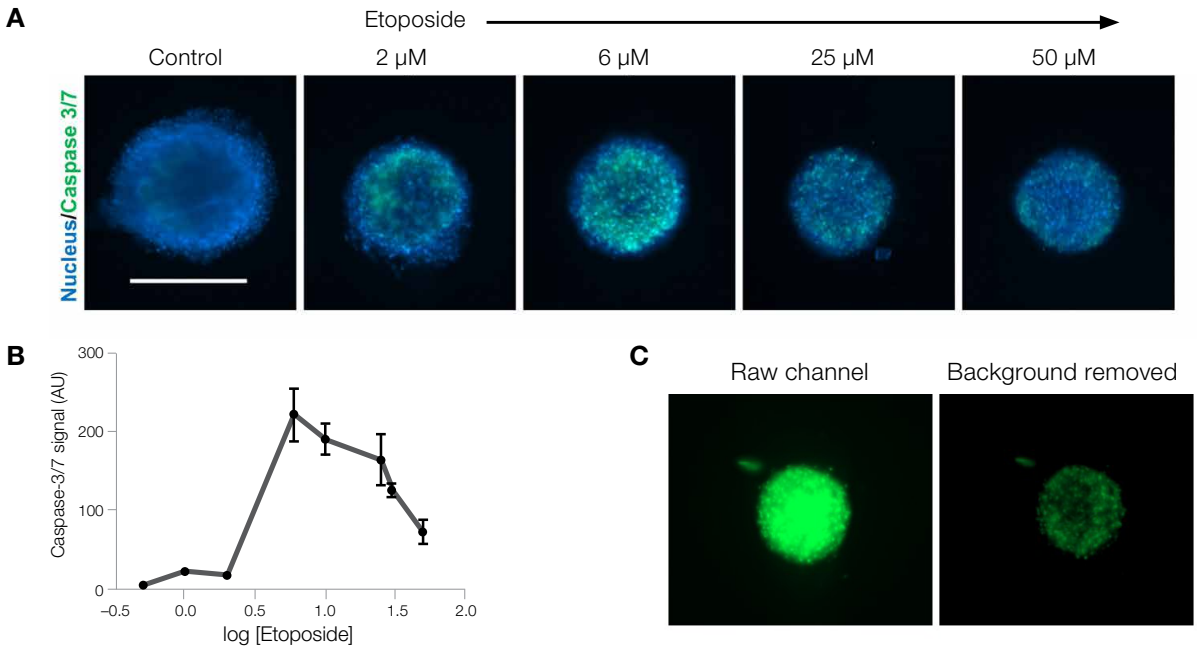

Figure 5. Apoptosis assay analysis. (A) Representative images of control and etoposide-treated MDA-MB-231 spheroids. Scale bar: 500 µm. **(B)** Plot of caspase-3/7 signal intensity against increasing concentrations of etoposide. Six spheroids were considered for every treatment concentration. The plot was generated using GraphPad Prism software from the data obtained from HCS Studio software. Error bars represent standard deviation; N = 2. **(C)** Representation of raw channel (left) and background-corrected channel image (right) for MDA-MB-231 spheroids.

Compared to the control, there was an increase in caspase-3/7 signal with increasing etoposide concentration. However, beyond 6 µM etoposide, the caspase-3/7 signal decreased gradually, possibly owing to an increase in cell death (Figure 5A, B). Another point to note is that the extracellular matrix created background in staining, but using the background removal function for the green channel in HCS Studio software removed it (Figure 5C).

Cell proliferation assay using the Invitrogen™ ClickiT™ EdU Cell Proliferation Kit

This kit uses "click" chemistry to detect cells undergoing new DNA synthesis. T-47D cells were allowed to form spheroids for 24 hours, after which they were treated with 100 nM colchicine, an inhibitor of the mitotic phase of the cell cycle. After approximately 30 hours of treatment, 50% of the spent medium was exchanged with fresh medium containing 20 µM EdU and incubated overnight at 37^{0}C. Proliferating cells that had incorporated EdU were detected using the Click-iT EdU Cell Proliferation Kit with slight changes in the manufacturer's protocol. Briefly, cells were fixed in 3.7% Thermo Scientific™ Pierce™ Formaldehyde for 30 minutes and permeabilized with 0.25% Thermo Scientific™ Triton™ X-100 detergent for 1 hour, followed by incubation with Click-iT EdU dye detection cocktail overnight (as opposed to 30 minutes at room temperature as stated in the kit instructions).

Due to multiple washes involved in the protocol, it is possible that spheroids get dislodged from the center of the well. As a result, they don't always fall completely in the path of light. This gives erroneous readings and variability between replicates. Thus, visualizing the spheroids followed by analysis gives more meaningful data. An example is shown in Figure 6A. Here, both spheroids have been dislodged from the center of the well, but the spheroid in the right panel (shown with arrow) is only partially captured in the field of view. Hence it was excluded from the analysis. Also, small spheroids (200–400 µm) had to be used in the assay to capture most of the spheroids on the Thermo Scientific™ CellInsight CX7 and CX7 LZR HCS Platforms. However, this challenge has been resolved with a new software technology, Thermo Scientific™ EurekaScan™ Finder. EurekaScan Finder has a "seek and find" feature for the CellInsight CX7 LED and LZR HCS Platforms aimed at accelerating discovery by automating the identification and capture of irregularly seeded biological samples, including spheroids, at progressively higher magnifications. With the EurekaScan Finder feature applied, specimens are identified during low-magnification "seek" operations and, once "found", efficiently scanned at higher magnifications for optimal resolution. EurekaScan Finder allows scientists to first identify samples using low magnification across large surface areas, capture them at intermediate magnification, then evaluate them for rare events or improved resolution at higher magnifications.

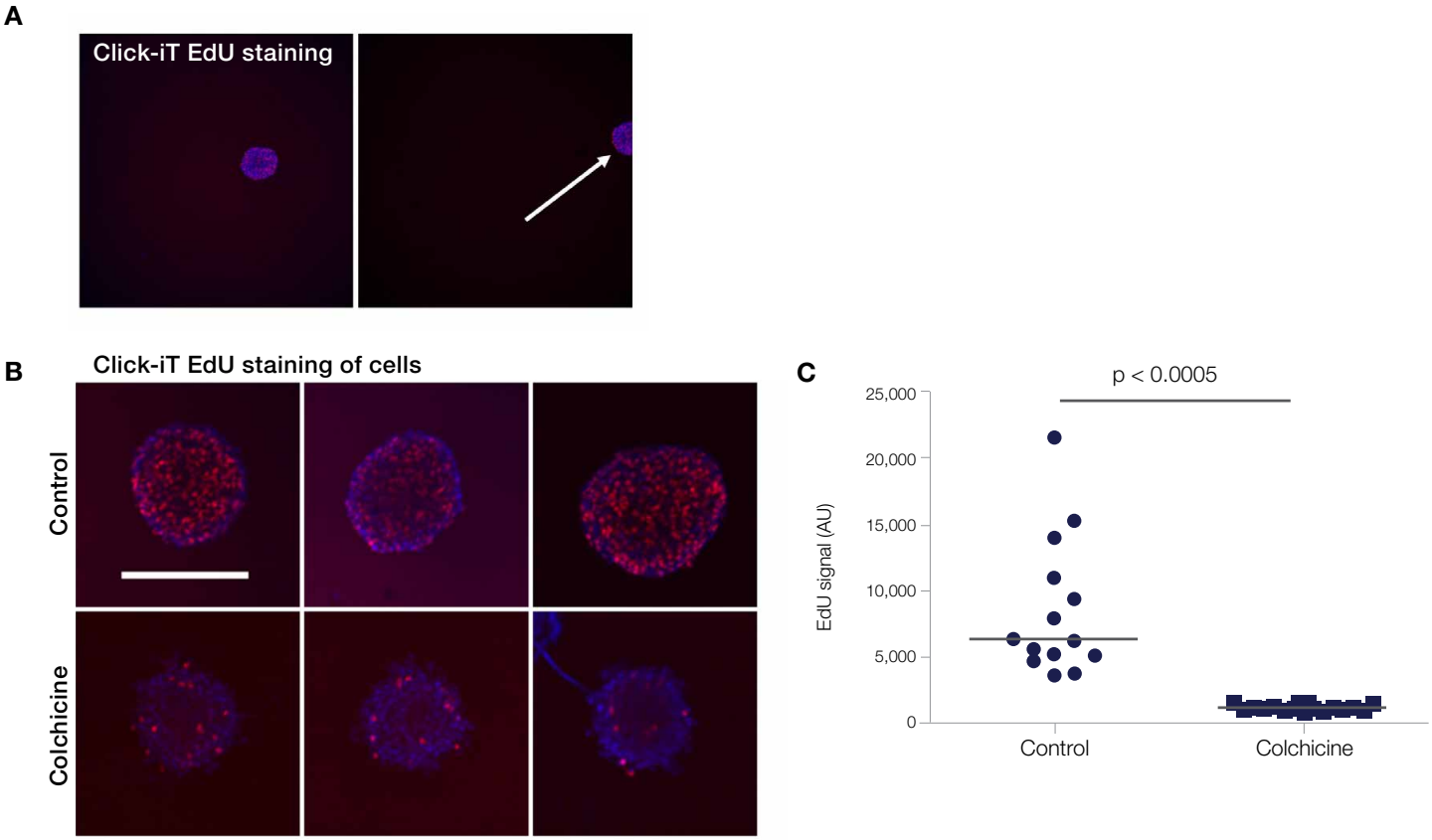

Figure 6. Cell proliferation assay analysis. (A) Field view of a fully captured (left) and a partially captured (right) spheroid as the latter got dislodged during washing. **(B)** Representative images showing Click-iT EdU staining (red) in T-47D spheroids without and with colchicine treatment. Images were acquired using the CellInsight CX7 HCS Platform under a 4x objective and in confocal mode. Scale bar: 200 µm. **(C)** Dot plot analysis of cellular proliferation in T-47D spheroids without and with colchicine treatment. The general intensity measurement tool in HCS Studio software 4.0 was used to analyze the Click-iT EdU signal (y-axis); N = 2. *P* < 0.0005 for difference from control by unpaired *t*-test.

Nevertheless, buffer exchanges should be performed carefully, as scratches in the wells give background signal during imaging, leading to noise in analysis.

For cell proliferation analysis, the spheroid was masked to negate background signal intensity. As depicted qualitatively in Figure 6B and quantitatively in 6C, colchicine treatment led to a significant reduction in proliferating cells in spheroids, indicated by reduced EdU signals.

Conclusion

Though spheroids can be more complicated to analyze than cells cultured under standard 2D conditions, we have shown that a wide variety of cell-based as well as culture supernatant–based assays can be optimized to test drug responses in cancer cells grown in 3D. For the majority of cases, increasing the incubation time of drugs as well as detection reagents for 3D cultures helps reagents better penetrate the spheroids and results in more meaningful data. We recommend keeping washes to a minimum and instead using media exchanges. Based on our observations, centrifuging spheroid-containing plates multiple times does not help to settle spheroids at the bottom, especially if the spheroids are fixed. So, exchanging buffer carefully and gently along the sides of wells is recommended. For comparative studies where analysis can be done on the medium rather than the cells, e.g., PrestoBlue HS reagent or ELISA, a microplate-based readout is the preferred method. However, when the readout is cell based and involves multiple buffer exchange steps, such as the CellEvent Caspase-3/7 Green Detection Reagent for apoptosis studies or Click-iT EdU detection kit for cell proliferation studies, an image-based readout will yield more reliable and reproducible information about the cellular effect of drugs.

Ordering information

Product	Cat. No.
Plastics	
Nunclon Sphera 96-well plates	174925
Nunclon 96-well optical-bottom plates	164588
Matrix Reagent Reservoirs	8094
Media, serum, and antibiotics	
DMEM (PANC-1, MDA-MB-231)	31966021
MEM (HepG2)	11095080
RPMI (LNCaP, T47D)	72400047
McCoy's 5A (SKOV-3)	16600082
Fetal Bovine Serum (FBS)	10270106
Penicillin-Streptomycin	15140122
Reagents and kits	
Phosphate-Buffered Saline (PBS)	10010031
PrestoBlue HS Cell Viability Reagent	P50201
LIVE/DEAD Viability/Cytotoxicity Kit	L3224
NucBlue Live ReadyProbes Reagent	R37605
PSA (Total)/KLK3 Human ELISA Kit	EHKLK3T
CellEvent Caspase-3/7 Green Detection Reagent	C10423
Click-iT Plus EdU Cell Proliferation Kit	C10639
Instruments	
CellInsight CX7 LZR High-Content Screening (HCS) Platform	A46120
Varioskan LUX Multimode Microplate Reader	N16045
EVOS M7000 Imaging System	AMF7000
Pipettes	
Finnpipette F1 Multichannel Pipettes	4661020N, 4661030N

Find out more at **thermofisher.com/sphera**

ThermoFisher SCIENTIFIC